THESIS

SCATTER LOSS AND SURFACE ROUGHNESS OF HAFNIUM OXIDE THIN FILMS

Submitted by

Jonathan Tollerud

Department of Electrical and Computer Engineering

In partial fulfillment of the requirements

For the Degree of Master of Science

Colorado State University

Fort Collins, Colorado

Fall 2011

Master's Committee:

Advisor: Carmen Menoni

Azer Yalin
Mario Marconi

ABSTRACT

SCATTER LOSS AND SURFACE ROUGHNESS OF HAFNIUM OXIDE THIN FILMS

The work presented in the thesis aims to characterize and improve the surface quality and scatter loss of HfO_2 single layer thin films. Dual ion beam sputtered coatings of HfO_2 produced at CSU have been shown to have a high damage threshold and low absorption. They have not been optimized for reduced surface roughness. Both surface quality and scattering of dual ion beam sputtered thin films depend on the growth conditions and substrate quality, so a study of growth parameters and substrate choice is conducted. The growth parameters selected in this work are beam voltage of the main ion source and sample thickness. Samples grown on standard optically polished substrates are compared to samples grown on two types of super-polished substrates. A multilayer coating is also examined to characterize how scatter loss scales with the number of layers.

A device is built to measure scatter loss at 1064nm, 633nm and 405nm and an in depth analysis is conducted of the surfaces using atomic force microscopy and white light interferometry. The films scatter loss at 1064nm are shown to be sensitive to substrate choice, film thickness and main beam voltage. Scatter loss at 1064nm generally decreases when beam voltage is reduced. Scatter loss at lower wavelengths decreases much more significantly. Smoother substrates show improved scatter performance, but it is again much more noticeable at lower wavelengths. Thicker samples show increased scatter, especially at shorter wavelength. Surface scans are benchmarked using a variety of techniques, but power spectral density analysis is shown to be the

best predictor of scatter loss for most samples. The best growth conditions and a super polished substrate yield a scatter loss of 6.7ppm for a single layer and 12.3ppm for an output coupler which is comparable to commercially available output couplers.

Acknowledgements

This work was supported by the Office of Naval Research and Joint Technology Office from the United States Department of Defense.

The PCI data presented was taken at Stanford University by Dr. Ashot Markosyan. Dr. Dinesh Patel helped in creating the samples and calculating deposition rates. XRD data was taken by Dr. Pat Mccurdy. I thank my friends who worked with me on this thin film study as well as others: Dr. Dinesh Patel, Peter Langston and Erik Krous. I appreciate the work of my committee members, Dr. Azer Yalin and Dr. Mario Marconi for their help and consideration.

I also thank my adviser, Dr. Carmen Menoni for her support and guidance throughout my time at CSU and especially during the completion of the experimental work and many revisions of this thesis.

Contents

Chapter 1

Project background and theory

This chapter provides the background and theory necessary to understand the motivation for the work presented in this thesis aimed at investigating scatter loss in hafnium oxide (hafnia) thin films and multi-layer coatings. Section 1.1 gives a brief background of the thin film project at Colorado State University and provides the motivation for improving surface roughness. Section 1.2 provides a brief introduction into dielectric thin film coatings for optical applications. Section 1.3 briefly discusses the main methods for depositing optical thin films, including the method used at CSU - dual ion beam sputtering. Section 1.4 discusses origin and measurement of surface roughness, interface roughness and defects that cause scatter loss in optical thin films, with a particular emphasis on previous work reducing surface roughness in films created in dual ion beam sputtering systems. Section 1.5 discusses measurement of light scatter from optical elements and provides mathematical formalisms necessary to understand the rest of the thesis. Section 1.6 quantitatively and qualitatively discusses the link between the physical sources of scatter and the magnitude and angular distribution of scattered light.

1.1 Project background and motivation

This section aims to provide a brief overview of the motivation for and progress in work towards improvements to optical thin films conducted at Colorado State University (CSU). Recently, the work at CSU has focused on HfO_2 as a high damage threshold, high index material for use in dielectric stacks. Multilayer optical coatings are becoming ever more ubiquitous in cutting edge optical systems. Of particular interest are coatings used in dielectric cavity mirrors in high power pulsed lasers operating in the near infrared (NIR) region of the electromagnetic spectrum. Performance requirements for these mirrors are very stringent; these state-of-the-art lasers are have ever higher pulse energy and lower pulse duration and consequently significantly increased peak power.

Higher peak power creates a number of tighter requirements on the cavity mirrors. If the peak power per unit area (fluence) increases above some threshold, the coating is damaged. The fluence at which the coating exhibits damage is called the laser induced damage threshold (LIDT) and is an important value for evaluating the usefulness of a coating in high powered laser cavity mirrors. Also, each time a the pulse reflects off of a cavity mirror, some of the pulse energy is absorbed. This is called the absorption loss and must be minimized for optimal power output. Absorbed energy heats the cavity mirrors, which causes thermal lensing and coating degradation. The absorbed energy is removed from the pulse, which also limits the degree to which the pulse can be amplified. Similarly, a portion of the incident light pulse is scattered on each reflection. As with absorption, this constitutes a loss to the pulse energy. The scattered light can also travel back through the gain medium and become amplified, reducing the amount of pump power that is available for the main beam. Cavity mirrors should also be able to last for a long time and be resilient to changing temperature and humidity conditions (environmentally stable).

The materials used in cavity mirrors must therefore exhibit low absorption and

scatter loss, have a high LIDT and be environmentally stable. This combination of requirements makes material choice quite difficult. HfO_2 matches these requirements well, particularly because its damage threshold is quite high compared to other materials. This increased damage threshold can be partially attributed to a larger bandgap (>5eV for HfO_2 vs <4eV for Ta_2O_5 and TiO_2).

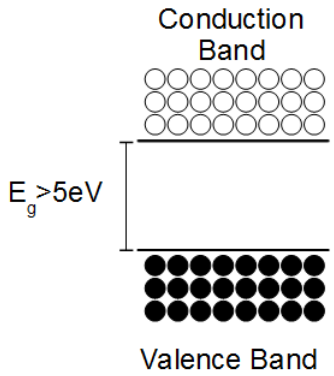

Figure 1.1: A band diagram of HfO_2 (a typical wide bandgap dielectric). The valence band is fully occupied and the conduction band is completely empty.

Figure 1.1 shows a band diagram of a dielectric material such as HfO_2. Due to the large bandgap of the material, the conduction band is nearly completely unpopulated. For an electron to be promoted into the conduction band, an amount of energy that is greater than the bandgap must be given to the electron. In dielectric materials, band to band absorption is negligible at mid-infrared wavelengths. In the NIR photons have less than 1eV of energy, and so single photon absorption cannot take place in dielectric materials. This is why these materials are transparent at visible and NIR wavelengths. However, electrons can still be promoted into the conduction band through a process called multi-photon absorption in which several photons act together to promote the electron to the conduction band. In amorphous dielectric materials, defects can act to effectively lower the bandgap. The defects can allow multiphoton absorption to take place with fewer photons, and thereby increase absorption and decrease LIDT. Multiphoton absorption is also dependant on fluence and pulsewidth[16]. A diagram

of each of these processes is shown in figure 1.2.

HfO_2 does have some limitations as a material. Intrinsic stress and surface roughness tend to be higher in HfO_2 than in other materials[23]. Stress can lead to decreased useful lifetime and sample deformation. Surface roughness increases scatter loss, and can increase LIDT at very high roughness values, though whether that trend continues to sub 0.5nm surface roughness is not clear[26].

Environmental stability, defect concentration and the optical qualities depend significantly on the deposition technique. Samples at CSU are deposited using dual ion beam sputtering (DIBS). DIBS is a desirable technique because it creates dense coatings that are environmentally stable and relatively free of defects. DIBS is discussed more thoroughly in sections 1.3 and 2.1.

Previous work at CSU in collaboration with the University of New Mexico (UNM) and Stanford recently has focused on reduction of absorption loss and increasing increasing LIDT. Different process parameters such as oxygen partial pressure have been related to LIDT. Single pulse and multiple pulse LIDT has been modeled using a rate model assuming trapped states within the bandgap[38]. Post-deposition annealing of samples has been shown to increase LIDT and reduce absorption by reducing occupied shallow defect states[42, 12]. The effect of assist beam energy on the structural properties of HfO_2 thin films was investigated[44]. This investigation showed a myriad of structural improvements to the film from increased assist beam energy including reduced stress, micro-crystallinity and surface roughness.

However, the surface roughness of HfO_2 films remained high and total loss measurements coupled with low absorption measurements implied that scattering loss was likely quite high. Anecdotal evidence of high scatter from HfO2 coatings particularly at short wavelengths was also provided by multiple sources. This combination of evidence prompted an investigation into the scatter properties of the HfO_2 films as well as an investigation into further reduction of surface roughness through deposi-

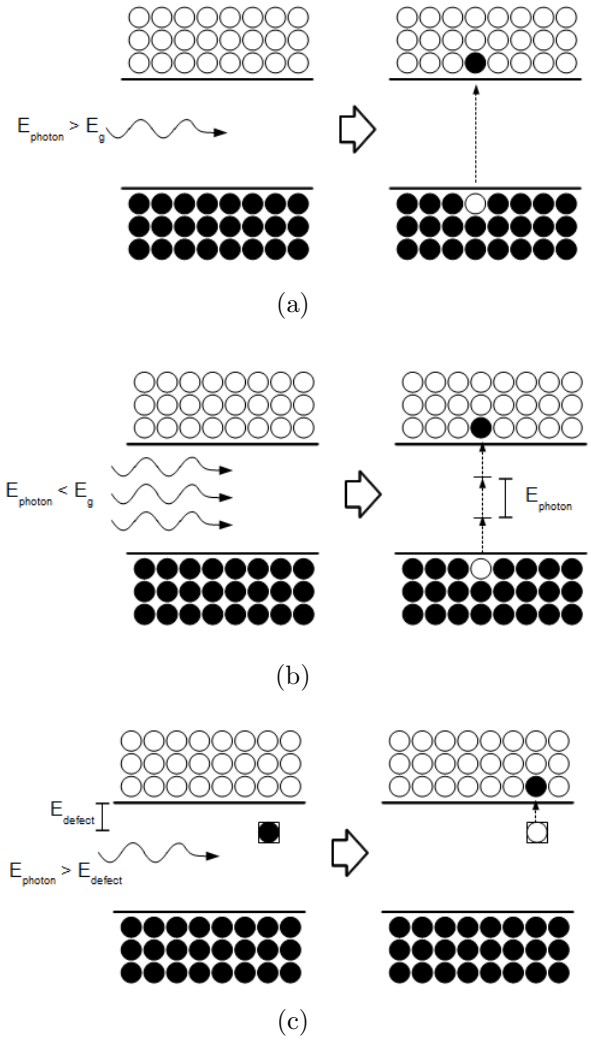

Figure 1.2: A band diagram describing the different absorption processes that can occur in dielectric materials. (a) shows single photon absorption. This process can only take place if the photon energy (E_{photon}) is greater than the bandgap energy (E_g). For wide bandgap materials such as HfO_2 this process can only take place at and below UV wavelengths. (b) shows multi-photon absorption. This process can occur in wide bandgap dielectric materials, but requires a large fluence. (c) shows absorption due to occupied shallow defects in the bandgap. This process can occur in wide bandgap dielectrics and likely accounts for most of the absorption by HfO_2 at low photon energies.

tion process parameters. This work includes design and construction of a device to measure scatter loss at multiple wavelengths with part-per-million (PPM) sensitivity, and its use in characterizing sets of coatings with different substrates, film thicknesses and deposition process parameters.

1.2 Dielectric interference coatings

Dielectric interference coatings are stacks of thin films that can be tailored to have specific optical properties. The coatings are grown on substrates with smooth super-polished surfaces(such as glass, quartz or silicon), and are typically 100s of nanometers thick. The materials used depend on the intended wavelength of light, but are typically oxides or fluorides for use in the visible/IR and UV respectively. In each case, the coating modifies the spectral transmission and reflection of the optic it is deposited on by increasing the reflectance in one region of the spectrum while lowering it in another. The requirements on these multilayer systems is often quite stringent. For example, in some applications, reflectance as high as 99.999% and in others reflectance below 0.1% are required. In some filters, narrow notches of transmission or a sharp change in reflectance at a specific wavelength is required. These very specific optical properties can be achieved by carefully choosing materials and layer thickness. The best coatings are achieved through use alternating materials with large changes in index of refraction.

The function of multilayer stacks is contingent on the reflectance and transmittance at an the interfaces between layers and the constructive or destructive interference of the light reflecting off of these interfaces. It is therefore important to find a quantitative way to predict the reflection and transmission coefficients of interfaces between layers as well as an effective transmission and reflectance for the entire multilayer.[36] First consider a single interface between two a semi-infinite materials

(figure 1.3 (a)). The reflection of light from a single interface can be calculated from:

$$R = \left(\frac{\eta_0 - \eta_1}{\eta_0 + \eta_1}\right)^2 \tag{1.1}$$

η_0 is the optical admittance of the starting medium and η_1 is the optical admittance of the second medium. Optical admittance is defined as $\eta = H/E$. In the optical regime, the optical admittance of a material depends on the index of refraction n and is different for s and p polarized light.

$$\eta_p = \frac{n\Upsilon}{\cos(\theta_t)} \tag{1.2}$$

$$\eta_s = n\Upsilon\cos(\theta_t) \tag{1.3}$$

$\Upsilon = \sqrt{\frac{\epsilon_0}{\mu_0}}$ is the optical admittance of free space. The calculation becomes more difficult when more than one interface is involved, especially if the distance is lower than the coherence length of the illumination, which is always the case for multilayer mirrors. Figure 1.3 (b) shows a thin film on a substrate in which there are two interfaces. The reflectance can still be calculated from the optical admittance, though it is now more complicated. The two interfaces work together to reflect the light, so an effective admittance of the sample can be calculated. The effective admittance Y can be calculated from the film admittance η_1 and the substrate admittance η_2. Because of the number of calculations, a matrix formalism is useful here. The matrix M is called the characteristic matrix for the layer.

$$Y = C/B \tag{1.4}$$

$$\begin{bmatrix} B \\ C \end{bmatrix} = M \begin{bmatrix} 1 \\ \eta_2 \end{bmatrix} = \begin{bmatrix} \cos\delta & (i\sin\delta/\eta_1) \\ i\eta_1 \sin\delta & \cos\delta \end{bmatrix} \begin{bmatrix} 1 \\ \eta_2 \end{bmatrix} \tag{1.5}$$

δ is a layer phase factor calculated from the film thickness, complex refractive index (N_1), wavelength and refracted angle (θ_1).

$$\delta = 2\pi N_1 d\cos(\theta_1)/\lambda \tag{1.6}$$

The reflectance and transmittance of the entire sample can then be calculated by [36]:

$$R = \left(\frac{\eta_0 - Y}{\eta_0 + Y}\right)\left(\frac{\eta_0 - Y}{\eta_0 + Y}\right)^* \tag{1.7}$$

$$T = \frac{4\eta_0 \mathrm{Re}(\eta_m)}{(\eta_0 B + C)(\eta_0 B + C)^*} \tag{1.8}$$

This process can then be generalized for film stacks with any number of layers by adding layer matrices accordingly. The generalized version of the matrix equation 1.5 for a system with k layers is:

$$\begin{bmatrix} B \\ C \end{bmatrix} = \mathrm{M}_1\mathrm{M}_2...\mathrm{M}_l...\mathrm{M}_{k-1}\mathrm{M}_k \begin{bmatrix} 1 \\ \eta_{sub} \end{bmatrix} \tag{1.9}$$

where

$$\mathrm{M}_l = \begin{bmatrix} \cos\delta_1 & (i\sin\delta_l/\eta_l) \\ i\eta_l \sin\delta_l & \cos\delta_l \end{bmatrix} \tag{1.10}$$

$$\delta_l = 2\pi N_l d_l \cos(\theta_l)/\lambda \tag{1.11}$$

Y is still calculated from equation 1.4. Transmittance and reflectance of the sample can still be calculated using 1.7. One important note is that for transmittance to have any meaning, all the materials must have very low absorption[36].

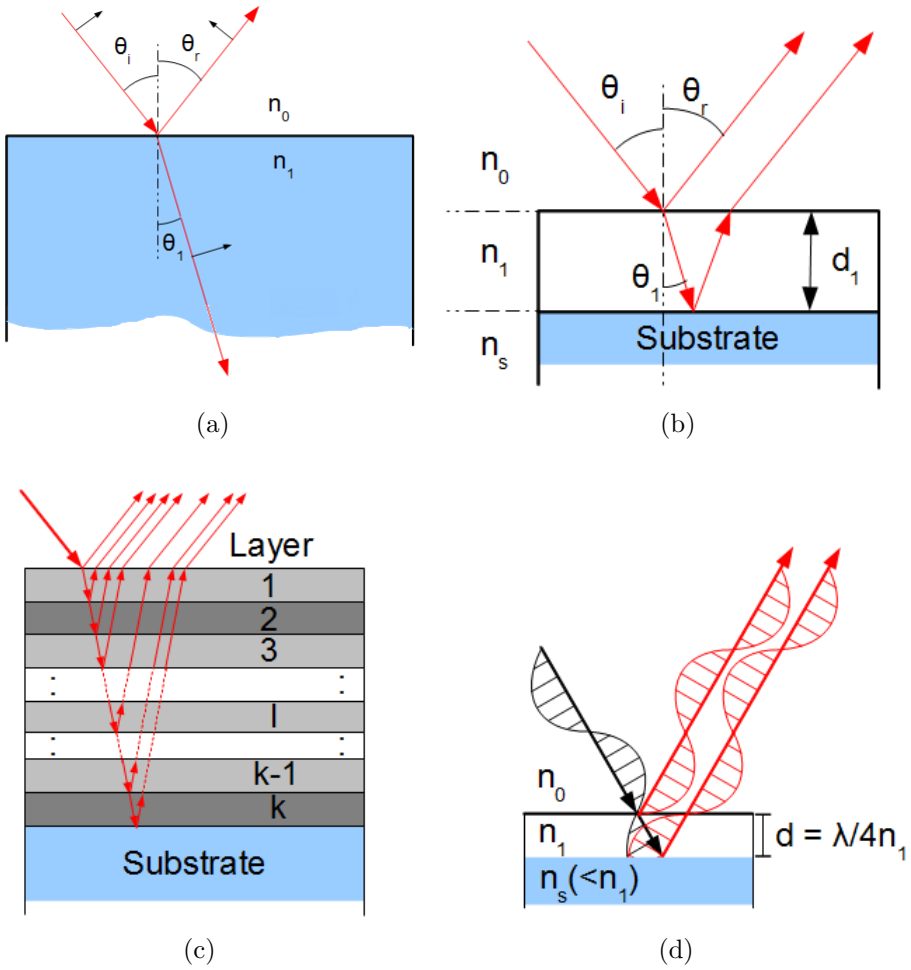

Figure 1.3: (a)Light partially reflecting at a dielectric interface. Black arrows indicate the electric field direction for p polarized light (b) Light reflecting from both interfaces of a thin film on a substrate. (c) light reflecting from many many interfaces of a coating with k layers. (d) Constructive interference from a $\lambda/4n$ thickness film.

The reflectivity of an HR coating is maximized when many alternating layers with different indexes of refraction are deposited with an optical thickness of $\lambda/4$ per layer (ie a physical thickness of $\lambda/4n$). The reflectivity of a single layer is maximized when the optical thickness of the film is $\lambda/4$ because the reflected light from the two interfaces interfere constructively as shown in figure 1.3 (d). Note that the constructive interference occurs because there is a 180deg phase shift when the wave is reflected from a high index layer into a low index layer. No phase shift occurs for the reflection from a low index layer into a high index layer.[36] If another layer with a different index of refraction is coated on top of the first, the reflectivity is increased again. This process is repeated until the desired reflectivity is achieved. The reflectivity of a $\lambda/4$ dielectric stack at the wavelength λ can be calculated by[36]:

$$R = \left(\frac{1 - (n_h/n_l)^{2p}(n_h^2/n_s)}{1 + (n_h/n_l)^{2p}(n_h^2/n_s)} \right)^2 \tag{1.12}$$

Equation 1.12 shows that reflectivity increases with increasing contrast between n_h and n_l and with p (the number of bilayers). So, the best ways to increase reflectance in a multilayer stack is to chose materials with significantly different indexes of refraction and by increasing the number of layers. However, increasing p also increases the number of interfaces and as such potentially increases the amount of scattered light. Figure 1.4 shows calculated reflectance spectra for $\lambda/4$ HR coatings with different numbers of bilayers, and peak reflectivity calculated as a function of number of bilayers.

Material choice is also tricky. Most materials used currently are metal oxides. For low index of refraction, SiO_2 is generally used, though Al_2O_3 is also sometimes used. Several high index materials are used, though each have benefits and drawbacks.

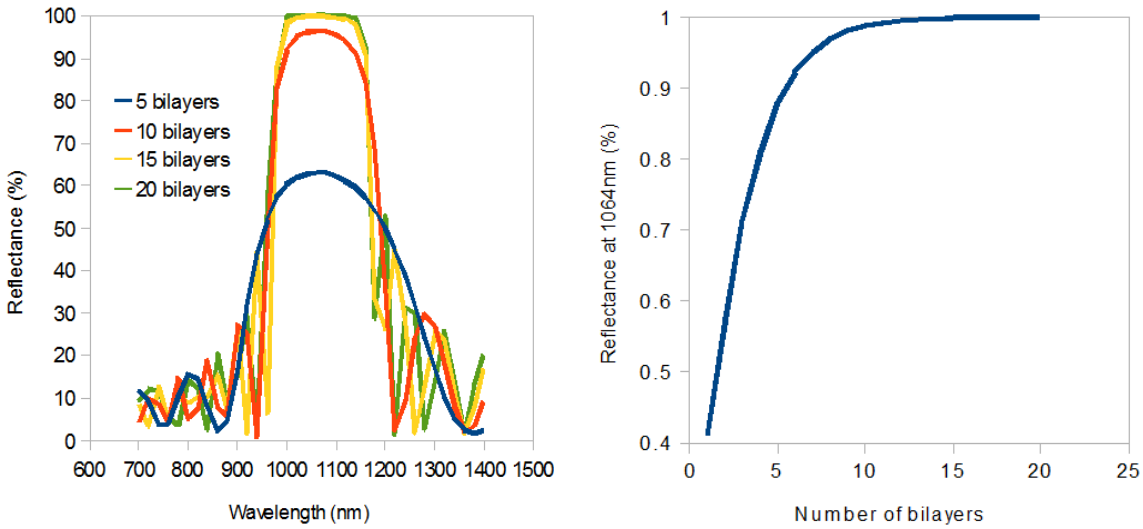

(a) (b)

Figure 1.4: (a) Calculated reflectance as a function of wavelength for different numbers of bilayers, (b) calculated peak reflectance as a function of number of bilayers.

Material	n(λ =1064nm)
SiO_2	1.59
Ta_2O_5	2.08
ZrO_2	2.07
HfO_2	2.02
Al_2O_3	1.65
Sc_2O_3	1.95
TiO_2	2.49

Figure 1.5: Thin film refractive indices (measured at CSU).

HfO_2, Ta_2O_3, Sc_2O_3 and ZrO_2 have all been used successfully. Table 1.5 shows a list of materials with indexes of refraction at one micron wavelength. Other properties such as damage threshold, absorption, intrinsic stress, roughness, cost and ease of deposition must be considered when choosing materials as well.

Multi-layer coatings can be designed to reduce reflection. This type of coating is called an anti-reflection (AR) coating. AR coatings can have a variety of configurations but typically involve the same sets of high and low index materials as HR coatings.

1.3 Optical thin film deposition

This section briefly presents the main techniques that are used to deposit dielectric films for optical applications. Thin films can be deposited using several different techniques, each of which has its own benefits and drawbacks. Thin film deposition can be divided into two main categories, physical deposition and chemical deposition. In chemical processes, two or more gasses or liquids react along a surface to form a solid film. In physical processes a vapor phase plume of material which is created by physical means such thermal energy transfer or momentum transfer condenses on a surface to form a thin solid film. Many variants of both chemical and physical deposition exist including some hybrid processes.

A common chemical deposition process is chemical vapor deposition (CVD). In CVD processes, multiple gasses that contain the required "building blocks" for the final film are injected into a vacuum chamber and flowed along the substrates. These precursor gasses react or decompose at the surface producing a thin film. As a bi-product, reactive gasses made up of unused parts of the decomposed precursor gasses are created. These bi-product gasses are usually very reactive, and must be quickly removed from the chamber. Removal of the gasses is accomplished by flowing an inert

gas along with the precursor gasses[11].

CVD processes can produce films that have several desirable attributes. Films exhibit high packing density, good stoichiometry and conform well to non-uniform surface (which is not true of most physical deposition processes which are directional). CVD has the disadvantage of creating films with tensile stress, and having defect concentrations related to the purity of the precursor gasses. Material choice is also a problem as somewhat stable and cheap pre-cursor materials have not been found for all materials[11].

A common variation on CVD is an epitaxial process called atomic layer deposition (ALD). In ALD, the precursor gasses are flowed in separately. During each pulse, a single atomic layer of the material is deposited. Between pulses, the chamber is purged. The precursor gasses are designed so that they react to form the desired compound[1]. ALD is a particularly slow deposition technique but allows very precise control of film thickness and creates films that are very uniform over large areas[7].

Physical deposition techniques can be divided into evaporation and sputtering. In evaporation deposition, a vapor of film material is created thermally. The energy to evaporate the film can be delivered by running a current through container holding the sample material. The container is heated resistively which heats the sample material. A vapor phase plume of sample material is created which condenses on the substrates. The plume is highly directional, so the substrates must be rotated to avoid non-uniformity [41].

Material can also be evaporated through the use of a directed electron beam. The electron beam is a more efficient way to evaporate because it deposits all of its energy in a specific area. Evaporation using electron beams has the added benefit of reducing the amount of material from the container that can evaporate and become incorporated into the film as defects[9].

Evaporation is a fast technique, but has the disadvantage of creating films that

are not dense or porous. Porous films are less environmentally stable. The refractive index shifts with humidity as water adsorbs to the film. The density of the films can be increased by adding energy to the system through the use of an ion beam assist source. In ion beam assisted deposition (IBAD), an ion source is aimed at the substrates during deposition which increases the mobility of atoms in the coating. The increased mobility allows for decreased porosity and therefore increased index of refraction and environmental stability. The simplicity and speed of this process make it very popular for high throughput coating deposition[11][35].

Vapor can also be created through momentum transfer in a process called sputtering. During sputtering atoms are removed from near the surface of a solid by energetic ion bombardment [53]. The material under bombardment is called the target. Energetic ions are usually created by ionizing an inert gas such as Ar and accelerating them towards the target. The Argon ions can be created through a number of means, but it is usually some sort of plasma.

One common type of sputtering is magnetron sputtering. In magnetron sputtering, the target is kept at a large negative bias compared to the chamber ground. Large magnets are placed near the target such that there is a large magnetic field perpendicular to the electric field created by the biased target. An inert gas is flowed into the chamber along with some electrons to start the plasma. The electrons are accelerated away from the target, but the magnetic field causes them to spiral due to the Lorenz force. The spiralling energetic electrons eventually collide with and ionize the sputtering gas. This creates additional electrons that are also accelerated. Eventually this develops into a stable plasma near the target. The ionized atoms from the inert gas are accelerated towards the target and eventually hit the target with a large amount of energy, removing some target atoms. The target atoms form a vapor phase plume which is directed towards the substrates. Due to the directionality of the target atoms, the substrates must be rotated to achieve uniformity[53].

In ion beam sputtering, the ions are created in a separate discharge chamber. A plasma is created using an RF coil around the discharge chamber. The ions are accelerated towards the target using a biased grid system. This process allows more control over the characteristics of the sputtering ions (directionality, energy and flux) and separates the plasma from the substrates[27]. The process can also be conducted at lower pressures which lessens the likelihood of defect incorporation. Ion beam sputtered films have been shown to have high damage threshold, low absorption and scatter loss and good environmental stability[35].

Both ion beam sputtering and magnetron sputtering can also be used in conjunction with an assist ion beam aimed at the substrates as in IBAD. Magnetron sputtering with an assist ion beam is known as ion assisted magnetron sputtering. Ion beam sputtering with an assist ion beam is known as dual ion beam sputtering[27].

All the samples created for this thesis were deposited using dual ion beam sputtering (DIBS). Chapter 2 describes the deposition device in more detail.

1.4 Physical origins of scattered light from thin films

This section provides a qualitative discussion of some of the physical features in thin films that lead to scattering of light. A more explicit quantitative analysis of the these physical features on the scatter properties is conducted in section 1.6.

The most significant source of scattered light in optical thin films is generally surface roughness[14]. Surface roughness is comprised of many different features which may originate in the substrate surface or from the coating. Scattering causing surface features can include polishing marks and blemishes, random height fluctuations, localized defects such as dust, nano-crystallinity, and splatters from uneven coating. Each of these types of features affect the scatter properties of the film differently.

Consider first a glass substrate polished for optical coatings. Even very highly polished surfaces have some leftover scratch marks and pits which contribute some to the roughness. In addition to the scratches and pits, there are also random fluctuations in surface heights. There is a broad distribution in the lateral size of these fluctuations. The features that are at or above the wavelength of light are of most interest. For features much larger than the wavelength of light, geometrical scattering can be predicted by looking at the slope of the feature and predicting the geometry of the transmitted and reflected rays through the use of equations 1.16 and 1.17.

Once a coating is deposited on the substrate, the surface profile evolves. The coating may smooth out some of the scratches, pits, and high spatial frequency roughness, likely reproducing most of the broader features of the surface. The coating also typically introduces smaller features depending on the material.

For transparent samples, surface roughness on both sides of the sample must be included. Quantitatively predicting the role that scattering from the back surface plays can be difficult and depends on the optical properties of the sample. In the case of an anti-reflection coating, the back surface and front surface play very similar roles. In the case of a high reflection coating, the front surface and interfaces account for nearly all scatter light.

Another potentially significant source of scatter is interface roughness. This can be both roughness between the substrate and the coating as well as between layers in the dielectric stack. The amount that interface roughness contributes to the total scatter loss depends on several factors, which is discussed further in section 1.4.2. Finally, localized large defects (section 1.4.4) and small bulk defects (section 1.4.3) play a role in scattering light as well and are discussed more thoroughly later.

Much more is known about surfaces because several techniques exist to directly profile surfaces. These techniques include mechanical techniques (surface profilometry, atomic force microscopy) and optical techniques (white light interferometry).

Atomic force microscopy (AFM) and white light interferomtry (WLI) give a 2D map of surface heights which can then be used to calculate statistics about the surfaces (discussed furthur in section 1.4.1). These statistics are good for quantifying the random roughness, but do not do a good job of finding localized defect concentrations. Dust particles and localized defects can be large enough to show up when the sample is examined under a Nomarski microscope or with a technique called total internal reflection microscopy (TIRM). Section 1.4.4 gives a bit more detail on techniques to measure localized defect concentrations. Interface roughness (section 1.4.2) cannot be directly measured in a completed thin film, but techniques such as ellipsometry, grazing incidence x-ray reflectivity and angle-resolved scatter measurements can give some insight into the magnitude and spatial distribution of scattering. The amount of scattering from bulk defects is generally very low, but is discussed in section 1.4.3.

1.4.1 Surface roughness measurements of optical coatings

Surface maps can be be achieved using atomic force microscopy (AFM) and white light interferometry (WLI). These maps can be analysed to create useful benchmarks to compare surfaces quantitatively. This section describes the most common parameters used to judge the quality of optical surfaces: scratch/dig, flatness, root mean squared (RMS) roughness, correlation length, autocorrelation function and the power spectral density function.

A common parameter used to judge the quality of substrates is scratch/dig. The scratch value is calculated by measuring the width of the scratches found in the surface: Scratch $= W \times 10\mu m$ where W is the width of the largest scratch found. Ie, a scratch value of 30 means that the maximum scratch width is $3\mu m$. The dig value is calculated similarly except that it measures the diameter of pits instead of the width of scratches. The scratch/dig value is actually not very useful in understanding scattering because the amount of light scattered is independent of the width of flat

bottomed pits and scratches while random roughness in the non scratched areas of the coating can contribute significantly to scattered light[14].

Another commonly used parameter is the sample flatness. Flatness is the the amount that the mean surface height fluctuates per inch of sample diameter. Flatness is useful in short pulse lasers and interferometers where wave-front distortion can be a problem, but is not a good indicator of how a sample scatters light. Flatness is often given in units of 'waves' at $\lambda = 632nm$. Flatness requirements depend a lot on the application but $\lambda/10$ is typically sufficient and not difficult to achieve[21].

Instead of scratch/dig and flatness, a parameter called root mean squared (RMS) roughness is more commonly used. RMS roughness is very useful in most situations, though it can be misleading if used in the absence of other information . Typically, an optically smooth surface has a Gaussian distribution of surface heights. This is referred to as "random roughness". For samples with Gaussian height distributions an RMS roughness value can be calculated using:

$$\sigma_{RMS} = \sqrt{\frac{1}{MN} \sum_{k=0}^{M-1} \sum_{l=0}^{N-1} \left[H\left(x_k, y_l\right) - \mu\right]^2} \tag{1.13}$$

Where M and N are the dimensions of the array H and μ is the mean height of the surface. σ_{RMS} can be basically thought of as a parameter describing the average height of features on the surface and is by far the most used parameter in characterizing surfaces. σ_{RMS} can be correlated directly with scatter loss in certain situations (see section 1.6) and is therefore a good first order benchmark of the quality of the surface. However, there are limitations in how much can be learned from just the distribution of heights.

The transverse size of the surface features must also be considered, especially in determining the angular distribution of the scattered light. Coming up with a simple and meaningful parameter to describe transverse feature size is complex. The way that is typically employed is through the use of an autocorrelation function. The

autocorrelation function is a function that describes the degree of correlation between two surfaces height maps $H(\vec{r})$ and $H(\vec{r}+\vec{d})$ where $H(\vec{r}+\vec{d})$ is $H(\vec{r})$ shifted laterally by the vector $\vec{d}$. The x-axis is the magnitude of the lag distance ($|d|$) and the y axis is the average magnitude of the correlation between the surfaces as a function of the lag distance[14]. At $|d| = 0$, $H(\vec{r}+\vec{d}) = H(\vec{r})$ and the surfaces are perfectly correlated so the autocorrelation function equals one. As $|d|$ increases, the degree of correlation drops depending on the transverse size of the features. The point at which the autocorrelation function drops to $1/e$ is known as the correlation length (τ_c) and can be thought of as describing the transverse size of the features[14].

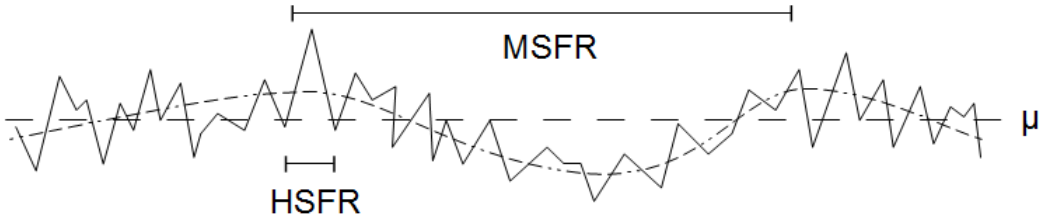

Figure 1.6: Surface roughness is a convolution of features with many different spatial frequencies. A constructed profile with a range of spatial frequency roughness components is shown. The overall height average μ is shown.

Still more information can be gleaned by looking at the autocorrelation function in the spatial frequency (or Fourier) domain. The power spectral density function (PSD) is the fourier transform of the autocorrelation function. Similar to other forms of Fourier analysis, the surface can be described as a summation of many sin functions at different frequencies. In this case, these are spatial frequencies which are defined as the inverse of the distance between two consecutive peaks of the sin function and are usually presented in units of μm^{-1}. The PSD at a particular frequency is the amplitude of the sin function at that spatial frequency and is often described as the 'roughness power' of features at that spatial frequency. An example PSD for silicon and molybdenum multi-layers on glass substrates is shown in figure 1.7.

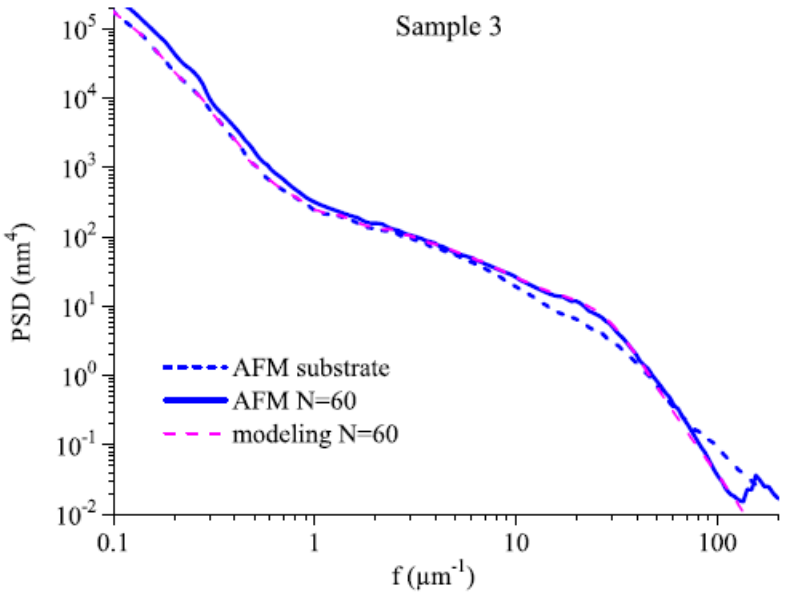

Figure 1.7: An example PSD for silicon/molybdenum multilayers on glass substrates.

The bandwidth limited RMS roughness of a surface can be calculated from the PSD using equation 1.14.

$$\sigma_{RMS} = 2\pi \int_{f_{min}}^{f_{max}} PSD\,(f)\, f df \tag{1.14}$$

where the PSD is the power spectral density function of the surface and f are the spatial frequencies of the roughness. If the limits $f_{min} = 0$ and $f_{max} = \infty$ roughness calculated by equation 1.14 is equivalent to the RMS roughness calculated in equation 1.13. If different limits are chosen, a band-width limited roughness can be calculated which can be very useful in determining the scatter properties of a film (see section 1.6).

Generally, the spatial frequencies are split into three categories (shown in figure 1.8). Examining how the PSD changes in different ranges can give insight into how scatter loss changes as a function of the wavelength of illumination. MSFR is particularly important in visible and near to mid-infrared scattering from coatings[50]. HSFR is only important for very short wavelengths (UV through soft x-ray).

	Spatial frequency range	$\lambda(\mu m)$
Low spatial frequency roughness (LSFR)	0 - 0.001 μm^{-1}	> 3
Mid spatial frequency roughness (MSFR)	0.001 - 1 μm^{-1}	$0.2 - 5$
High spatial frequency roughness (HSFR)	1 - ∞ μm^{-1}	< 0.4

Figure 1.8: Definitions of different spatial frequency ranges.

1.4.2 Roughness evolution and interface roughness

Roughness evolution

The surface roughness of a film is a convolution of the substrate surface and the coating roughness. As each successive layers is deposited, the surface changes. The coating may smooth out some spatial features while exacerbating others. For smooth films such as Ta_2O_5 and SiO_2, typically there is an enhancement of HSFR and some minimal smoothing in the MSFR, leading to a decrease in roughness when coated on mid quality substrates (RMS $\sim 0.6nm$) and a slight roughening effect on super-polished substrates (RMS $\sim 0.1nm$).

Growth models can be derived to quantify the surface evolution from one layer to the next. A growth model that has been shown to be accurate is a linear growth model that treats evolution of roughness at each frequency separately. Mathematically, that can be seen in equation 1.15.

$$\mathrm{PSD}_n(f) = \mathrm{PSD}_{int,n}(f) + \alpha_{rep,n}(f)\mathrm{PSD}_{n-1}(f) \tag{1.15}$$

where $\alpha_{rep,n}(f)$ is function showing the degree to which the layer smooths out roughness from the previous layer, PSD_n is the power spectral density function of the n^{th} layer, $\mathrm{PSD}_{int,n}(f)$ is the power spectral density of the roughness intrinsic to the

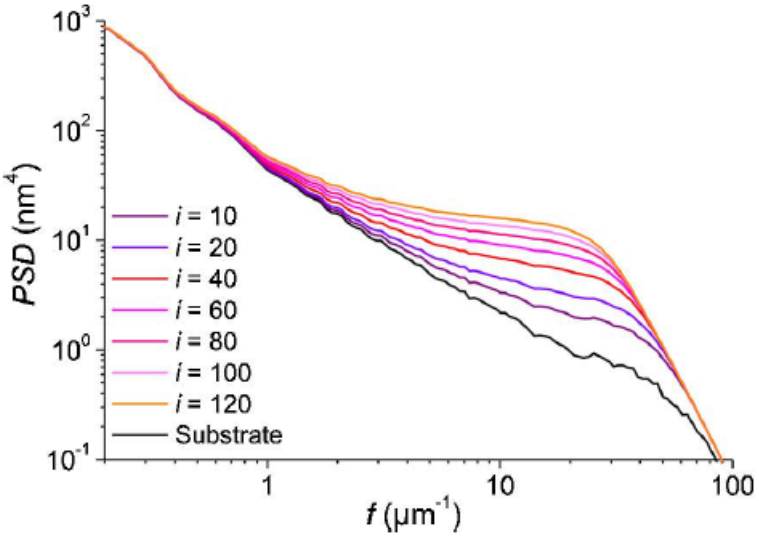

Figure 1.9: A series of PSDs for Mo/Si multi-layers with a different number of bilayers. This shows that the roughness evolves with the number of layers, increasing in high spatial frequencies and staying constant at lower spatial frequencies.[51]

n^{th} layer.and f is the spatial frequency. $\alpha_{rep,n}(f)$ is dependent on material, process, layer thickness and other parameters and must be measured empirically. This process can be iterated to predict the roughness of a completed coating at each layer, though $\alpha_{rep,n}(f)$ must be alternated if the multiple materials are used[51]. Figure 1.9 shows a series of PSDs for multilayers with increasing numbers of bilayers. The roughness is increased consistently at high spatial frequencies but remains constant at the lower spatial frequencies.

Interface roughness

Interface roughness is another important factor in determining the scattering performance of a coating, though it is not as simply understood as surface roughness. Intuitively, one would expect each interface to act independently and scatter a similar amount of light. Given that the roughness evolves from one surface to the next as described in the previous section, this would seem to indicate that multi-layer stacks would scatter a significantly larger portion of the light than single layers. Luckily this

turns out not to be the case.

Individual layers act together rather than independently and the degree of correlation between layers is more important than the actual roughness at individual interfaces. A coating where all the interfaces are perfectly correlated can be modelled as a single surface. If the layers are not perfectly correlated as is typically the case, the scattering value is higher than otherwise predicted by the single interface approximation. As mentioned in the previous section, the roughness increases at different rates for different spatial frequencies according to the smoothing function . Spatial frequencies where the PSD is enhanced by the coating tend to create uncorrelated roughness, whereas spatial frequencies that don't change with the coating (which are driven by the substrate roughness) tend to stay correlated through the entire stack. Since different wavelengths interact with different spatial frequency roughness for scatter purposes, multi-layer stacks can have significantly different scatter performance at different wavelengths[8].

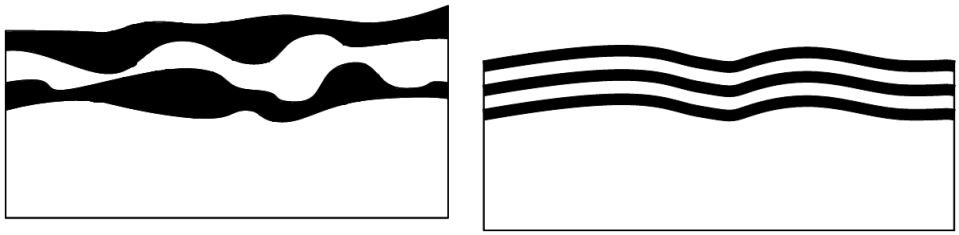

(a) (b)

Figure 1.10: Drawing of (a) partially uncorrelated and (b) correlated layers.

Oxide coatings tend to show less roughness enhancement per layer at mid spatial frequencies and thus stay more correlated. Mid spatial frequencies are also the frequencies most important especially for NIR and to a lesser degree visible scattering, meaning that performance should be close to that of the substrate even for HRs with many bilayers[51].

Interface roughness can be measured using spectroscopic ellipsometry, and angle

resolved scatter (ARS) measurements. Ellipsometry is discussed more thoroughly in section 2.2.4. ARS is discussed in section 1.5.2.

Interface intermixing

Another phenomenon often confused with interface roughness is interface intermixing. Intermixing is different in that the actual molecules of each material diffuse across the boundary while there is still enough energy at the surface of the interface to allow for rearrangement. Because the regions in which materials are intermixed tend to be small both in height and laterally, intermixing does not scatter light the same way as interface roughness. Instead, it acts as an intermediate layer with a dielectric constant in between that of the two layers at the boundary. As such, it changes the spectral transmission and reflection properties of the interface. Typically this manifests as a slight increase in transmission due to lower index of refraction contrast[50]. Interface mixing is more critical in interference coatings used at wavelengths in the ultraviolet, extreme ultraviolet and x-ray regions.

1.4.3 Bulk defects

Bulk scattering is the scattering of light from defects within the coating and substrate. Within all amorphous films and substrates, there is some short range order or nano-crystallinity. The crystal size can be on the order of just a few atoms or up to a few nanometers. At the edges of these tiny crystals, there can be mismatches that cause dislocation defects or gaseous inclusions from the chamber during deposition. These discontinuity defects cause slight variations in the dielectric constant which can cause light to scatter. The defects are usually atomically sized and well below the wavelength of visible and IR light, so Rayleigh scattering theory can be effectively applied. Most optical components have low defect concentrations, and the defects do not cause significant disturbances to the refractive index. Scatter loss generated by

bulk defects is generally quite low compared to localized surface defects, surface and interface effects.

1.4.4 Localized defects and particulates

Another significant contributor to scatter light, especially on mirrors outside of a clean room environment is localized defects such as dust particles. These particles can be on the substrate before coating, can be included within the middle of the stack or on the surface. Deposition is usually accomplished in vacuum, so particle defects are usually on the surface. In some deposition systems such as evaporation, there is the possibility of large clusters of coating material arriving at the sample at the same time, creating large localized defects made up of coating material. [20]

The most common and detrimental type of localized defects are particles between 0.1 and 1 μm on the substrate underneath the coating. The coating generally conforms to the shape of the defect as layers are grown. Figure 1.11 shows this effect. Localized defects are particularly difficult to model because their size is generally in the same range as the wavelength of the light. In very controlled circumstances Mie theory (discussed further in section 1.6) and finite element analysis techniques have been able to accurately predict scattering values[48]. However, even a very developed Mie theory is not capable of fully predicting the magnitude and distribution of the scattering because of the large amount of the required parameters for the defects such as size, shape, concentrations, materials, refractive index, etc are unknown.[20] The problem becomes more complicated still when the defect is covered by a multi-layer coating. The relative importance of defects on scattering can be quite large, particularly in the infrared where the importance of scattering from random roughness drops off due to the $1/\lambda^2$ dependence [14]. At short wavelength, the scatter values from localized defects is washed out by the increase in scattering from random roughness. Localized defects have also been shown to be detrimental to damage threshold in part because

defects tend to have significantly higher absorption than the surrounding coating[54].

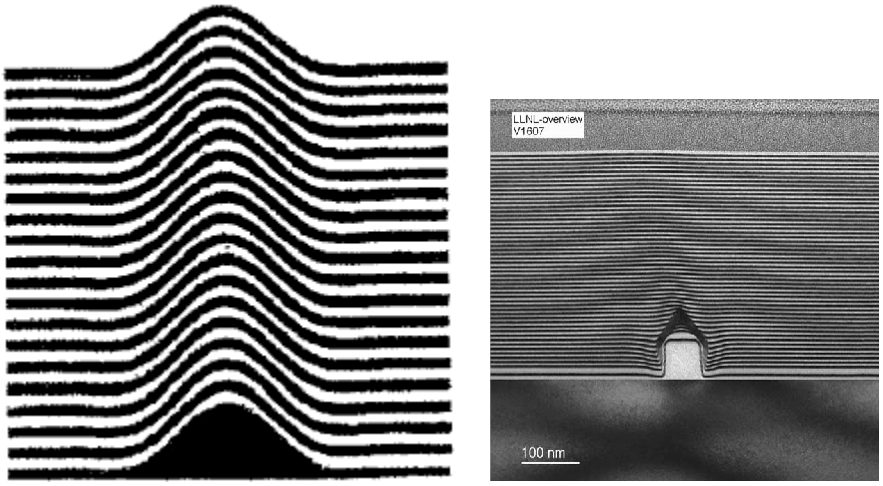

(a) (b)

Figure 1.11: (a) Drawing showing the effect of large localized defects on the substrate underneath a multi-layer coating.(b) TEM image showing the effects of smoothing of localized defects through off normal ion bombardment, image taken from [22].

Substrate preparation is the best way to mitigate the effect of localized defects. Substrate cleaning is generally performed in clean rooms filtered by HEPA and ULPA filters which do a good job of filtering out particles larger than 100 to 300 nm in size. The effect can also be lowered, particularly in high reflectors, through the use of off normal ion bombardment during deposition[40]. Figure 1.11 shows that defects can be almost completely removed in coatings with many layers[22].

1.4.5 Surface roughness from DIBS systems

There are many ways of depositing the oxide materials used in optical coatings. Each deposition technique and often each system has its own strengths, weaknesses and peculiarities even when growing films with the same materials. Not much work has gone into reducing surface roughness, though there are sporadic papers in the recent literature about in the main set of coating materials for the visible and NIR (HfO_2, Ta_2O_5, ZrO_2, Al_2O_3 and SiO_2), of which some has been on coatings from dual ion

beam sputtering[30, 56, 47, 32]. Though some basic relationships exist that are true for most deposition systems, the following paragraphs focus on work on coatings grown in dual ion beam sputtering deposition systems.

One of the main benefits of dual ion beam sputtering systems is that there are many 'knobs' that can be adjusted to achieve the desired coating attributes and optical performance. Of these knobs only some have an effect on surface roughness.

Low index materials (Al_2O_3 and SiO_2) exhibit by nature very little surface roughness and generally replicate the substrate surface at MSFR ranges and smooth out HSFR from the substrate. 0.1nm roughness surfaces have been demonstrated in both Al_2O_3 and SiO_2[33, 29].

High index materials have proven to be a bit trickier. Ta_2O_5 was the material of choice for some time, and as such has been studied more completely than others. Surface roughness in tantala films is generally very good, between 0.1 and 0.5 nm RMS.

Several systematic studies have been conducted of tantala growth parameters vs surface roughness. Yoon et al found that substrate temperature had an small effect on surface roughness, and that roughness was minimized at 150C (figure 1.12)[57]. In a 2008 paper Yoon et al[56] reported that RMS roughness decreased with increasing assist beam voltage up to about 550V, and then a steep increase from there (see figure 1.12). Kulisch et al showed no dependence of tantala surface roughness on oxygen partial pressure and a very good roughness value of 0.14 nm[30]. Annealing of coatings is a good way to reduce defects and absorption while increasing damage threshold. However, it also increases crystalline size and therefore surface roughness. Increasing annealing temperature can also significantly increase the surface roughness above a certain temperature[47]. Figure 1.14 shows results from Lee et al.[32]. These results show that changing the ratio of oxygen to argon in the assist source had some effect on the surface roughness, though the change is not significant. The same paper

showed a drop in roughness by increasing the assist beam voltage from 0V to 50V but no significant change after. This paper showed better results than were reported in [56] for the same experiment, but the voltage ranges were not the same.

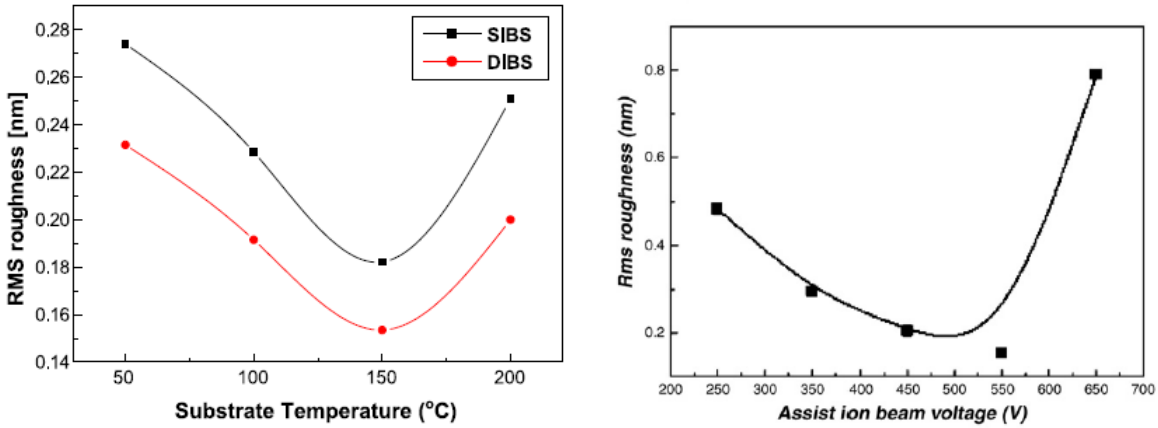

(a) Results from Yoon et al on rms substrate roughness vs substrate temperature.[57]

(b) Results from Yoon et al on rms substrate roughness vs assist beam voltage.[56]

Figure 1.12: Results from the literature on tantala film roughness.

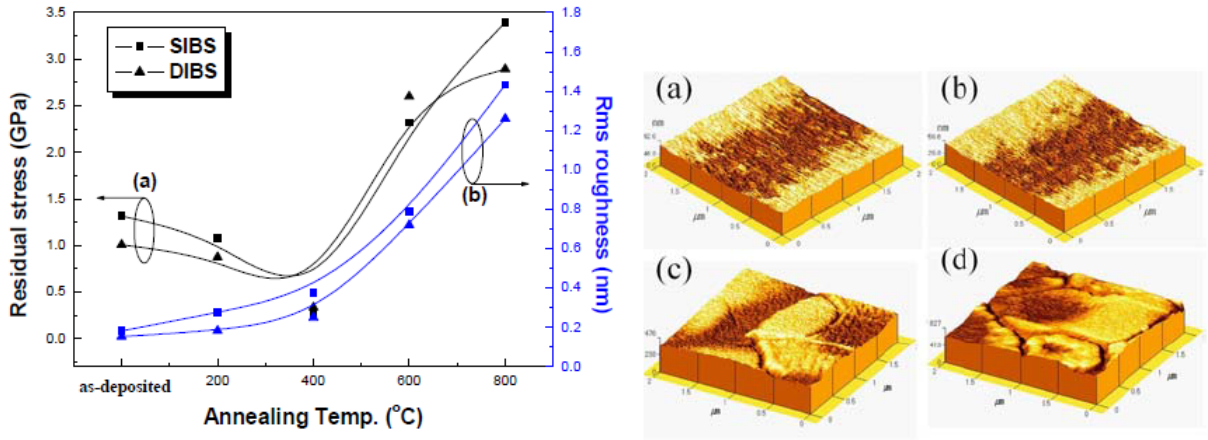

Figure 1.13: Annealing of Ta_2O_5 films increases surface roughness[47]. (c) and (d) show films annealed at 800C, (a) and (b) are the films as grown.

TiO_2 and ZrO_2 have received some attention, but the problem has not been approached as roundly as with tantala. Surface roughness studies of HfO_2 in particular

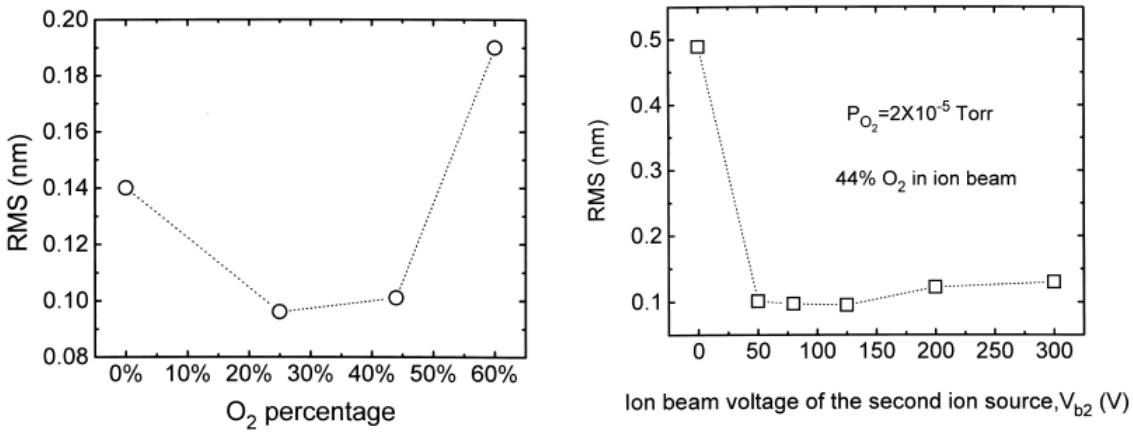

Figure 1.14: Results from Lee et al. [32]

are absent in the literature. Indeed, the only roughness data that has been published has been single values in studies of other film characteristics rather than focused roughness studies.

In a laser damage threshold study, Gallais et al [23] reported roughness values for hafnia films of multiple thicknesses grown using different techniques. For thin films (less than 100nm) the film was quite smooth and matched the RMS roughness of the substrate at 0.5nm. For thicker films (around 250nm thick) the RMS roughness value increased significantly up to almost 3nm. For thin films, DIBS was capable of matching the roughness values of other techniques. This value is significantly higher than that of other high index films.

1.5 Light scattering by optical elements and thin films

Scattered light from optical coatings can have a myriad of detrimental effects in optical systems. Any light scattered at an interface represents a loss of useful light from the main beam. This can be damaging in systems with many optics and particularly in

high power lasers. The scattered light can also cause a loss of contrast in imaging and lithographic printing systems and noise in other high sensitivity measurements[15, 28]. This section introduces the basics of scatter loss measurement.

1.5.1 General description of scattered light

In its most general form light scattering is the process by which the trajectory of an electromagnetic wave is made to deviate from a basic straightforward path. Light scattering by bound electrons in dielectric materials accounts for phenomena such as reflection and transmission of light at an interface and also governs the relative amplitudes of the transmitted and reflected light[24]. Consider figure 1.15 which shows a diagram of a beam of light at a partially transparent interface. P_r and $P_t$correspond to the power in specularly reflected and transmitted beams respectively. P_{bs} corresponds to the total power of the light reflecting off the interface, omitting the specularly reflected power. This is called the diffuse reflected power or backscattered power. P_{fs} corresponds to the power of the light transmitted through the interface, omitting the specularly transmitted light. This is called the diffuse transmitted power or foward scattered power. Assuming a perfectly smooth interface the trajectory of both transmitted and reflected light is predictable according to equations 1.16, 1.17 and P_{bs} and P_{fs} would be zero.

$$\theta_r = -\theta_0 \tag{1.16}$$

$$n_2 \sin(\theta_t) = n_1 \sin(\theta_0) \tag{1.17}$$

However, even the smoothest of surfaces have some non-uniformities which cause some of the impinging light to reflect diffusely. Because the surface is transparent a portion of the light is transmitted through sample, some of which is transmitted

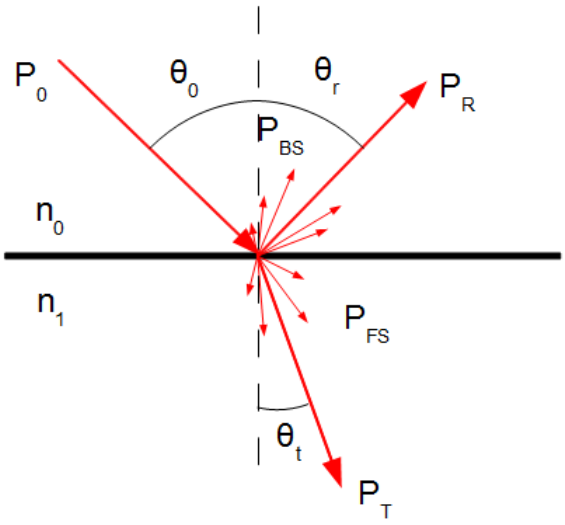

Figure 1.15: A depiction of scattered light approaching a partially transparent interface. Some of the light is reflected or transmitted specularly. The rest of the light is reflected or transmitted diffusely (scattered).

diffusely. The relative amount of light that is backscattered is called the diffuse reflectance or the non-specular reflectance, R_{dif}, and is calculated according to equation 1.18.

$$R_{dif} = \frac{P_{bs}}{P_0} \tag{1.18}$$

As with reflection, most of the transmitted light continues on a trajectory governed 1.17, but a small amount is scattered by the surface non-uniformities. Similar to diffuse reflectance for backscattered light, a relative amount of forward scattered light is called the diffuse transmittance or the non-specular transmittance, T_{dif}, and is calculated according to equation 1.19.

$$T_{dif} = \frac{P_{fs}}{P_0} \tag{1.19}$$

The specular reflectance R_{sp} and specular transmittance T_{sp} are defined similarly.

$$R_{sp} = \frac{P_R}{P_0} \tag{1.20}$$

$$T_{sp} = \frac{P_T}{P_0} \tag{1.21}$$

In most cases the scattered light is no longer useful, and as such constitutes a loss in power to the main beam. The scatter loss coefficients TS_f (forward scatter) and TS_b (backscatter) are used to represent the total amount of scatter loss from a sample which may be a single interface, a single layer coating or a multi-layer. In the case of a single interface, TS_f and TS_b are equivalent to T_{dif} and R_{dif}. In the case of thin films and multi-layers the relationship is not as simple. The diffuse reflectance and transmittance of each layer as well as the electric fields at each layer must be considered. The total scatter loss, TS, is simply the sum of TS_f and TS_b.

$$\mathrm{TS} = \mathrm{TS}_f + \mathrm{TS}_b \tag{1.22}$$

In addition to the light lost to scatter in a thin film, light is also lost to absorption. The amount of light a sample absorbs is called the absorbance, α_{abs}.

$$\alpha_{abs} = \frac{P_{abs}}{P_0} \tag{1.23}$$

Where P_{abs} is the total power absorbed by the sample. The total power lost in a sample is the sum of the scatter loss and the absorbance:

$$P_{lost} = P_{abs} + P_{bs} + P_{fs} = P_0 \left[\alpha_{abs} + \mathrm{TS}_b + \mathrm{TS}_f\right] = P_0 \left[\alpha_{abs} + \mathrm{TS}\right] \tag{1.24}$$

Depending on the application, the definition of 'lost light' might include either specularly reflected or transmitted light. For a high reflector the total power lost can be described according to equation 1.25. For an anti-reflective coating the total power lost can be calculated according to equation 1.26:

$$P_{lost(HR)} = P_o \left[\alpha_{abs} + \mathrm{TS} + T_{Sp}\right] \tag{1.25}$$

$$P_{lost(AR)} = P_o \left[\alpha_{abs} + \mathrm{TS} + R_{Sp}\right] \tag{1.26}$$

The term in the brackets is the total loss of the sample. Because energy must be conserved, the power of the output light must equal that of the input light.

The ratio of R_{dif} to T_{dif} is related to the ratio of R_{Sp} to T_{Sp}.ie, in a sample that has no transmission, there is also no transmitted scatter. This becomes a bit more complicated when attempting to quantify samples with R less than 1. As an example, consider two samples. Sample 1 is transparent and has $R_{Sp} = 0.04$. Sample 2 has the exact same surface texture but is metalic so that $R_{Sp} = 0.99$. TS_b measured for sample 2 is significantly larger than the loss measured for sample 1. Clearly, the reflectance of the sample must be accounted for when discussing scatter loss and comparing samples with significantly different reflectance. Total integrated scatter (TIS) does this.

$$\mathrm{TIS}_b = \frac{R_{dif}}{R_{Sp} + R_{dif}} \approx \frac{\mathrm{TS}_b}{R_{sp}} \tag{1.27}$$

$$\mathrm{TIS}_f = \frac{T_{dif}}{T_{Sp} + T_{dif}} \approx \frac{\mathrm{TS}_f}{T_{sp}} \tag{1.28}$$

In the case of a high reflector, T_{dif} and T_{Sp} are very small compared with R_{dif} and R_{Sp} so, $R_{sp} + R_{dif}$ approaches 1 and TIS_b approaches TS_b. Thus, TIS is a particularly useful parameter for low reflection coatings or for comparing coatings with different reflectance.

1.5.2 Scatter measurement

Scattered light can be measured two fundamentally different ways: Total scatter (TS) measurements and angle resolved scatter measurements (ARS). TS measurement are typically simple instrumentally and give the most directly useful information (total light lost to scatter), but TS measurements lack the depth of information that ARS measurements can give about the distribution of spatial frequencies. Typically an integrating sphere is used to collect the hemispherical scatter from the sample. The integrating sphere method is discussed thoroughly in section 2.2.1.

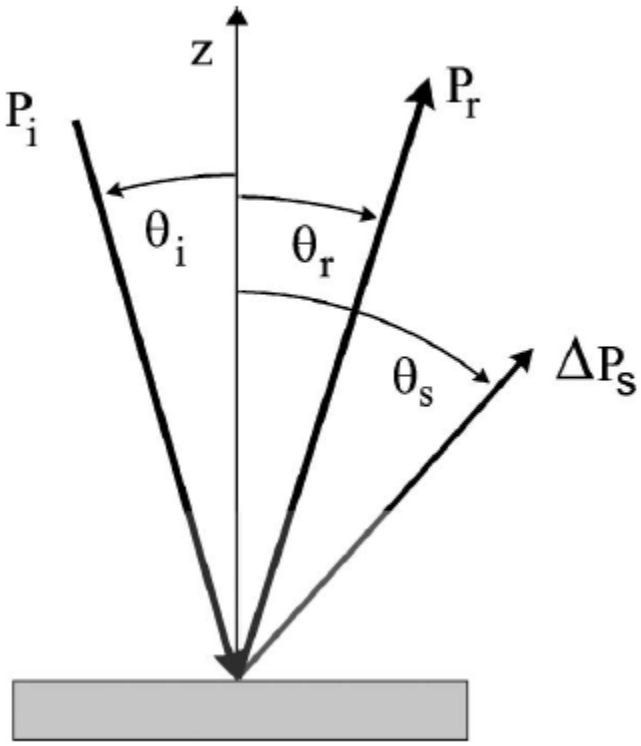

Figure 1.16: Diagram of the geometry in ARS measurements[51]

In ARS measurements, a high sensitivity photo-detector sits at the end of a long rotating arm attached to a goniometer. The detector occupies a known solid angle of the sphere made by the radius of the goniometer arm. The goniometer is rotated to collect the scattered power as a function of angle. The detector does not have to

rotate in both the azimuthal and angular directions because most optical samples are assumed to have azimuthal symmetry. The measured ARS is:

$$ARS = \frac{\Delta P_s / \Delta \Omega_s}{P_o} \tag{1.29}$$

which can be integrated to get the total scatter (TS)[51]:

$$\mathrm{TS}_b = \frac{P_s}{P_0} = 2\pi \int_{2^\circ}^{85^\circ} ARS(\theta_s) \sin\theta_s d\theta_s \tag{1.30}$$

$$\mathrm{TS}_f = \frac{P_s}{P_0} = 2\pi \int_{-2^\circ}^{-85^\circ} ARS(\theta_s) \sin\theta_s d\theta_s \tag{1.31}$$

$$\mathrm{TS} = 2\pi \left[\int_{2^\circ}^{85^\circ} ARS(\theta_s) \sin\theta_s d\theta_s + \int_{-2^\circ}^{-85^\circ} ARS(\theta_s) \sin\theta_s d\theta_s \right] \tag{1.32}$$

where P_s is the total power of the scattered light and P_0 is the power of the beam impinging on the sample. The limits of 2° and 85° specified in ISO 13696 which governs scatter measurements[14].

1.6 Relationship between scatter loss and surface roughness

This section discusses quantitatively the connection between surface roughness and scatter loss, starting with theory for scattering of light from small features and ending with theory relating specifically to smooth surfaces.

1.6.1 General theory of light scattering

When considering general theories of light scattering by objects, there are three regimes to consider which are related to size of the scattering object. A scattering

parameter (x) is used to differentiate these regimes.

$$x = \frac{2\pi r}{\lambda} \tag{1.33}$$

where r is the critical dimension of the scatterer and λ is the wavelength of illumination. If the scatterer is significantly smaller than the wavelength of the light($r << \lambda$), the light scatters by Rayleigh scattering, which has a $1/\lambda^4$ dependence. For scatterers that are about the same size as the wavelength of light, the problem is far more difficult. Solutions to Maxwell's equations are not as easily attained, and an analytical solution called Mie theory was developed by Gustav Mie[45]. Mie theory can fairly accurately predict scattering magnitudes and angular scattering distributions, but requires a fairly complete knowledge of the geometry and size distributions of the scatterer, which makes its application to thin films more difficult.

In the case of very small particles ($x << 1$) the intensity per unit area scattered by the particle is[10]:

$$I(R,\theta) = I_0 \frac{8\pi^4 N\alpha^2}{\lambda^4 R^2}\left(1+\cos^2\theta\right) \tag{1.34}$$

where N is the number of particles, α is the polarizability of the particle, λ is the wavelength of the incident radiation, R is the distance from the center of the particle, and θ is the angle of the scattered light. The most notable aspect of this solution is the $1/\lambda^4$ dependence which means that scatter from small features and particles increases significantly at lower wavelength.

For particles that are approximately the wavelength of light ($x \approx 1$) the analytical solutions come out of Mie theory. A general solution to the problem of light scattering from spheres of arbitrary size was achieved by Gustav Mie in 1908 [19]. Starting from Maxwell's equations, Mie developed a solution that could calculate electric fields at any point inside and outside the sphere [19]. The general solution achieved by Mie is

shown in equations 1.35, and 1.36.

$$E(\theta,\varphi) = -\frac{i}{kr}e^{-ikr+iwt}\cos(\varphi)S_2(\theta) \tag{1.35}$$

$$H(\theta,\varphi) = -\frac{i}{kr}e^{-ikr+iwt}\sin(\varphi)S_1(\theta) \tag{1.36}$$

where S_1 and S_2 are scattering factors which are calculated from the modified spherical Bessel functions π and τ[19].

$$S_1(\theta) = \sum_{n=1}^{\infty}\frac{2n+1}{n(n+1)}\left[a_n\pi_n(\cos\theta) + b_n\tau_n(\cos\theta)\right] \tag{1.37}$$

$$S_2(\theta) = \sum_{n=1}^{\infty}\frac{2n+1}{n(n+1)}\left[b_n\pi_n(\cos\theta) + a_n\tau_n(\cos\theta)\right] \tag{1.38}$$

In more practical terms, this solution leads to scattering and extinction efficiencies (Q_s and Q_e) that are defined by:

$$Q_s = \frac{2}{x^2}\sum_{n=1}^{\infty}(2n+1)\,\Re\left(|a_n|^2 + |b_n|^2\right) \tag{1.39}$$

where a_n and b_n are the Mie scattering coefficients, which are a function of the size parameter (x) and the indices of refraction of the scatterer and the material in which the scatter is suspended[2]. The infinite sums in equations 1.39 and 1.39 cannot be calculated exactly, so the summation must be terminated at a point where the summation closely approximates the exact answer. As the size of the particle (and hence the size parameter x) increases, the number of terms that must be summed increases as well. For large particles, Q_s and Q_e cease to be accurate due to rounding errors within the sum, so a different method such as geometrical optics (figure 1.17) must be pursued[2].

If the scattering object is much larger than the wavelength of the incident light,

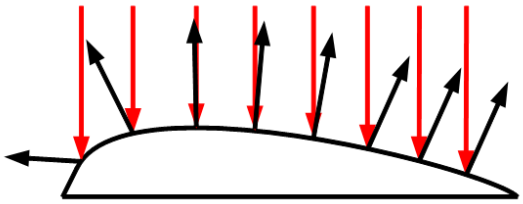

Figure 1.17: An illustration of geometric scattering. Light is scattered according to equations 1.17 and 1.16

the light interacts simultaneously with many atoms which act together and cause the light to scatter in the "forward" direction much like the effect observed in the stacks of two or more layers[45]. In this case, the light follows the rules of refraction and reflection and scatter geometrically. This means that light scattering can be predicted based on the geometry of the scatterer (see figure 1.17).

1.6.2 Scattering from smooth surfaces

In the 1950s, Davies developed a theory to relate the roughness of a surface to the scattering of electromagnetic waves[18]. The theory was then further developed by Porteous and Bennett in 1961 [13] to achieve the relationship:

$$TS = R\left(\frac{4\pi\sigma_{rms}}{\lambda}\right)^2 \tag{1.40}$$

This relationship has validity only for very smooth surfaces, ($\sigma_{rms} \ll \lambda$). The integration limits used to calculate the RMS roughness must chosen carefully - not all roughness features affect scatter the same at all wavelengths. The inverse relationship of TS with the λ^2 is important to note - the same surface scatters light at short wavelengths significantly more than longer wavelengths[51].

ARS can also be related to the film roughness and the interfaces in a multilayer through the use of the PSD functions of each of the interfaces.

$$ARS(\Theta_s) = \frac{1}{\lambda^2} \sum_{i=1}^{N+1} \sum_{j=1}^{N+1} C_i C_j PSD_{ij}(f) \tag{1.41}$$

where N is the number of layers in the multi-layer and C_j and C_i are optical factors that are derived from an ideal multilayer that has no interface roughness. PSD_{ij} is the interface cross correlation PSDs for surfaces i and j. There are typically many bilayers in an multilayer mirror, so actually modelling this can be a difficult task. This process can be simplified by assuming most of the interface roughness to be repetitive from layer to layer, but still leads to less than reliable models. In addition, since much of the micro-roughness does not correlate from layer to layer it is even more difficult to successfully use equation to evaluate the interface roughness[51].

The PSD can be useful in determining how light scatters from a coating. Features with spatial frequencies much higher than the incident light (shorter spatial wavelengths) do not cause significant scatter loss, but rather act as an intermediate medium that increases the transmittance of the top layers of the coatings and thereby decreasing the reflectance. Features with spatial frequencies lower than the frequency of the incident radiation do contribute to significant scatter loss. Spatial frequencies much lower than the frequency of the incident radiation scatter light close to the specular direction which is called near angle scatter[50]. PSDs for substrates tend to be higher at lower spatial frequencies than oxide coatings. This means that substrate roughness generally creates near angle scatter and coating roughness generally creates more hemispherical scatter[14].

AFMs are very useful tools for measuring surface roughness of optical coatings because they can measure spatial frequencies from around 0.05 to 50 μm^{-1} which cover a large region of the spatial frequencies of interest for light scattering. Spatial frequencies below 0.05 μm^{-1} can also cause scatter, so white light interferometers (WLI) can be used to extend the PSD lower. Figure 1.18 shows the spatial frequencies that AFM and WLI devices can measure as well as the spatial frequencies that

contribute to scattering for light of three different wavelengths. The specifics of both AFM and WLI techniques are discussed further in Chapter 2.

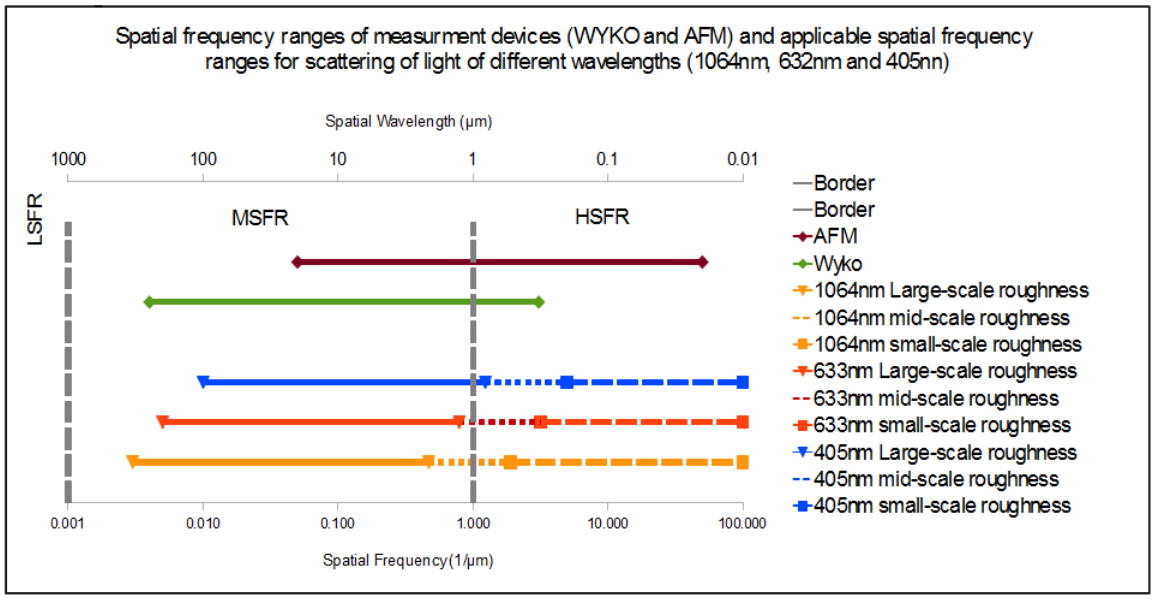

Figure 1.18: The spatial frequency range sampled by two different surface measurement methods and the applicable ranges for light scattering at three wavelengths of light. The solid bar is the range of spatial frequencies that contribute to near angle scatter. The ultra fine dashed bar indicates the region that contributes to hemispherical scattering and the large dashed bar indicates the region of spatial frequencies that does not contribute to scattering but does affect the transmittance of the interface[50].

Chapter 2

Experimental Techniques

This chapter discusses the experimental techniques used in this work. Dual ion beam sputtering, the process by which oxide thin film coatings are deposited is discussed first in section 2.1. Several different techniques are used to characterize the samples after they are deposited. Each of these techniques are discussed individually, including basic theory of operation as well as the specific experimental setup.

2.1 Dual ion beam sputtering system

The oxide coatings characterized in this work were deposited onto optical substrates using a dual ion beam sputtering (DIBS) system. This section discusses the general layout and operation of the system as well as the specific deposition parameters that are changed to create the sample sets used in this work.

2.1.1 General layout

A diagram of the system is shown in figure 2.1. Sputtering is the process by which atoms are removed from a solid state target by energetic ions or atoms[49]. The sputtering ions (in this case Ar^+) deliver enough energy to the target atoms that

they are removed from the target into a vapour directed towards the substrates. In this DIBS system, an Ar^+ ion beam is created by an RF ion source. Each energetic ion removes a number of target atoms which are ejected from the target with lower energy and some distribution of directions which is centered on the sample holder.

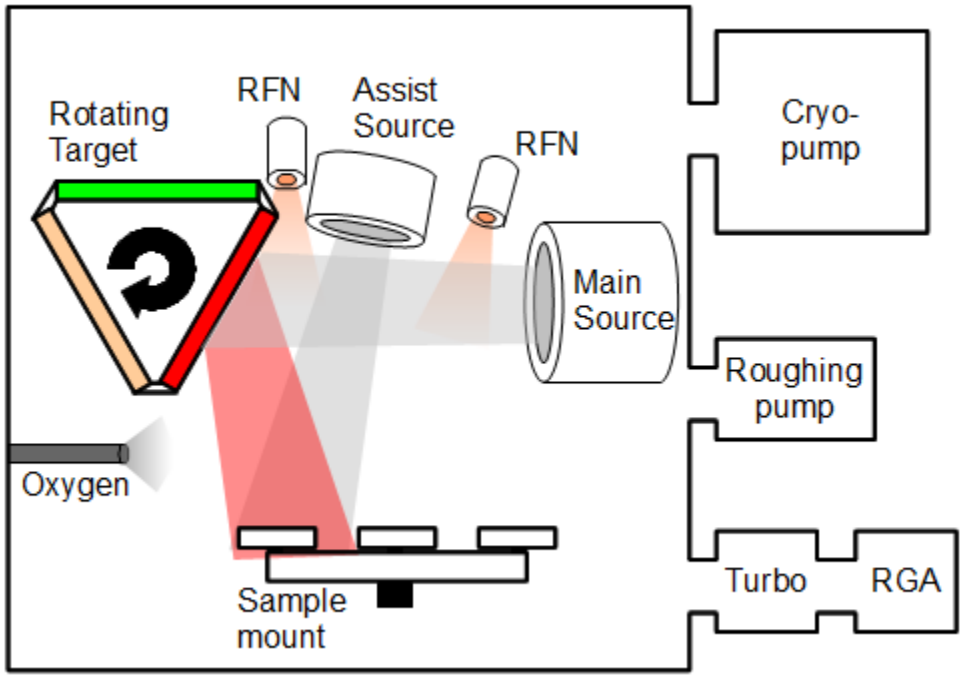

Figure 2.1: Diagram of the DIBS system used to deposit oxide coatings.

The plume of target atoms then impact upon and condense on all the surfaces of the chamber and on the substrates. The flux of target atoms or molecules is not uniform or homogeneous so neither is the growth rate. To achieve uniformity, the samples must be spun. In the system used in this work, uniformity is accomplished by a planetary rotating system made up of four "planets" attached to a central "sun". The "planets" and the "sun" rotate independently as shown in figure 2.2. The goal of the planetary system is to create quasi-random motion. Though the "sun" rotates at 0.4 rps, the actual period of the planetary (such that the sample returns to the exact point it started) is several minutes. Samples are cleaned and loaded into sample

holders in a class 1000 clean room. Substrates were cleaned using ultrapure acetone and methanol before being loaded into sample holders[52].

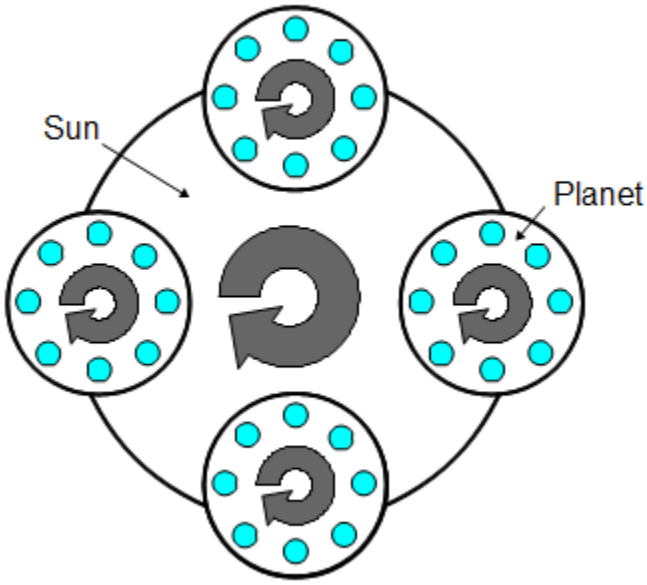

Figure 2.2: Planetary sample mount. The "sun" and "planets" rotate independently to ensure uniformity.

A second ion beam is directed at the sample. This "assist" beam is used to increase packing density of the growing films. To maintain neutral space charge, two radio frequency neutralisers (RFNs) are used to inject low energy electrons into the chamber. The electrons from the RFNs do not directly neutralize the ions in the Ar^+ beam, but rather maintain a neutral space charge in the chamber[52].

The target can be either a metal target or an oxide. The target mount is water cooled and rotates to allow for the use of three different targets without venting of the system. During deposition, the target is set to oscillate to allow uniform sputtering of the target.

To minimize defects and allow sputtered atoms to reach the substrate without collisions, the deposition process must be conducted under vacuum. The vacuum system

consists of a dry mechanical roughing pump and a cryogenic pump. High vacuum is achieved by a cryogenic vacuum pump. Typical base pressures are around 10^{-5} Pa. Gasses are flowed into the chamber during deposition for a couple of reasons. Argon gas is flowed through the RFNs and the ion sources. For reactive sputtering from metal targets, oxygen is flowed into the chamber. At steady state conditions during deposition, the chamber pressure increases to around 10^{-2} Pa. Gas flow controllers are used to monitor and control the flow of argon and oxygen into the chamber. Gaseous partial pressure was measured with a quadrupole residual gas analyser (RGA). A computer controls all deposition parameters, and records all pertinent information for the duration of the coating process.

The gridded ion sources used in this system create a mono-energetic ion beam and allows for a number of different parameters to be changed independently which can affect the growth rate, mechanical and optical properties of the final coating. The most important parameters that can be changed are the beam current (I_B) and beam voltage (V_B). Changing V_B changes the kinetic energy of the sputtering ions. V_B can be varied from 600V to 1250V for ion kinetic energies of 600eV to 1250eV. I_B is the charge per unit time that is extracted from the source. Beam current can be varied from 100mA up to 600mA which is 6.2×10^{20} up to 3.7×10^{21} ions per second. Sample growth rate increases with increasing beam voltage and beam current[52].

When the energetic ions impact the surface of a metal or oxide target a number of different processes can occur. The ion may backscatter, implant itself and lose its energy to heat or it may remove target atoms. The process by which atoms are removed from the target by high energy incident particles is called 'sputtering'. The sputtered atoms then form a gas phase, low energy plume of particles and clusters that travel away from the target. The directionality of the sputtered atoms follows a cosine distribution centered around the 'specular'[58].

2.1.2 Test samples

For the work described in this thesis, HfO_2 films were deposited using a hafnium metal target on a variety of substrates while varying a variety of deposition parameters. Figure 2.3 lists all the samples that were created for this experiment.

Set 1 is a set of samples with different beam voltages. The beam voltage was varied from 600 to 1250 V. This set was deposited on several different substrates: polished fused silica with an RMS roughness of 0.6nm, super-polished fused silica with an RMS roughness of 0.1nm, and super polished sapphire with an RMS roughness of 0.1nm. To measure the scatter properties of a completed dielectric interference coating, an output coupler made up of 8 quarter-wave bilayers of SiO_2 and HfO_2 was deposited on the same set of substrates as the first set of samples.The second set of samples was deposited with different thicknesses, ranging from 100nm up to 400nm. These samples were deposited on normal-polished fused silica with an RMS roughness of 0.6nm and on silicon wafers.

	Beam Voltage (V)	Thickness (nm)	Substrates
Set 1 (vs. V_B)			
	600	150	A,B,C
	800	150	A,B,C
	1000	150	A,B,C
	1250	150	A,B,C
Set 2 (vs. thickness)			
	600	100	C
	600	150	C
	600	200	C
	600	400	C
Output coupler			
	600	[180nm SiO_2, 130nm HfO_2]x8	A,B

Figure 2.3: A compilation of the samples discussed in this work. Key to substrates: **A** = super-polished fused silica (RMS = 0.1nm), **B** = super-polished sapphire (RMS = 0.1nm),**C** = standard polish fused silica (RMS = 0.6nm).

2.2 Film characterization techniques

A variety of experimental techniques are used to characterize the oxide coatings after they are deposited. This section discusses each experimental technique individually. Techniques discussed include a scatterometer used to measure scatter loss at multiple wavelengths, atomic force microscopy and white light interferometry to measure surface roughness, ellipsometry to measure coating thickness and optical constants, spectrophotometry to measure transmission spectra and a twyman-green interferometer to measure stress.

2.2.1 Scatterometer

Scatter loss (TS) measurements at three wavelengths are conducted using a scatterometer. The experimental setup can be seen in figure 2.4.

Three different light sources are used in this scatterometer: a neodynium-doped yttrium aluminum garnet (Nd:YAG) solid state laser operating at 1064nm capable of producing 5 watt output power, a helium neon (HeNe) laser operating at 632.8nm capable of producing 5mW output power, and a diode-pumped solid state (DPSS) crystal laser operating at 405nm capable of producing 10mW output power. The output power of the YAG is reduced to around 300mW to match the dynamic range of the detector and the system.

The optical system is laid out in such a way that measurements can be made for reflected scatter as well as transmitted scatter. Several mirrors are used to direct the probing laser beam to the integrating sphere. Switching from reflected to transmitted scatter measurements is accomplished by a flip mirror. A chopper was placed early in the optical system to modulate the signal going to the integrating sphere at a specific frequency so lock-in detection could be used. After the chopper, a partially reflecting optic was used to "pick-off" a constant amount of light from the beam that was then

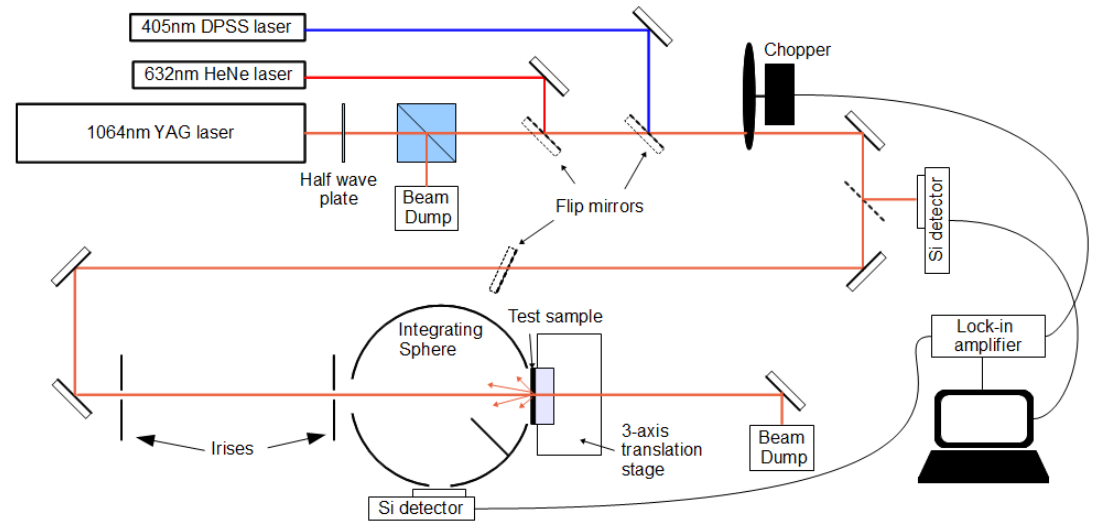

(a)

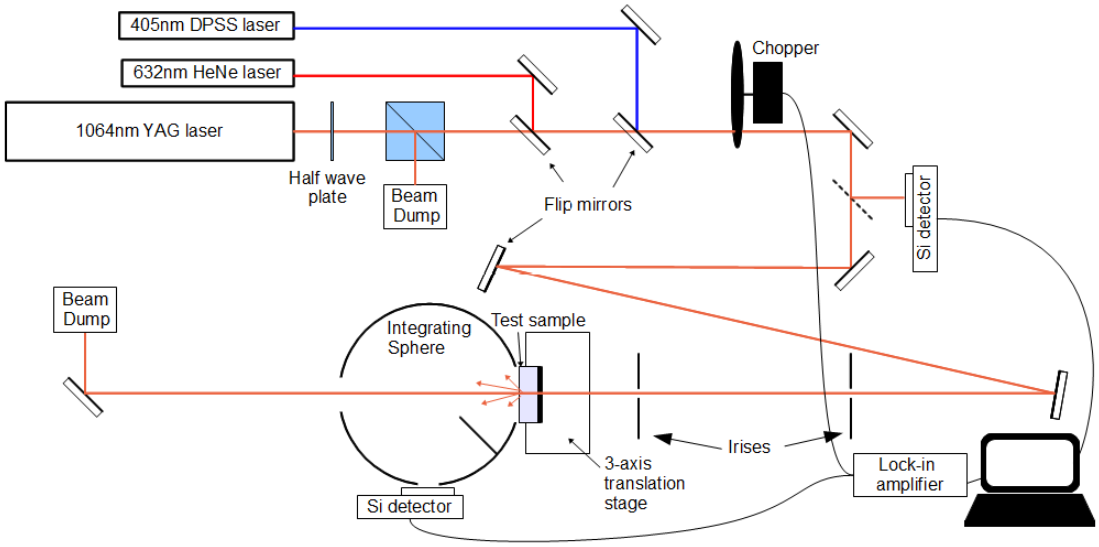

(b)

Figure 2.4: Diagram of the measurements of (a) scatter loss due to backscatter (TS_b) and (b) scatter loss due to forward scatter (TS_f). Switching from one configuration to the other is accomplished by a flip mirror.

monitored using a biased silicon detector. This is called the "pick-off" detector and it is used to account for variations in the output power of the lasers.

A four inch diameter integrating sphere is used to collect light scattered from the sample. The integrating sphere has three ports all with knife edges. Port one is where the beam enters for reflected scattering measurements. Port two is the sample port. Port three is the detector port. There is a baffle between the sample port and the detector port which prevents light from travelling directly to the sample to the detector. Ports one and two have 0.5" diameters. Port 3 has a 1" diameter. Integrating spheres are be discussed more thoroughly in section 2.2.1.

The detector on the integrating sphere is an adjustable gain amplified silicon detector. The detector was chosen based on the wavelength range, noise requirements and varying power of the different light sources used. The responsivity curve of the detector (shown in figure 2.5) peaks between 800 and 1050nm, but has acceptable responsivity at 1064nm and 632nm (0.3 A/W). At 405nm, the silicon detector is less responsive (0.1 A/W), but has sufficient responsivity for the purpose of scatter measurement. The output power of the three sources is quite different (5mW for the HeNe, 10mW for the DPSS, 300mW YAG), so a variable gain detector was used to match the dynamic range of the detector to the requirements of the system. Each gain setting has a different noise level due to the amplification circuitry so background noise measurements must be repeated whenever the detector gain is changed.

The signal from the detector is sent to a lock-in amplifier. The lock-in amplifier filters out any signal that is not at the chopped frequency (approximately 1.5 kHz). The intrinsic random noise of the lock-in amplifier is around 1-5nV (intrinsic noise is measured by disconnecting the detector from the amplifier). The maximum voltage the lock-in can tolerate is 1V, giving the lock-in a dynamic range of approximately 10^9, which is more than sufficient for this measurement. The limiting factor in small signal detection and background noise turns out to be the optical system and well as

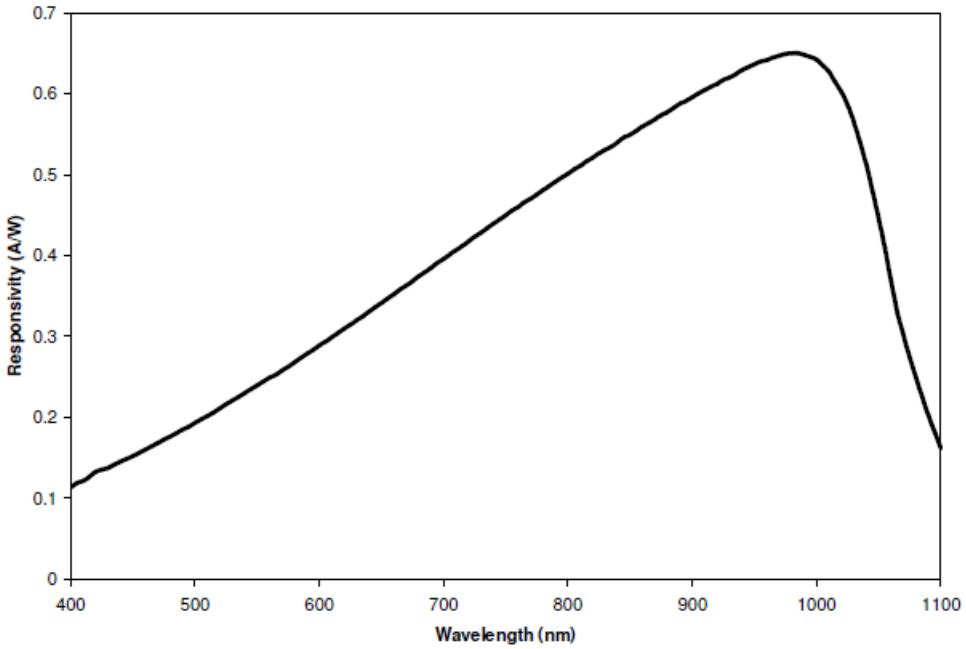

Figure 2.5: Spectral responsivity for the silicon detector used in this experiment. This detector was used for alll three wavelengths, and the same model of detector was used for both measuring the power in the integrating sphere and for measuring the power of the incident light. The responsivity falls rapidly above 1050nm because the photon energy is less than that of the silicon bandgap (1.1eV). The responsivity falls at lower wavelengths due to decreased penetration depth. As the penetration depth decreases, less of the radiation is absorbed in the depletion region of the p-n junction where optical power most efficiently couples into electric power. [17]

electronic noise from the detector when higher gain settings are used.

The same optical system is used to deliver illumination from each laser to the integrating sphere. Figure 2.4 (a) shows the configuration for measuring scatter loss due to backscatter (TS_b). In this configuration, incident light enters through port one. The light impinges on the sample at normal incidence. Some of the light is reflected specularly and some is scattered. The specularly reflected light exits the integrating sphere through port one and is dumped. The scattered light is collected by the integrating sphere. After a few bounces, the integrating sphere becomes uniformly illuminated. The detector measures the amount of the illumination.

By moving a flip-mirror into the beam line, the same setup can be used to measure scatter loss due to forward scatter (TS_f). This setup is shown in figure 2.4 (b). The incident beam passes through the sample before entering the integrating sphere through port 2. The specularly transmitted light continues straight through the sphere and exits through port 1. The transmitted scattered light is collected by the integrating sphere and then measured by the detector in port 3.

Near angle scattered light from early in the optical system can introduce significant background noise to the measurement. To reduce the amount of unwanted scattered light that reaches the integrating sphere, two variable diameter irises were placed directly upstream of the integrating sphere. The irises were mounted to xy translation stages to allow for more precise alignment. The iris alignment is critical to reducing the background noise of the system. The irises are aligned such that stray light and scattered light from earlier in the optical system are blocked without clipping any of the main beam. Any clipping of the parts of the beam that have significant power results in significant increase in diffracted light which can enter the integrating sphere and included in the detector signal. Diffracted light due to iris misalignment or irises that are set too small can easily lead to background noise that is orders of magnitude greater than the scatter signal from the sample. Conversely, if the irises are allowed

to be too far open, scattered light from earlier in the system can enter the integrating sphere with a trajectory that would allow it to be integrated into the main detector signal and thereby increase the background noise level.

Other sources of background noise include light scattering from earlier in the optical system and light reflecting back towards the integrating sphere after passing through the sample. Each of these sources of noise was mitigated to the point that it was not a significant portion of the measured signal from actual samples. Total background noise at 1064nm, 633nm and 405nm is 0.2ppm, 0.5ppm and 3.5ppm respectively.

Integrating sphere

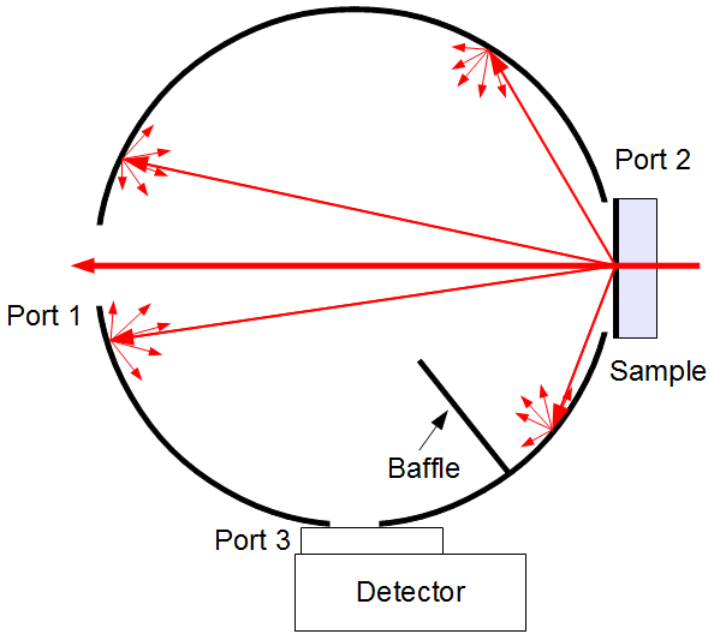

Figure 2.6: A diagram of an integrating sphere illustrating how after only a few bounces the sphere is uniformly illuminated. A baffle prevents any direct illumination of the detector without at least one reflection off the sphere wall.

Integrating spheres are devices to measure hemispherical or spherical light com-

ing from a source or off of a surface and are commonly used to measure scatter loss, reflectivity and color[34]. The hollowed inside of the sphere is coated with a carefully selected rough material that has very high reflectivity over a large range of wavelengths. The coating material is rough enough that it has nearly uniform hemispherical reflectance. After only a few reflections, the sphere is nearly uniformly illuminated as illustrated in figure 2.6. Because it is uniform throughout the sphere, the power per unit area at the walls (L_s) can be calculated from the input light flux P_0, the surface area of the sphere A_S, the reflectance of the wall ρ_w, and the port area f[34]:

$$L_s = \frac{P_0}{\pi A_s} \frac{\rho_w}{1 - \rho_w(1 - f)} \tag{2.1}$$

A detector placed at one of the ports measures this uniform radiation. The voltage measured by the detector can be related directly to the amount of light collected by the sphere using the spectral responsivity of the detector ($\Re(\lambda)$), the resistance of the load resistor (R_{load}), and the surface area of the detector (A_{det}).

$$V_{det} = \Re(\lambda) L_s A_{det} R_{load} = \frac{\Re(\lambda) A_{det} R_{load} P}{\pi A_s} \frac{\rho_w}{1 - \rho_w(1 - f)} \tag{2.2}$$

Since A_s is related to the square of the radius, smaller spheres have increased signal throughput. There are engineering limitation that prevent the spheres from getting too small. As the integrating sphere gets smaller and the port sizes remain constant, the port fraction increases. This in turn lowers the power per unit area within the sphere and the signal from the detector. A four inch diameter sphere is used for this experiment because it is the smallest size available for a sphere with the port configuration required.

Measurement procedure

From equation 1.30, $TS = \frac{P_s}{P_0}$. P_s can be calculated directly using equation 2.2, by solving for P. P_0 must be measured as well to get TS. This is accomplished using a highly reflecting diffuse calibration sample made of the same material that coats the inside of the integrating sphere. This sample has near 100% reflectance, nearly all of which is collected by the integrating sphere. The optical power collected by the integrating sphere can then be calculated using equation 2.2. However, when P_s is divided by P_0, everything but the recorded voltages (V_s and V_0) drop out.

$$TS = \frac{P_s}{P_0} = \frac{V_s \frac{\pi A_s (1-\rho_w(1-f))}{A_{det} R_{load}}}{V_0 \frac{\pi A_s (1-\rho_w(1-f))}{A_{det} R_{load}}} = \frac{V_s}{V_0} \tag{2.3}$$

So long as none of the other variables are changed between measurements (detector surface area, port fraction, integrating sphere surface area), TS can be calculated by simply dividing the voltages. Background noise must be accounted for in the measurement process as well. To accomplish this, a measurement is made with no sample in place. This voltage (V_{bg}) is subtracted directly from the measured scatter signal ($V_{measured}$) to get V_s.

$$V_s = V_{measured} - V_{bg} \tag{2.4}$$

To limit the effect of random noise, each measurement was integrated over a 30 second period. A minimum of five points were measured for each sample. Fluctuations in laser power were very small (5% drift for 1064nm and 1% drift for 405nm and 633nm), but were corrected for using the signal from the "pick-off" detector. A measurement of V_0 is made periodically throughout the measurement process to make sure it does not change significantly. A measurement of V_{bg} is made at each sample position before the testing commences and then again periodically to ensure it does not change. Two highly reflecting calibration samples with different roughness's are

used to check for day to day changes in the measurements.

2.2.2 Atomic force microscopy

Atomic force microscopy is a technique by which one and two dimensional profiles of the surface topography of optically smooth surfaces can be recorded. An array of surface heights can be recorded and analysed[39]. A diagram of the AFM used in this work is shown in figure 2.7.

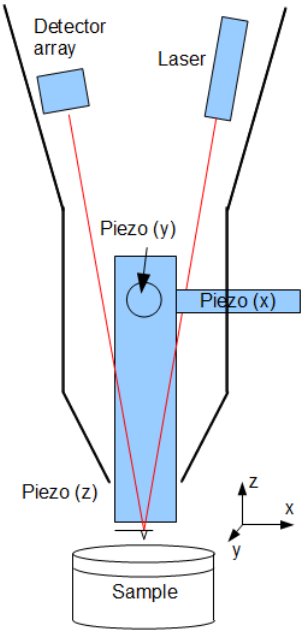

Figure 2.7: A diagram of the atomic force microscope used for this work.

An ultra-sharp tip (between 1 and 20 nm radius of curvature) is affixed to a cantilever on the end of a silicon chip. The cantilever has a resonant frequency given by its length and thickness, which is generally in the hundreds of kHz. A diagram of the tip and an SEM image of a tip are shown in figure 2.8. The tip is driven at its resonant frequency by a piezoelectric actuator. A laser is focused on the back of the cantilever which is coated with aluminum to increase reflectivity. The reflected laser light is recorded by a detector array. The distribution of the light across the detector

array changes along with the deflection of the vibrating tip. By monitoring the signal from the detector, the resonant frequency of the tip can be measured continuously. [43]

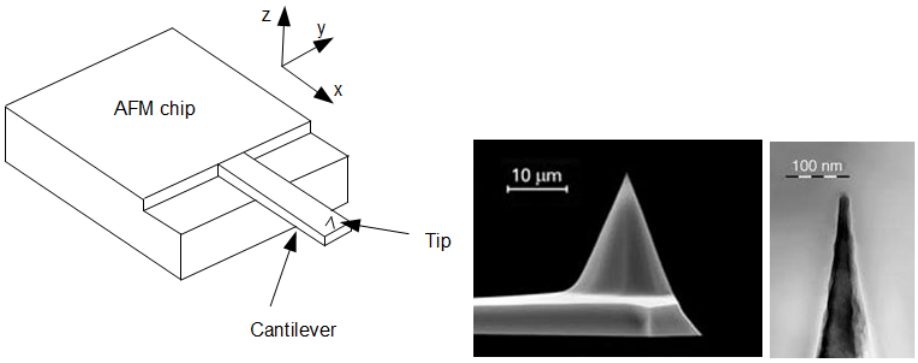

Figure 2.8: (a) A diagram of an AFM chip. (b) Scanning electron microscope image of the AFM tip on the end of the cantilever. (c) a close up scanning electron microscope image showing the sharpness of the very end of the tip.[5]

The AFM head is lowered towards the sample until it is close enough that the sharp tip can interact with the sample through Van der Waals forces[39]. This additional force on the tip changes the resonant frequency of the cantilever which is recorded by the detector array. The tip is raster scanned across the sample by two orthogonal piezoelectric actuators (oriented along the x and y axes). As the tip is scanned, the vertical (z-axis) piezoelectric actuator is controlled through a feedback loop to keep the tip at approximately the same height off of the sample at each x/y point. This is achieved by maintaining a constant resonant frequency. The displacement of the z-piezo is recorded at each point to achieve an array of surface heights[43].

The force of the tip on the sample in AFM surface measurements is much lower than in other surface profilometry techniques (nN in AFM vs 10s of μN in surface profilometry) [43]. Lower force means that surface damage is minimized. However, samples with sharp features such as large particles or large ridges can damage tips if used in constant contact (also called contact mode). Instead, an intermittent contact

technique is used, called tapping mode, in which the tip vibrates and only contacts the sample for a small portion of its duty cycle. This reduces the amount of lateral load the tip experiences. Tips last much longer in tapping mode and less damage is done to the surface.

The x and y piezo motors cause the scanning head to pivot rather than translate. This introduces a bowing effect on the sample. There is also usually a difference in tilt between the sample and the scanning head, which leads to tilt in the recorded scan. This bow and tilt can be corrected for after the scan through the use of flattening algorithms built into the software. However, this manipulation inherently makes measuring of spatial frequency roughness near the low end of the spatial frequency range less accurate (ie, flattening algorithms can remove roughness by confusing with bow or tilt). A diagram of the bow/tilt problems is shown in figure 2.9.

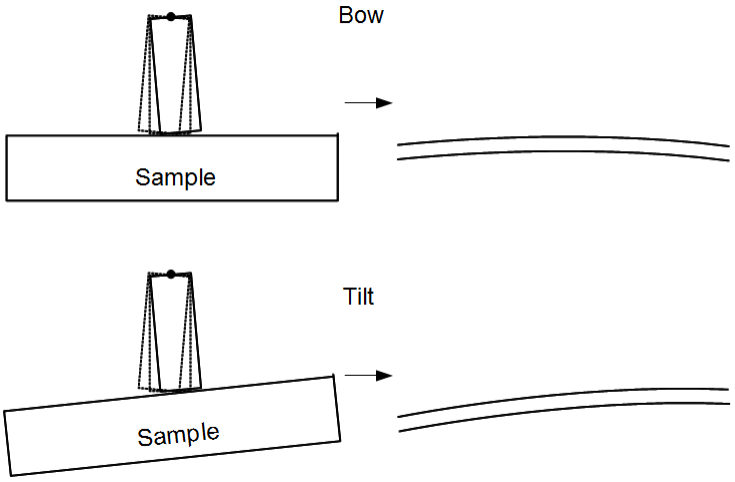

Figure 2.9: A diagram describing the problem of bow and tilt in the AFM used in this work.

Surface scans were conducted with a Novascan SPM-3D atomic force microscope (AFM) in tapping mode. A micromasch NSC-15 tip was used for all scans. The tip has a resonant frequency of 325kHz and a 10nm radius of curvature tip. For each sample, square 15um scans were conducted at a minimum of three spots on the

sample. The scan resolution was 500 pixels/line. Bow and tilt were removed using algorithms in the Novascan software, and the same corrections were used on every scan. Each scan is outputted as raw data and analysed in a separate Matlab program. The Matlab program calculates the RMS roughness, skewness, pit-area of the scan, and produces height histogram, 3-d and 2-d plots and a PSD. RMS roughness is defined in equation 1.13 from chapter one. Pit area is defined as the percent of the area in which the surface heights are more than four standard deviations below the average height.

The scan sizes of $15\mu m$ and $40\mu m$ were chosen for the following reasons. $40\mu m$ is the largest scan that can be made with the AFM can achieve. Lower spatial frequencies are important for scatter prediction, especially at longer wavelengths. The larger scan size allows the PSD to be extended to lower spatial frequencies. The $15\mu m$ scan size was chosen because a $15\mu m$ scan at 500 pixel per line resolution means that a pixel is 30nm, which is close to the ideal radius of curvature of the tip. Features smaller than 30nm do not contribute significantly to scattered light in the visible and IR range.

2.2.3 White light interferometry

White light interferometry is an optical technique to determine surface topography of a smooth sample. A white light interferometer (WLI) is an off shoot of the basic Michelson interferometer, which consists of a reference beam and an object beam with some difference in optical path length. The difference between the optical path length of each arm of the interferometer must be less than the coherence length of the light. Modern interferometry tends to use monochromatic light from a laser due to its long coherence length. In white light interferometers, coherent sources with broader spectra are used to allow for better reconstruction due to smaller shifts between fringes and the ability to resolve steps larger than $\lambda/4$[55]. In white light interferometers,

the object beam that reflects off of the sample suffers a phase shift. The magnitude of the phase shift changes with the surface topography[55].

A Veeco WYKO NT2000 white light interferometer was used in this work. A diagram of the device is shown in figure 2.10 (a). A lamp is used to create spectrally broad (white light) illumination which is then filtered by a red bandpass filter. The light after the filter is still spectrally broad compared to a laser (approximately 20nm full width half max). A partially reflecting beam splitter redirects the light towards the sample. An objective lens is used to focus the light to a small spot on the sample. Directly after the objective lens, the light is split into two beams by a Mirau interferometer (shown in figure 2.10 (b))[55].

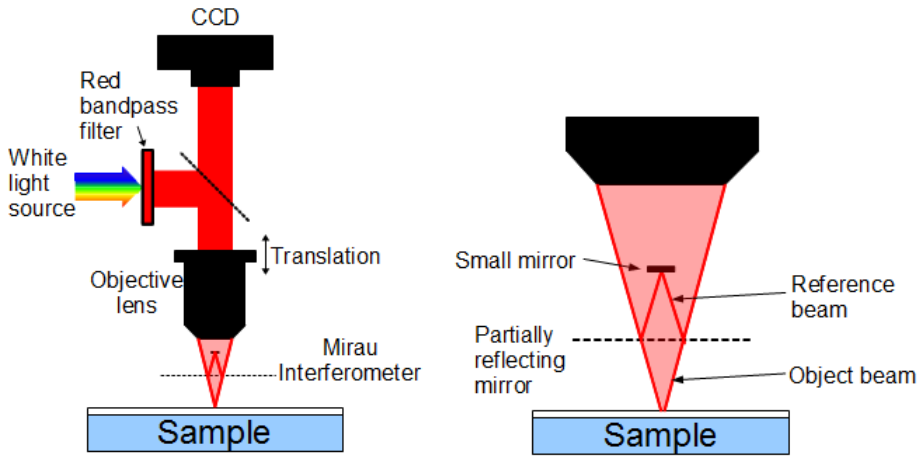

Figure 2.10: (a) A diagram of the WYKO NT2000 white light interferometer used in this work. (b) a diagram of the Mirau interferometer in the objective lens that causes the relative phase shift in the two beams. [55]

The Mirau interferometer consists of a partially reflecting mirror. The light reflected by this mirror becomes the reference beam. A small fully reflecting mirror is placed at the focus of the reflected reference beam light. The reference beam reflects back off of the partially reflecting mirror to recombine with the object beam which has reflected from the sample. The two beams are re-collimated by the objective

lens. The object beam suffers a phase shift with respect to the reference beam that depends on the surface topography of the sample. Since all the surfaces that the reference beam reflect off of are flat, any difference in relative phase between the two beams is a result of irregularities in the sample. The two beams are recombined to form an interferogram which is recorded using a CCD. Small discontinuities in the sample surface cause small changes in the fringes.

In phase shifting interferometry (PSI) mode the objective lens is translated up or down a number of times by a piezo-motor. This change in distance causes an additional phase shift in the object beam which causes the fringes to shift. Several images are recorded with different phase shifts. The surface topography is then reconstructed from the series of images[55]. Surface statistics (RMS roughness, skewness, PSD, etc) can then be calculated from the reconstructed image, in a manner similar to what is described in section 2.2.2.

WLI is a non-contact, non-destructive technique that is complimentary to AFM in surface characterization. Vertical resolution in surface heights down to about 0.2nm can be achieved due to the use of white light which reduces the distance between fringes. However, the combination of CCD pixel size and limitations on the size of the focal spot limit the lateral resolution. The minimum scan size is $120\mu m$. With a scan resolution of 740 pixels per line, the minimum pixel size is about 160nm. By changing the objective lens, the scan can be increased to $500\mu m$. The size can be increased further in some instruments by translating the sample and stitching images together. Figure 1.18 shows a plot comparing WLI and AFM in terms of the size of the spatial frequencies that can be sampled. Though the WLI is not capable of resolving features as small as the AFM, it can measure larger scale roughness (lower spatial frequency) which can contribute more to scattering especially at infrared wavelengths.

WLI also requires less image processing to remove bow and tilt which causes less distortion to the image, especially for low spatial frequencies. Due to the nature

of the instrument, the sample must be aligned very carefully to remove tilt (which is accomplished by centering and minimizing fringes), reducing the amount of tilt removal required in image processing.

2.2.4 Spectroscopic ellipsometry

Spectroscopic ellipsometry is an optical technique that can be used to determine the thickness and complex index of refraction of a thin film. Ellipsometry is a term describing any technique that measures the change in polarization of light upon reflection from a surface. If linearly polarized light is incident upon the surface at an angle, the light reflecting off the sample is elliptically polarized. This effect is caused by the fact that S and P polarized light reflect differently, as seen in the Fresnel reflection coefficients (equations 2.12 through 2.15). Also, P polarized light suffers a phase shift upon reflection whereas S polarized light does not. Light that is linearly polarized, but with some combination of S and P polarized light experiences a change in polarization upon reflection as shown in figure 2.11[25].

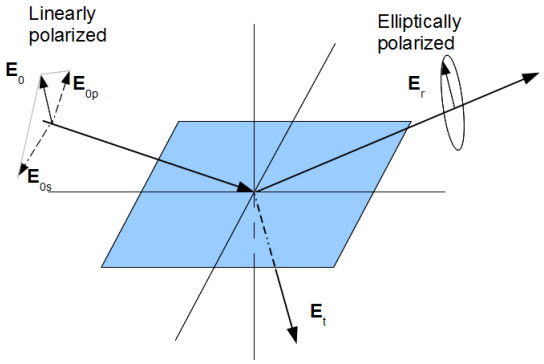

Figure 2.11: Reflected light from an interface. The incident light is linearly polarized, a mix of P and S polarization. The reflected light is elliptically polarized due to a change in relative amplitudes phases of the P and S polarized portions of the light.

By knowing the polarization state of the incident light and the reflected light, the complex Fresnel coefficients (r_s and r_p) can be calculated. Their ratio, ρ, is measured by the ellipsometer. The ratio ρ is related to two "ellipsometric angles" Ψ and Δ [25].

$$\rho = \frac{r_p}{r_s} = \tan\Psi e^{i\Delta} \tag{2.5}$$

Figure 2.12 shows an electromagnetic wave encountering a dielectric interface. E_i represents the electric field component of the incoming wave. E_r and E_t represent the electic field component of the reflected and transmitted electromagnetic waves respectively. Mathematically the coefficients are a combination of an amplitude ($|r|$) and a phase shift ($e^{i\delta}$)[24].

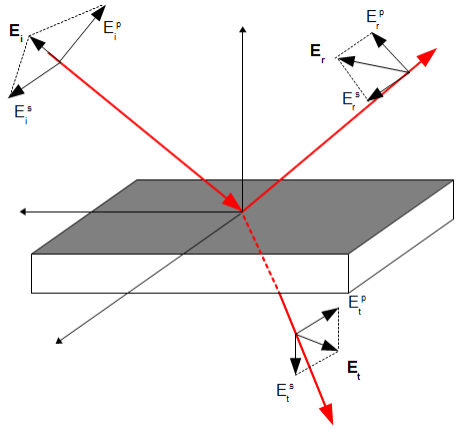

Figure 2.12: Electric field vectors for an electromagnetic wave with linear polarization encountering an interface. From this setup, the reflection and transmission coefficients can be calculated as a function of angle of incidence and the complex indices of refraction of the two meduims. [25]

$$r_p = \frac{E_r^p}{E_i^p} = |r_p|e^{i\delta_p} \tag{2.6}$$

$$r_s = \frac{E_r^s}{E_i^s} = |r_s|e^{i\delta_s} \tag{2.7}$$

The intensity of the reflected light is the square of the electric field amplitude[24], so the intensity of the reflected light is:

$$R_p = |r_p|^2 \tag{2.8}$$

$$R_s = |r_s|^2 \tag{2.9}$$

Ψ can be related to the real part of the complex Fresnel coefficients and Δ can be related to the complex portion.

$$\tan \Psi = \frac{|r_p|}{|r_s|} \tag{2.10}$$

$$\Delta = \delta_p - \delta_s \tag{2.11}$$

The Fresnel reflection and transmission coefficients can then be related to the complex index of refraction $\tilde{n} = n + ik$ by applying the requirement of continuity of the tangential components of the electric and magnetic fields at the interface[36]. The resulting coefficients are:

$$r_p = \frac{\tilde{n}_1 \cos\theta_0 - \tilde{n}_0 \cos\theta_1}{\tilde{n}_0 \cos\theta_0 + \tilde{n}_1 \cos\theta_1} \tag{2.12}$$

$$r_s = \frac{\tilde{n}_0 \cos\theta_0 - \tilde{n}_0 \cos\theta_1}{\tilde{n}_0 \cos\theta_0 + \tilde{n}_1 \cos\theta_1} \tag{2.13}$$

$$t_p = \frac{2\tilde{n}_0 \cos\theta_0}{\tilde{n}_1 \cos\theta_0 + \tilde{n}_0 \cos\theta_1} \tag{2.14}$$

$$t_s = \frac{2\tilde{n}_0 \cos\theta_0}{\tilde{n}_0 \cos\theta_0 + \tilde{n}_1 \cos\theta_1} \tag{2.15}$$

where $\tilde{n}_0$ is the complex index of refraction of the incident medium and $\tilde{n}_1$ is the complex index of refraction of the second medium. This same relationship is true for

all interfaces that the light crosses. So, for a multilayer stack, the Fresnel reflection and transmission coefficients for each layer must be calculated. This process becomes more difficult for samples with many interfaces as light may reflect several times within the stack before exiting (see figure 2.13). The polarization state of the light is different depending on how many reflections the light experiences in the stack. The relative phase of the P and S polarized light change as well due to reflection phase shifts. The amount of polarization change is highest near Brewster's angle where r_p goes to zero. The increased contrast between the S and P reflectances increases the sensitivity of the technique, so ellipsometry is typically done near Brewster's angle[25].

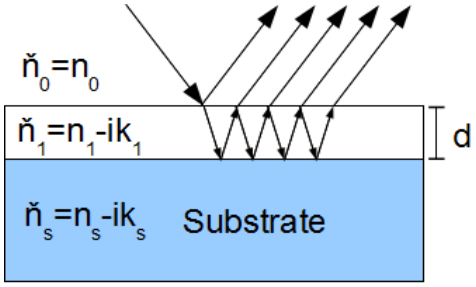

Figure 2.13: Reflected light from a thin film. The light may make many reflections within the layer before reflecting back out of the film. The amplitude and phase of the light measured by the detector is a combination of all of the reflected rays. This effect must be accounted for in the modelling process.

In spectroscopic ellipsometry, Ψ and Δ are measured over a range of wavelengths. This is accomplished by illuminating the sample with broadband light and separating the light by wavelength with a spectrometer after the sample. An example ellipsometric spectrum (Ψ and Δ) is shown in figure 2.14. Ellipsometric spectra can be recorded at multiple angles of incidence to improve the accuracy of the measurement and make modelling easier.

The ellipsometer used in this experiment is a Horiba UVISEL. This ellipsometer uses multiple lamps to provide broadband illumination from 150nm to 2100nm. The light is focused to a small spot on the sample before reflecting and being collected.

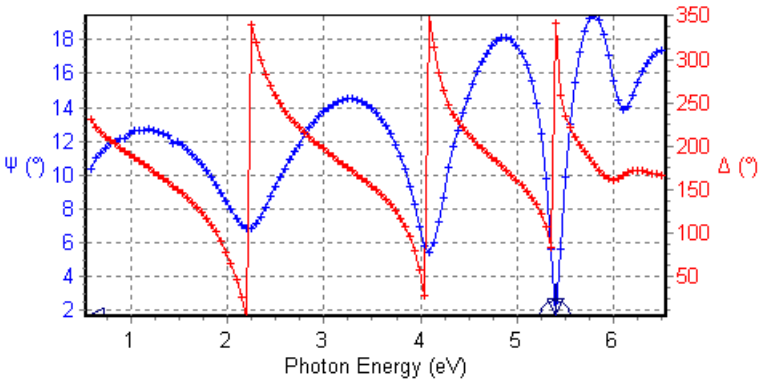

Figure 2.14: Typical Ψ and Δ spectrum for a single layer of hafnium oxide on a fused silica substrate measured at 65° (chosen because it is close to Brewster's angle).

The collected light is then measured using one of two spectrometers. A Horiba iHR320 spectrometer measures infrared light and a Horiba FUV200 spectrometer measures visible and UV light. [4]

In order to turn the collected spectroscopic ellipsometry data into meaningful information about the sample, a model of the sample must be constructed. Modelling was accomplished in this experiment using the Horiba software (DeltaPsi2) that accompanies the ellipsometer[4]. Models must be constructed carefully as arriving at erroneous fits is possible if care is not taken. Typically, some of the details of the sample are known prior to beginning the fitting procedure including the general layer structure, approximate layer thickness and optical constants.

An example of a model used in this experiment for a single layer of HfO_2 on a fused silica substrate is shown in figure 2.15. Different layers can be stacked on top of a substrate. There are two basic types of layers used by the Horiba software. The first is a .ref file which is a series of n and k values that have been calculated from previous ellipsometer measurements. The other main type of layer is a dispersion file (.dsp) which uses a dispersion equation to calculate n and k. The parameters in the dispersion equation can be changed to match the material. The fused silica substrate layer used in figure 2.15 is a .ref file of n and k values which were measured using

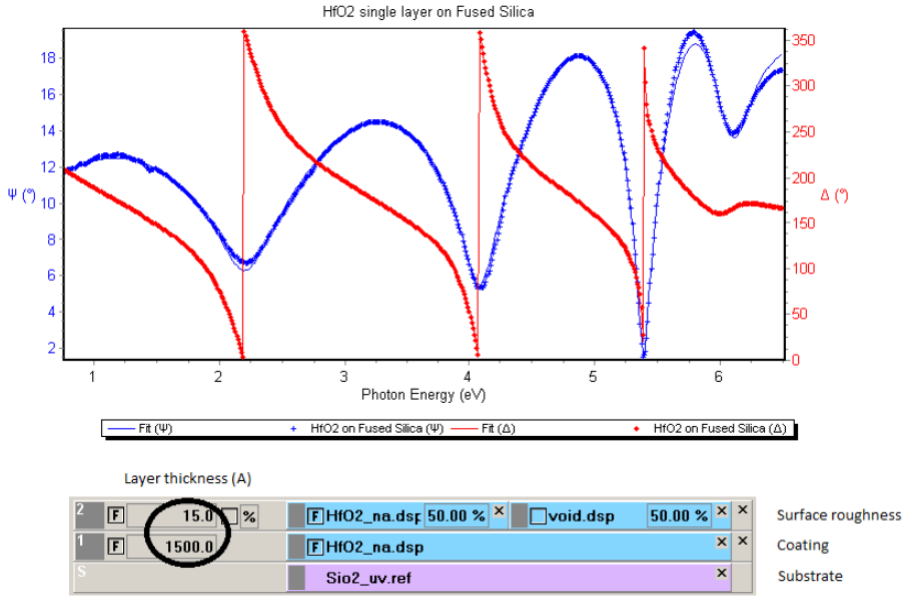

Figure 2.15: Fitted ellipsometry data and the accompanying model. The HfO2na.dsp is a new amorphous dispersion model.

the same ellipsometer. For the coating layer, neither the optical constants nor the thickness is known, so a .dsp layer is used. There are many models that can be used in .dsp layers to model dispersion and absorption. Different dispersion models are applicable to different materials and photon energy ranges. In this work, the "new amorphous" model was used to model HfO_2 single layers. The new amorphous model is an oscillator model which is based on physical phenomena. Equations 2.16 and 2.17 are used to calculate $n(\omega)$ and $k(\omega)$ in the new amorphous model[25].

$$n(\omega) = n_\infty + \frac{B(\omega - \omega_j + C}{(\omega - \omega_j) + \Gamma_j^2} \tag{2.16}$$

$$k(\omega) = \begin{cases} \frac{f_j(w-w_g)^2}{(w-w_j)+\Gamma_j^2} & \omega > \omega_g \\ 0 & \omega < \omega_g \end{cases} \tag{2.17}$$

where

$$B = \frac{f_j}{\Gamma_j}\left[\Gamma_j^2 - (\omega_j - \omega_g)^2\right] \tag{2.18}$$

$$C = 2f_j\Gamma_j(\omega_i - \omega_g) \tag{2.19}$$

n_∞ is the long wavelength refractive index, ω_j is the energy of maximum absorption, f_j is the oscillator strength, w_g is the bandgap energy, Γ_f is the broadening factor for the absorption peak. All of these parameters are fitted during the modelling process, along with the layer thickness and the surface roughness. Surface roughness is modelled using an effective medium approximation (EMA). EMA approximates roughness by a intermediate layer between the air and the film by a thin layer made up of 50% air and 50% coating. This method for approximating surface roughness is inherently inaccurate because it assumes the voids are evenly distributed through the thickness of the layer which is not typical of surface roughness. Due to the typically Gaussian distribution of surface heights in random roughness surfaces, the voids in the roughness layer are concentrated near the top of the layer (as shown in figure 2.16). This roughness value fit by the ellipsometer is typically around 0.3 to 0.7 nm, which is in the range of RMS values measured by the atomic force microscope. The ellipsometer values do not correlate directly to the AFM measurements and have been shown in other work to be less accurate[46].

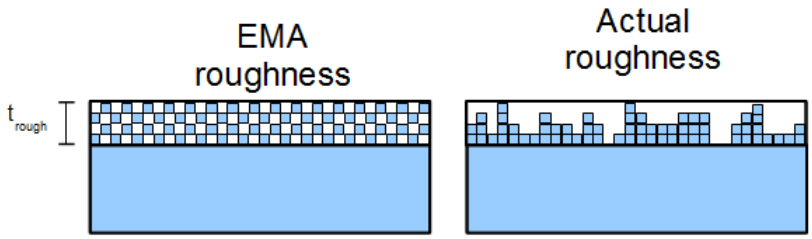

Figure 2.16: figure depicting the problem with the EMA in terms of the location of voids within the roughness layer.

The goodness of fit (χ^2) is calculated by equation 2.20 where Ψ_{calc} and Δ_{calc} are the values calculated for the model and Ψ_{exp} and Δ_{exp} are the experimentally measured values. Γ_i is the standard deviation of the experimentally measured value at a particular wavelength. Generally (χ^2) below 10 is considered to be a good fit. Care was taken to ensure that the minimum reached is not a local minimum but rather the global minimum for the fit by knowing and inputting as much information about each sample as possible[25].

$$\chi^2 = min \sum_i = 1^n \left[\frac{(\Psi_{calc} - \Psi_{exp})_i^2}{\Gamma_{\Psi,i}} + \frac{(\Delta_{calc} - \Delta_{exp})_i^2}{\Gamma_{\Delta,1}} \right] \tag{2.20}$$

2.2.5 Spectrophotometer

A spectrophotometer is a fairly simple way of directly measuring transmittance of transparent and semi-transparent samples. Lamps are used to create spectrally broad illumination. A monochromator is used to narrow the illumination spectrum. The monochromater is a grating that reflects different wavelengths of light at different angles. A variable width slit is used to limit the range of wavelengths that illuminate the sample. The light passes through the sample at normal incidence before being collected by a photodiode. The same measurement is made with and without the sample in the beam. The transmittance is then calculated by $T = \frac{P_T}{P_0} = \frac{V_T}{V_0}$, where P_T is the power transmitted through the sample, P_0 is the intensity of the light before the sample, V_T is the output voltage from the photodiode with the sample in the beam path and V_0 is the output voltage from the photodiode with no sample in the beam path. Figure 2.17 shows this setup.

The spectrophotometer used in this experiment is a Hitachi U-2010 UV/VIS which has a wavelength range of 190nm through 1100nm. Two lamps are used to achieve this range - a deuterium lamp produces broadband UV light from 190 to 450nm and a tungsten iodide lamp produces broadband light from 450 to 1100 nm[3].

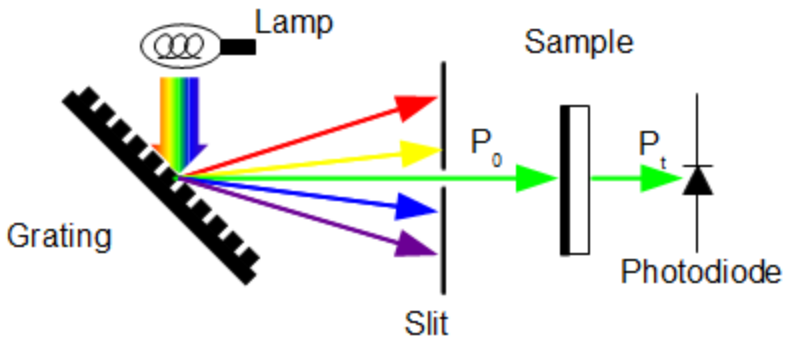

Figure 2.17: Diagram of a simple single-beam spectrophotometer.

A typical transmission spectrum for a hafnium oxide coating on a fused silica substrate and an uncoated fused silica substrate are shown in figure 2.18.

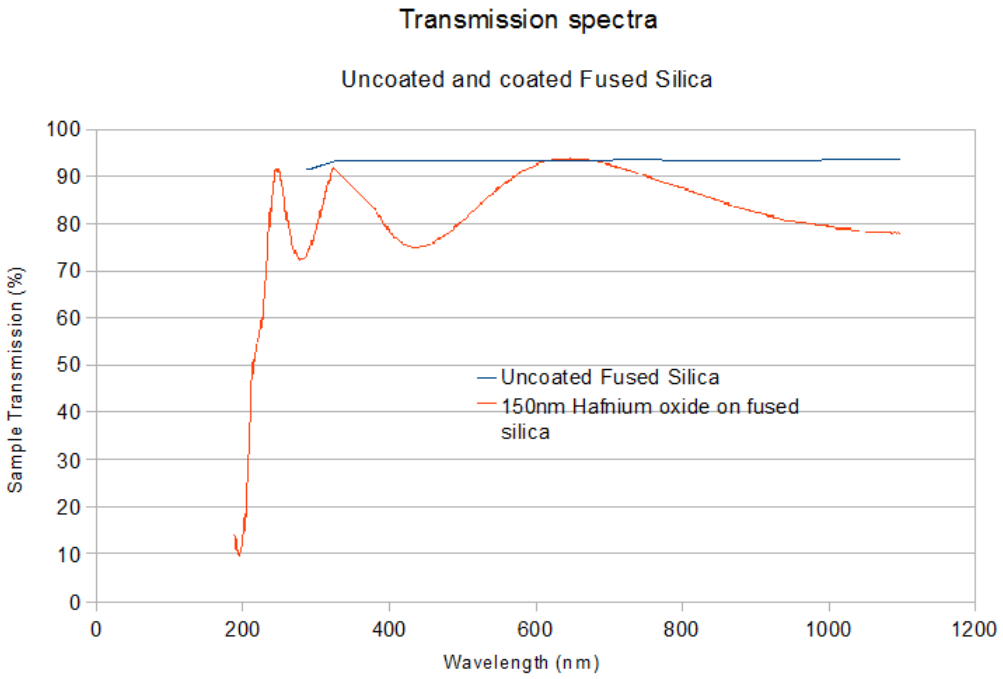

Figure 2.18: Typical transmission spectra for an uncoated UV grade fused silica and UV grade fused silica coated with 150nm thick layer of HfO_2. The loss in transmission of the uncoated substrate is due to Fresnel losses (4% at each interface). The coated sample suffers decreased transmission (increased reflectance) at wavelengths where the optical thickness of the film is an integer multiple of $\lambda/4$. The transmission of the coated sample drops more significantly as the photon energy approaches the HfO_2 bandgap of approximately 6eV (200nm).

Chapter 3

Results and Discussion

This chapter details the results of a systematic study of single layer HfO_2 thin film surface roughness, scatter loss and other performance characteristics. These characteristics are examined as a function of beam voltage during deposition, substrate choice and film thickness. Section 3.1 examines the effect beam voltage during deposition and the role of substrate choice. Section 3.2 examines the effect of film thickness on the surface quality and scatter loss. Section 3.3 compares a multilayer coating deposited at CSU with an identical coating created by a commercial company. Each section begins with a presentation of the results followed by a discussion.

3.1 Set 1: Beam Voltage

Single layer thin films of amorphous HfO_2 are deposited optical substrates with different main source beam voltage. All other deposition parameters including film thickness are kept constant. Figure 3.1 shows the deposition parameters that are used for each sample. Three different types of substrates are coated at each beam voltage to examine the role of substrate choice on scatter properties and surface roughness. Figure 3.2 gives the details of each of the substrates used in this experiment.

Sample	Beam Voltage (V)	Substrates	Beam Current (mA)	Thickness (nm)
1	600	A,B,C	400	150
2	800	A,B,C	400	150
3	1000	A,B,C	400	150
4	1250	A,B,C	400	150

Figure 3.1: Deposition parameters for the samples characterized in this section. Details for the substrates can be found in figure 3.2.

Substrate	Material	Structure	RMS Roughness (nm)	Thickness (mm)	Diameter (mm)
A	Fused Silica	Amorphous	0.1	6.4	25.4
B	Sapphire	Crystalline	0.1	3.0	25.4
C	Fused Silica	Amorphous	0.6	6.4	25.4

Figure 3.2: Details for the three substrates upon which HfO_2 thin films were deposited.

3.1.1 Deposition Rate

The deposition rate for each film is determined by measuring the film thickness and dividing by the deposition time. Film thickness was measured using spectroscopic ellipsometry. The deposition rate as a function of beam voltage (V_b) is shown in figure 3.3.

The growth rate increases with beam voltage. The increased energy of the sputtering atoms increases the sputtering yield which in turn increases the rate at which the atoms reach the sample surface. For the three lower beam voltages the relationship is quite linear ($r^2 > 0.99$), which is reasonable given that the sputter yield is related to the energy of the bombarding atoms in that range [37]. It is not clear why the linear relationship does not hold for the 1250V sample. The factory recommended beam voltage for the DIBS system is 1250V to achieve the fastest deposition rate.

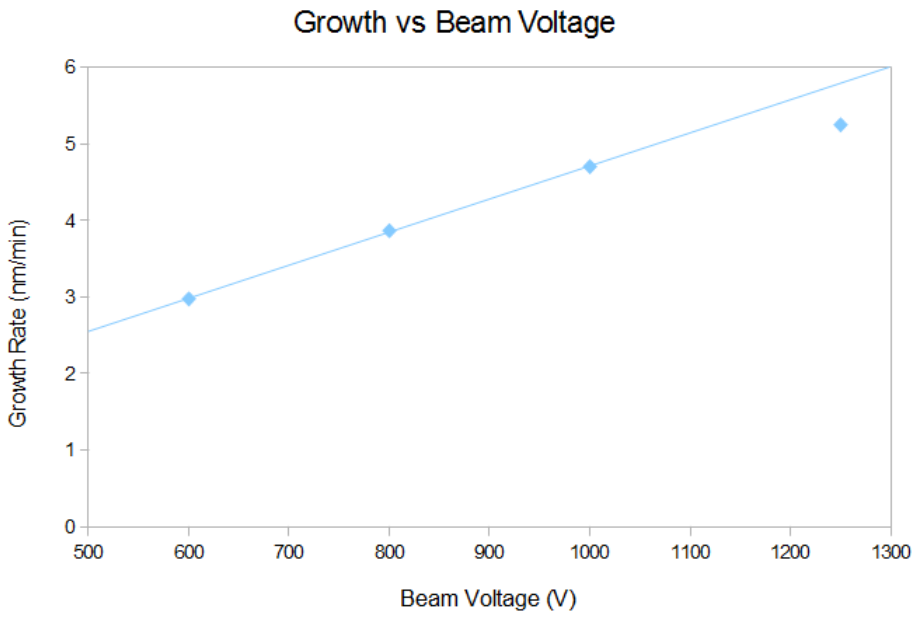

Figure 3.3: Growth rate for samples grown with different beam voltages.

3.1.2 Optical constants

Refractive index and extinction coefficient curves were calculated for each sample using spectroscopic ellipsometry. Ellipsometric data were measured at 65° angle of incidence from 190 to 2100nm, and then fitted using a "new amorphous" model. The index of fraction and extinction coefficient (k) are calculated from the model parameters.

The refractive index and extinction dispersion are shown in figure 3.5. For practical purposes, the extinction coefficient is zero at 1064nm, the design center wavelength of interest in this work.

The refractive index at 1064nm is shown in figure 3.4 as a function of beam voltage. No trend is evident, and over the whole spectrum of beam voltage there is less than 0.2% change in index of refraction. This suggests that there is little structural change (for example packing density or void fraction) between different beam voltages.

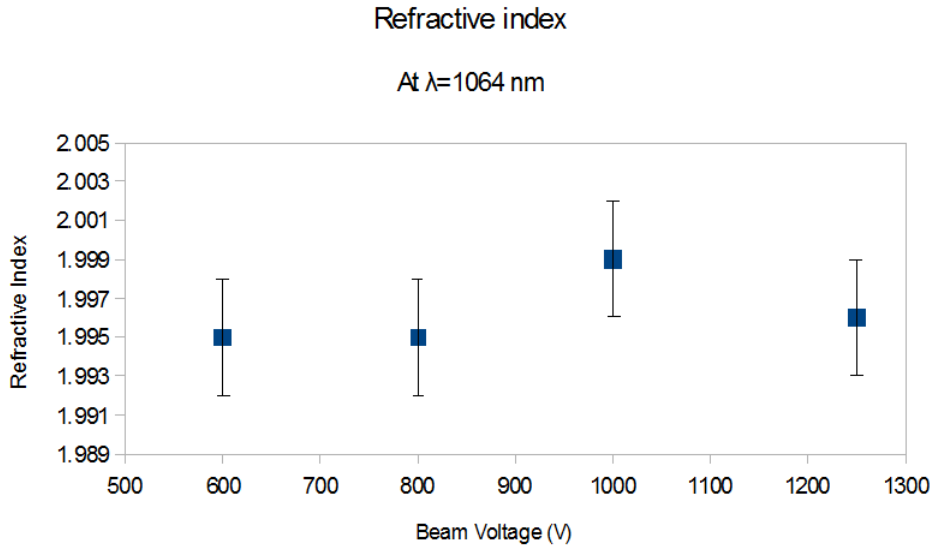

Figure 3.4: Index of refraction of thin films as a function beam voltage during deposition.

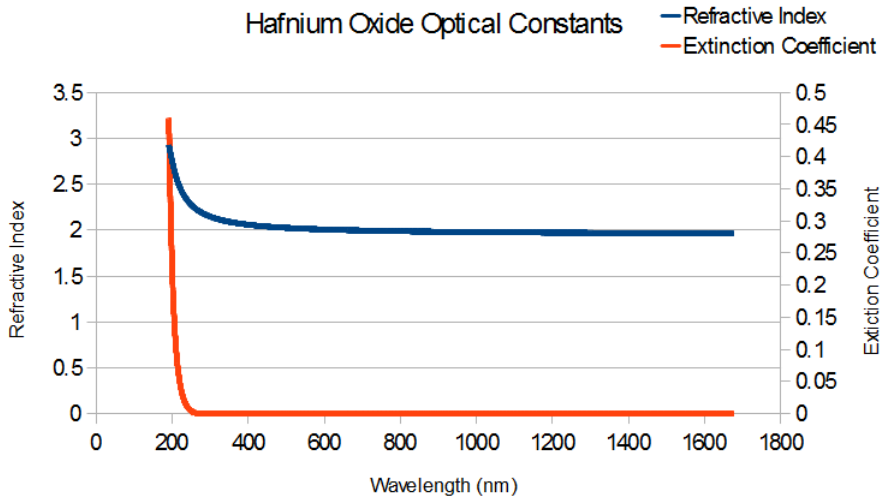

Figure 3.5: An example index of refraction spectrum for HfO2. At 1064nm it is approximately 2.

3.1.3 Surface Roughness

Sample surfaces were mapped using atomic force microscopy (AFM) and white light interferometry (WLI). In both techniques a three dimensional map of the surface is created. The map is a two dimensional grid of surface heights. From these maps, various statistics are calculated.

Atomic Force Microscopy

Coatings deposited on substrates A and C were profiled using a Novascan SPM 3D atomic force microscope. Each scan is conducted with a $15\mu m$ scan size, and a resolution of 500 pixels per line (so each pixel is 30nm). Surface maps were recorded at three positions on the sample, approximately 5mm apart. From these scans, the root mean squared (RMS) roughness was calculated using equation 1.13 and then averaged across all three measurement locations.

Figure 3.6 shows the calculated RMS roughness for each sample as a function of beam voltage for different substrates. Figure 3.6 (a) compares substrates A and B. Not surpisingly since the surface quality of the uncoated substrates is very similar, the two behave very similarly. Each show a trend towards increasing RMS roughness with increasing beam voltage. In both cases, the sample coated at 600V has a roughness very close to that of the substrate indicating a very smooth coating with limited roughness enhancement. When deposited at higher beam voltages (1000V and especially 1250V), the roughness increases significantly when compared to that of the substrate.

Figure 3.6 (b) compares a high quality substrate (substrate A) with the lower quality substrate (substrate C). The values for substrate A are the same those seen in Figure 3.6 (a). Like samples grown on the smoother substrates, the coating grown at 600V on the lower quality substrate matches very closely the roughness of the uncoated substrate, again indicating a smooth coating that does not enhance the

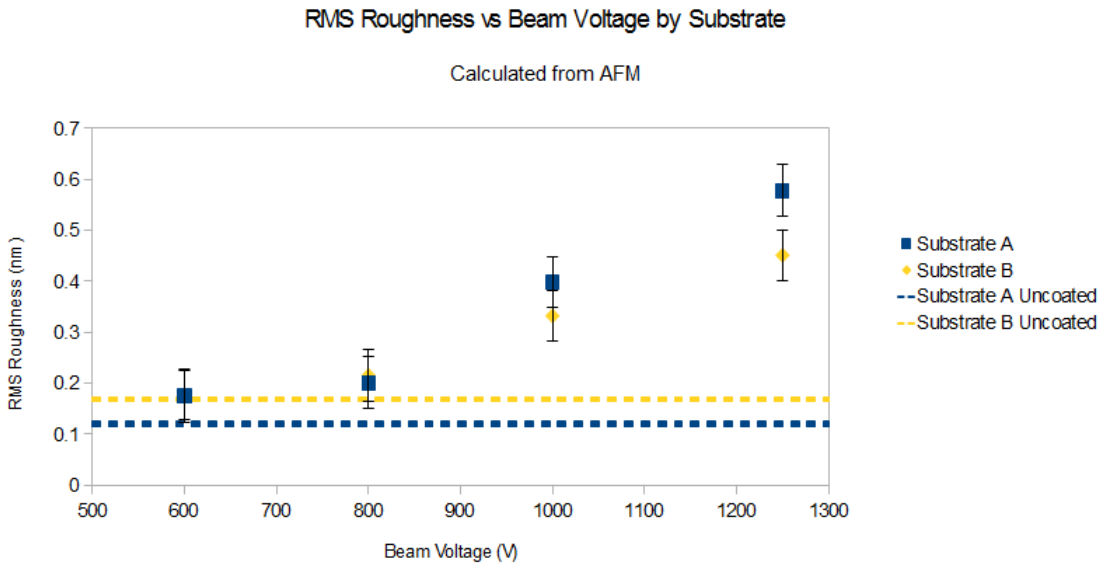

(a)

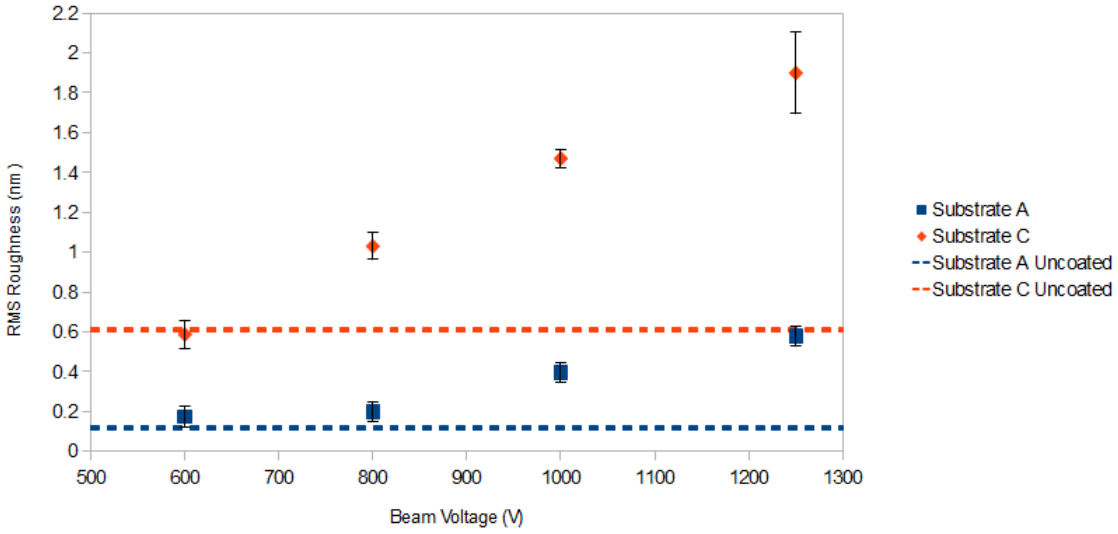

(b)

Figure 3.6: RMS roughness for hafnia thin films as a function of beam voltage for different substrates. (a) compares films grown on the two super polished substrates (A and B). (b) compares films grown on a super polished substrate (A) with films grown on the less polished substrate (C). The dotted lines indicate the average RMS roughness for the uncoated substrate each of the samples is grown on.

roughness of the substrate much if it at all. However, as beam voltage is increased, the roughness of the coatings on the lower quality substrates increases significantly. The reason for this more exaggerated increase in roughness is not clear. Pits do tend to concentrate along scratch marks on the substrate, so the increased number of scratch marks may cause an increase in the number of pits that are created.

RMS roughness is a good first order benchmark of the quality of a surface, but does not do much to predict scatter performance of a surface or to explore the types of features causing the roughness. Roughness can take the form of pits, or peaks of different heights and widths, and is usually a combination of both. A qualitative visual inspection of the scans showed that for most of the samples the surfaces are made up mostly of flat plateau type features with deep pits and occasional gouges or trenches. Very few significant peaks were found on any of the samples.

On the smooth substrates (A,B), the plateau areas (those without pits) appeared to be much smoother than on the rough substrate (C), and seemed to match the surface quality of the substrate. The concentration of pits also appears to be much larger on the lower quality substrate, even though no pits are present on the uncoated substrates. Also, the concentration of pits appears to increase with increasing beam voltage. The height histogram for these scans also shows the presence of pits through a slight skew towards lower surface heights and a long raised tail on the lower end of the gaussian. Figure 3.7 shows some scans from different coatings. Figure 3.8 shows the pit map for each of the scans in figure 3.7.

To attempt to explore the role of pits in sample surfaces in a more quantitative manner, a matlab program is used to identify pits. The program outputs a "pit count" as well as a "pit area" which is the fraction of the surface that is covered in pits. Because the pits and gouges have different sizes, the pit area is a more useful way to quantify pits. The results from this study are shown in figure 3.9. For all three substrates, the larger beam voltages show larger pit area values. Samples grown on

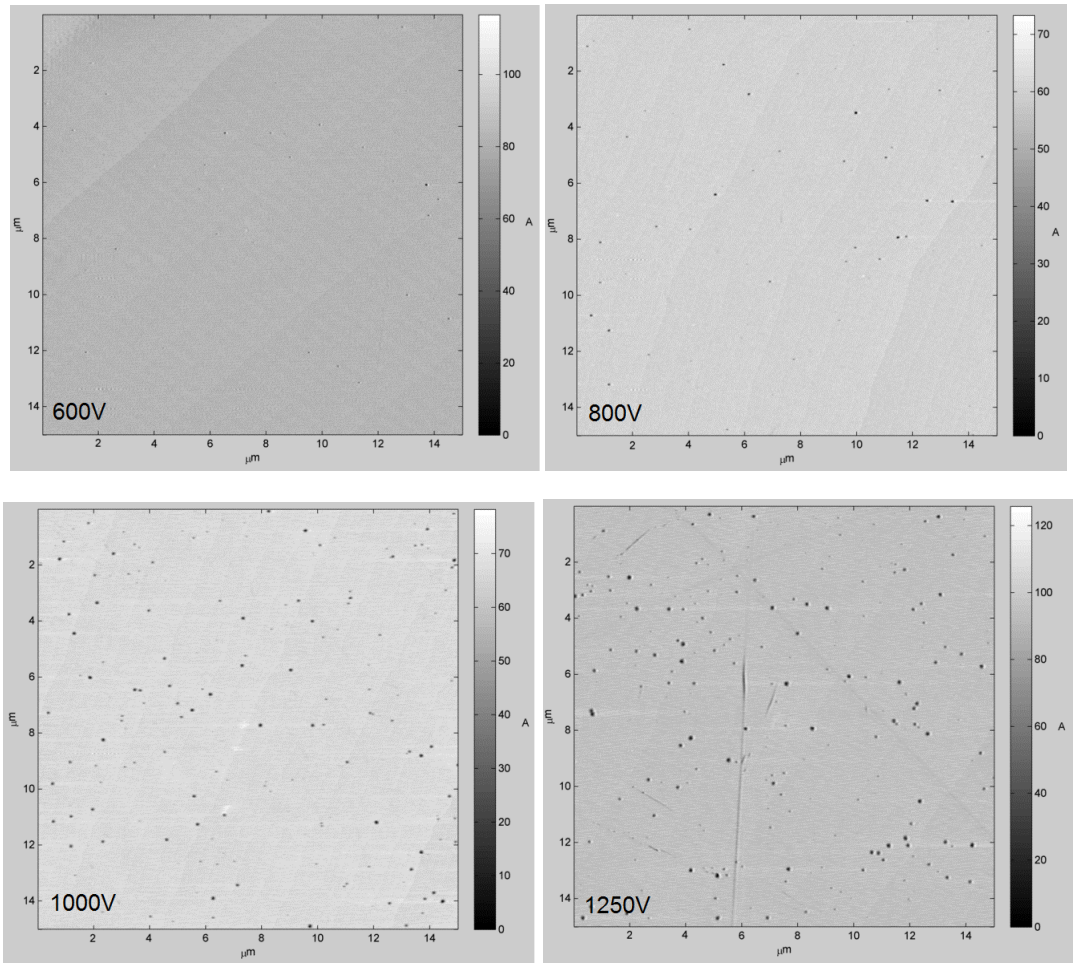

Figure 3.7: AFM scans of samples deposited with different beam voltages on Substrate A.

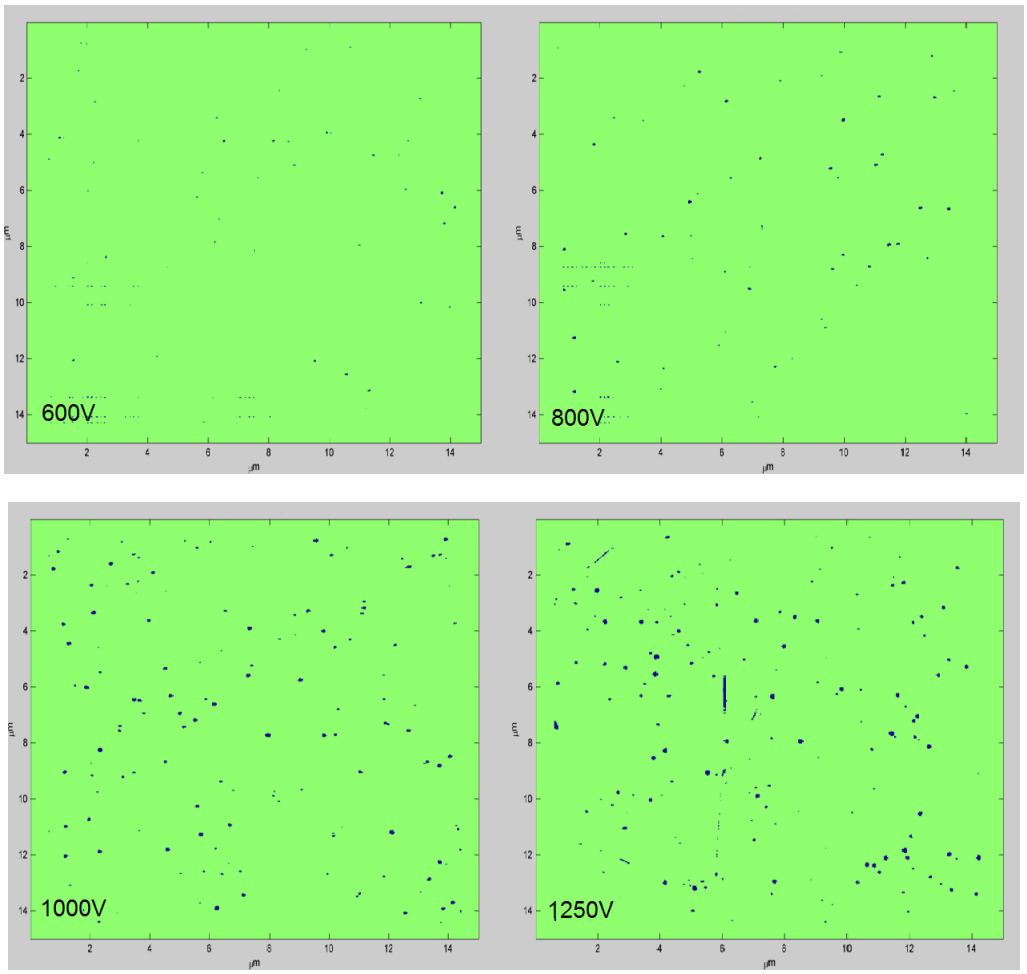

Figure 3.8: Pit maps for the AFM scans in figure 3.7.

the lower quality substrate have a larger pit area at all beam voltages, and samples grown on the two higher quality substrates (A,B) act very similarly to one another at all beam voltages. The quantitative analysis agrees with the qualitative analysis and suggests that increasing surface roughness is likely mostly due to increasing concentration of pits. It should be noted, that the depth of the pits could not be accurately measured due to limitations with the measurement technique; the aspect ratio of the tip does not allow it to reach the bottom of deep narrow pits such as the ones that exist on these samples.

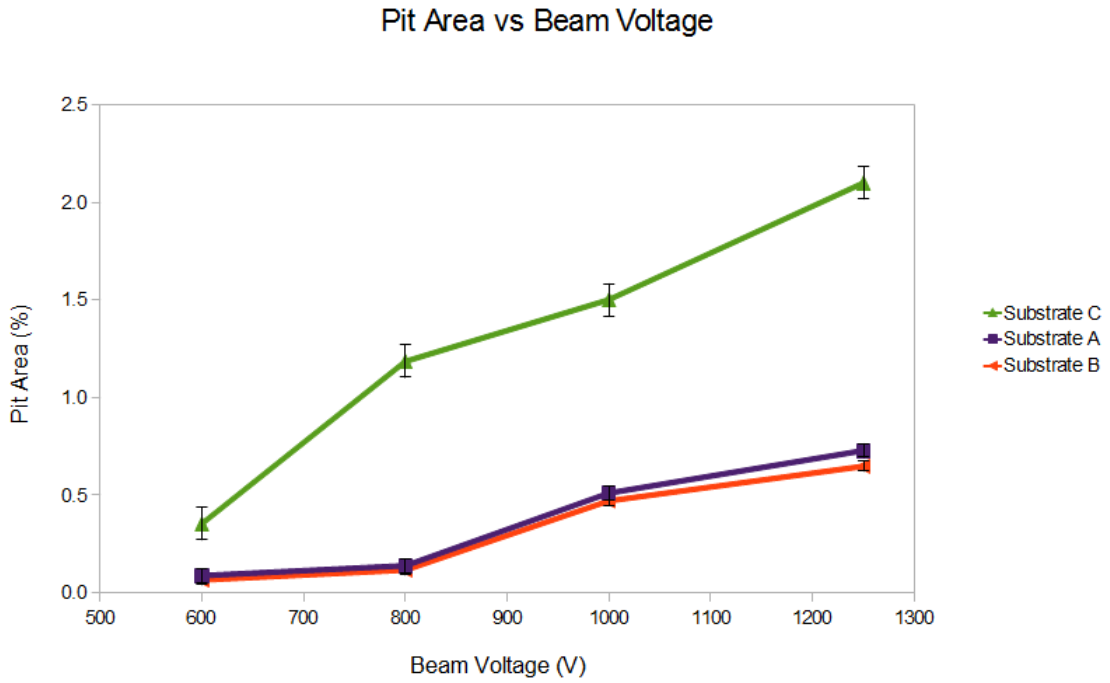

Figure 3.9: Pit area as a function of beam voltage. The lower quality substrate shows a significant increase in pit area with beam voltage. The higher quality super polished substrates show some increase, though a less significant amount.

White light interferometry

Coatings deposited on substrates A and C are profiled using a Veeco WYKO white light interferometer (WLI). Surface maps were recorded at three positions on the sample, approximately 5mm apart. The scans are recorded with the highest magnification

lens and have scan size of 91x120μm and a pixel size of about 160nm. From these scans, the RMS roughness is calculated using equation 1.13 and then averaged across all three measurement locations. Figure 3.10 shows the average RMS roughness vs beam voltage during deposition. Figure 3.11 shows a WLI scan of the 600V sample on Substrate A and Substrate C.

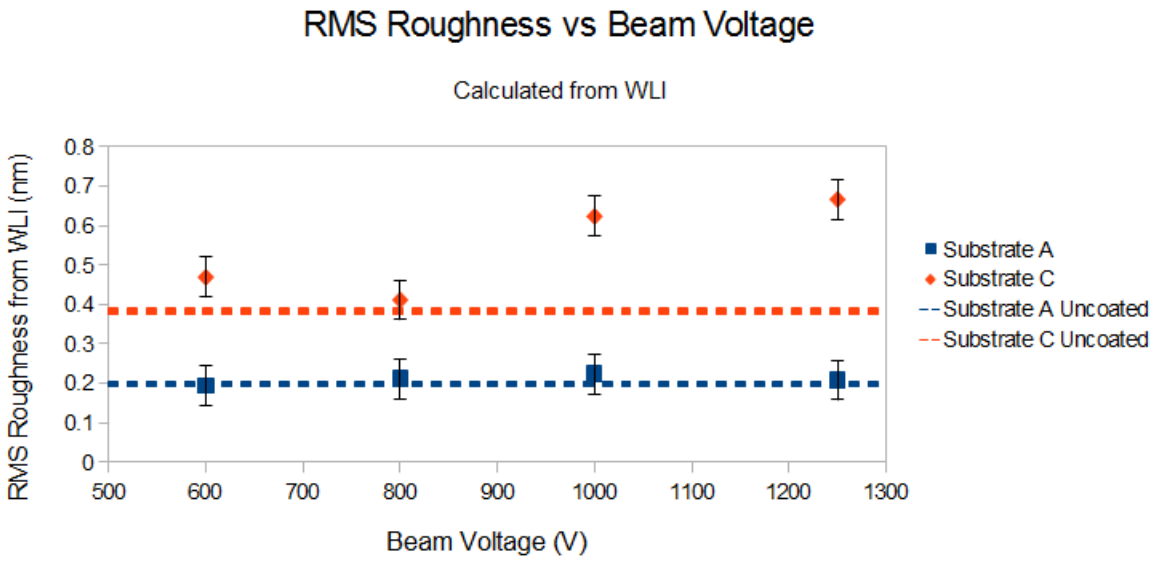

Figure 3.10: RMS roughness calculated from WLI surface maps as a function of beam voltage. The error bars are are the absolute error of the instrument as quoted in the Veeco manual. AFM roughness and WLI roughness measurements are always different as the two techniques sample different spatial frequency ranges.

Samples deposited on the higher quality substrate show no appreciable trend with increasing beam voltage. It should be noted, however, that all the samples measured were approximately at the detection limit of the interferometer (0.2nm). For the same samples deposited on the lower quality substrates (substrate C), there is a trend towards increasing RMS roughness for increasing beam voltage, though the RMS roughness of the 800V samples is slightly lower than that of the 600V sample. The higher beam voltage samples did not show the same sort of plateau and pit surface profile that the AFM did, but this is not surprising as the lateral resolution

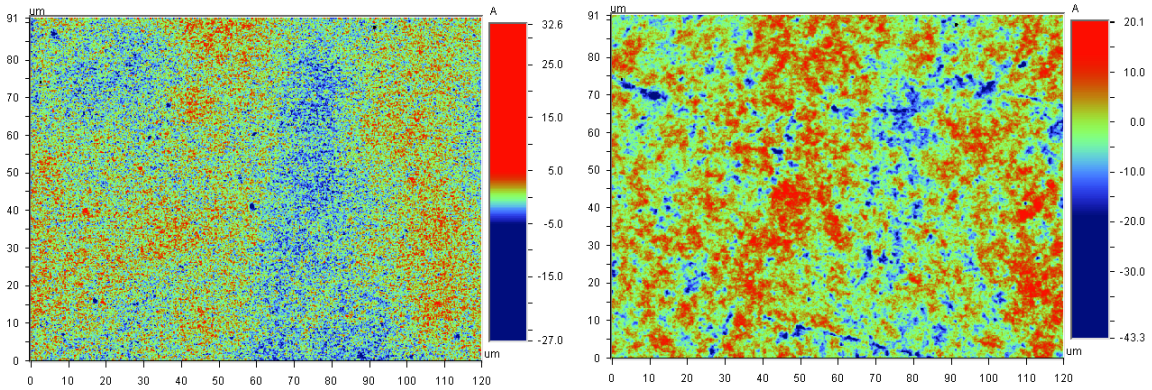

(a) (b)

Figure 3.11: Example WLI scans of thin films deposited on different substrates. (a) Substrate A. (b) Substrate C. (a) is smooth enough that it is below the detection limit of the device.

of the WLI is approximately the same size as the pits (150nm).

The increasing roughness with beam voltage likely does not stem from the increase in pits seen in the AFM measurements, but rather from larger features which also appear to increase with beam voltage. The WLI calculated RMS roughness is a better benchmark of the likely NIR scatter loss of the surface than the AFM calculated RMS roughness because it can profile the right range of spatial frequencies. See figure 1.18 for the spatial frequencies sampled by AFM and WLI as well as the spatial frequency ranges that are most important at each scattering wavelength. The range of frequencies the WLI samples overlaps nicely with the range of frequencies of interest for scattering at 1064nm.

Figure 3.12 shows overlaid histograms for samples deposited at different beam voltages. Each subplot is for different substrate. The difference between the substrates is clear. The samples deposited on higher quality substrates have narrower more uniform histograms. There is some broadening of the histograms with larger beam voltages on substrates A and B, but the rehistograms remain uniform. On substrate C, the left (lower) tail of the gaussian shows an increase with beam voltage. There is also some broadening of the histogram with increased voltage, but it is fairly

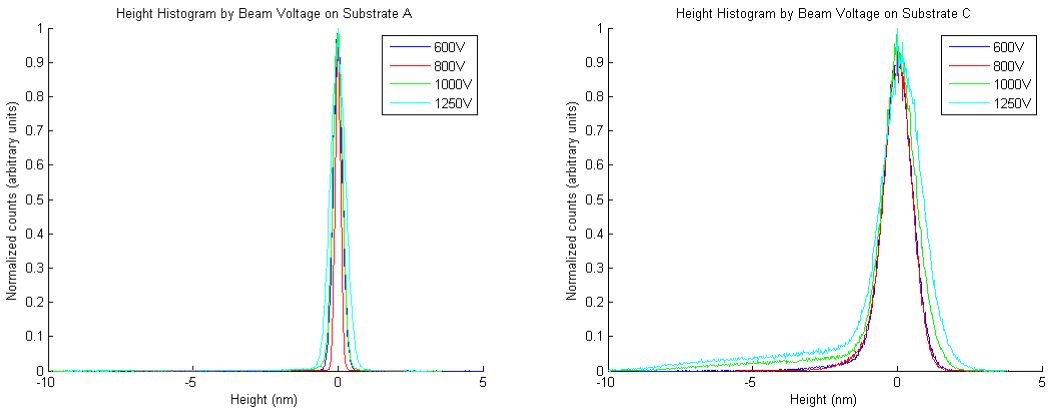

(a)

(b)

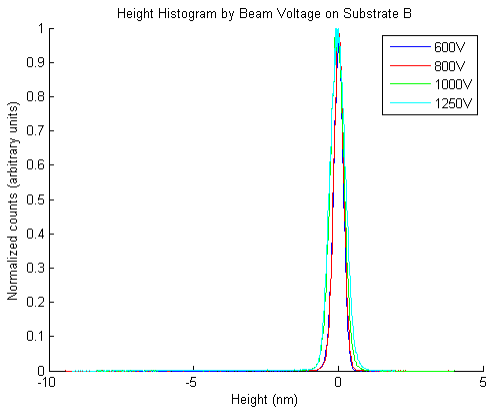

(c)

Figure 3.12: Height histograms by voltage on (a) substrate A, (b) substrate B, (c) substrate C.

insignificant when compared with the increase in the lower tail. This also supports the idea that most of the increase in roughness on the samples on substrate C comes from the increasing concentration, size and depth of pits whereas the increase of the roughness of the samples on substrates A and C is more randomly distributed and therefore increases the breadth of the histogram, but does not raise the lower tail disproportionately.

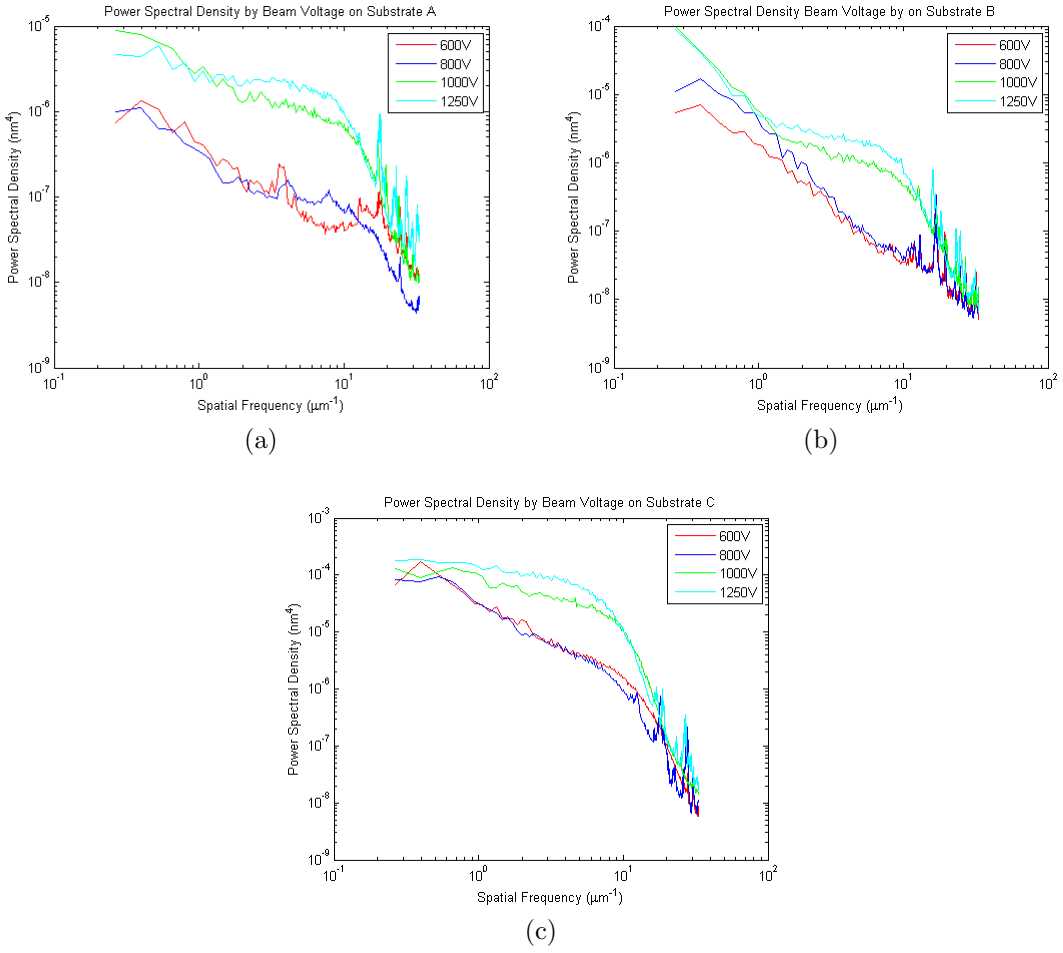

Figure 3.13: Power spectral density of samples with different beam voltages on (a) substrate A, (b) substrate B, (c) substrate C

RMS roughness and pit area are good first order benchmarks of a surface, but do not differentiate the spatial feature sizes (spatial frequencies) that are responsible for the roughness. Power spectral density analysis can do this. PSD plots are a useful

tool in understanding the relative contributions of different feature sizes to the overall roughness. By looking at how the PSD evolves from sample to sample, it is possible to see what types of features get larger. Figure 3.13 shows overlaid power spectral density (PSD) plots for samples with different beam voltages. Each subplot contains the same set of samples deposited on different substrates.

On substrate A, there is very little change from 600V to 800V or from 1000V to 1250V. There is however a fairly significant increase from 800V to 1000V that is spread across the entire PSD, with the largest increase at higher spatial frequencies (3-10 μm^{-1}). This indicates that scattering at all three wavelengths are affected, but 405nm and 633nm more so then 1064nm.

The same samples on substrate B act very similarly except that the PSD for the 800V sample which higher than the 600V sample, and closer to the 1000V/1250V sample. The PSD increases more in the 3-10 μm^{-1} range, but also shows an increase similar to the increase seen in the samples on substrate A at low spatial frequencies. Based on the PSDs, the samples on substrates A and B should perform quite similarly in how they scatter light across a range of wavelengths.

The PSD plots for substrate C have a slightly different appearance. The PSDs show an overall increase with beam voltage as is expected based on the RMS roughness results. All the PSDs are at fairly high values compared to those seen on the other substrates, which is again reasonable given the higher RMS that the samples on substrate C show. The main difference between between the PSD plots for substrate C, versus those for substrates A and B is that the increase with beam voltage appears to be limited to higher spatial frequencies; figure 3.13 (a) shows the same 'bump' seen in (b) and (c) at higher spatial frequencies, but at the low end of the spectrum, all the PSD plots for substrate C are nearly identical.

Figure 3.14 shows the same data as in figure 3.13, but arranged so that the substrates can be compared. Substrate C is consistently worse than A and B. The film

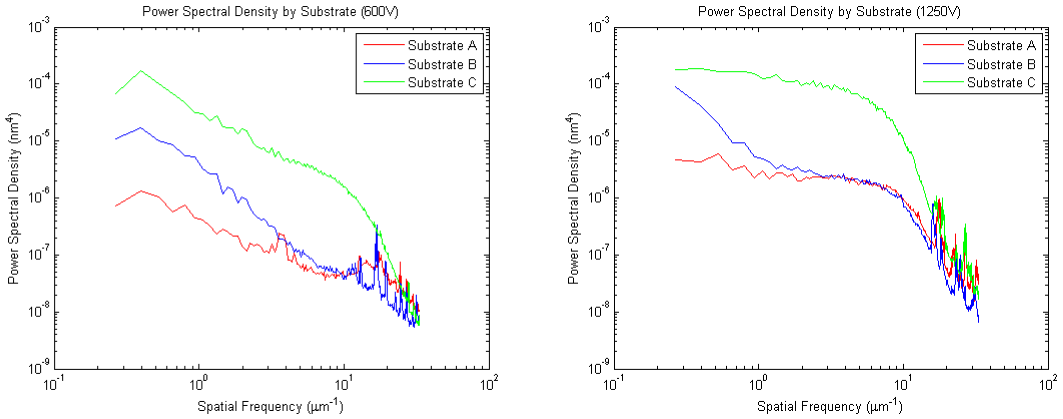

(a) (b)

Figure 3.14: Power spectral density by substrate at (a) 600V and (b) 1250V.

grown on substrate A and B are very similar, except that the film on substrate A is slightly smoother at low spatial frequencies. This indicates that substrate A should be slightly better then substrate B at long wavelength. At low spatial frequencies, both substrate A and B are very similar, especially at higher beam voltage, probably because the high spatial frequency roughness is driven mostly by the pit concentrations in these samples.

3.1.4 Scatter loss

Forward scatter loss (TS_f), and backscatter loss (TS_b) were measured individually for each sample at three optical wavelengths: 405nm, 633nm and 1064nm. Total scatter loss (TS) was then calculated by summing TS_f and TS_b. Not surprisingly, scatter performance is very much dependant on the substrate choice, so sets of samples on substrate B and C are discussed individually. Substrate A is omitted from the scattering discussion because inconsistent back surface polish skewed the data significantly. A comparison of the 600V film on each substrate follows at the end of this section.

Substrate B

A plot of total scatter loss vs beam voltage for substrate B is shown in figure 3.15. (a) shows TS at all three wavelengths (405nm, 633nm, and 1064nm) simultaneously as a way to compare the magnitude. (b)-(d) show the individual sets of data along with the TS value for the uncoated substrate. All three sets of data show the same trend - increasing scatter loss with increasing beam voltage. Scattering at 405nm and 633nm shows a fairly sharp increase, particularly from the 1000V to the 1250V sample. However, the scattering at 1064nm does not increase nearly as rapidly. Even the 1250V sample suffers only a very acceptable 6.7 ppm scatter loss. Though the lowest beam voltage value is half of that value, in absolute terms, a decrease of 3ppm is not much. The relative magnitude of the increase over different wavelengths is discussed more thoroughly in section 3.1.7.

An interesting feature of all these sets is that the low beam voltage sample has a scatter loss value lower than the substrate. This indicates that the coating may actually be smoothing out some polishing marks on the substrate.

Substrate C

A plot of total scatter loss vs beam voltage for substrate C is shown in figure 3.16. Figure 3.16 (a) is a plot of all three wavelengths together to show relative magnitude. Note that it is on a logarithmic scale for cleaner display. Figure 3.16 (b) - (d) show scattering at each wavelength independently. As with substrate B, all three sets show trends towards greater scatter at higher beam voltages. Scattering at 405nm and 633nm show a sharp increase with beam voltage, but the trend of scattering at 1064nm is less clear.

The sharp increase in scattering at lower wavelengths is likely related to the concentration of pits. The pits are about the right size to affect scattering at 405nm and 633nm but are small enough that 1064nm light does not "see" them. Given the

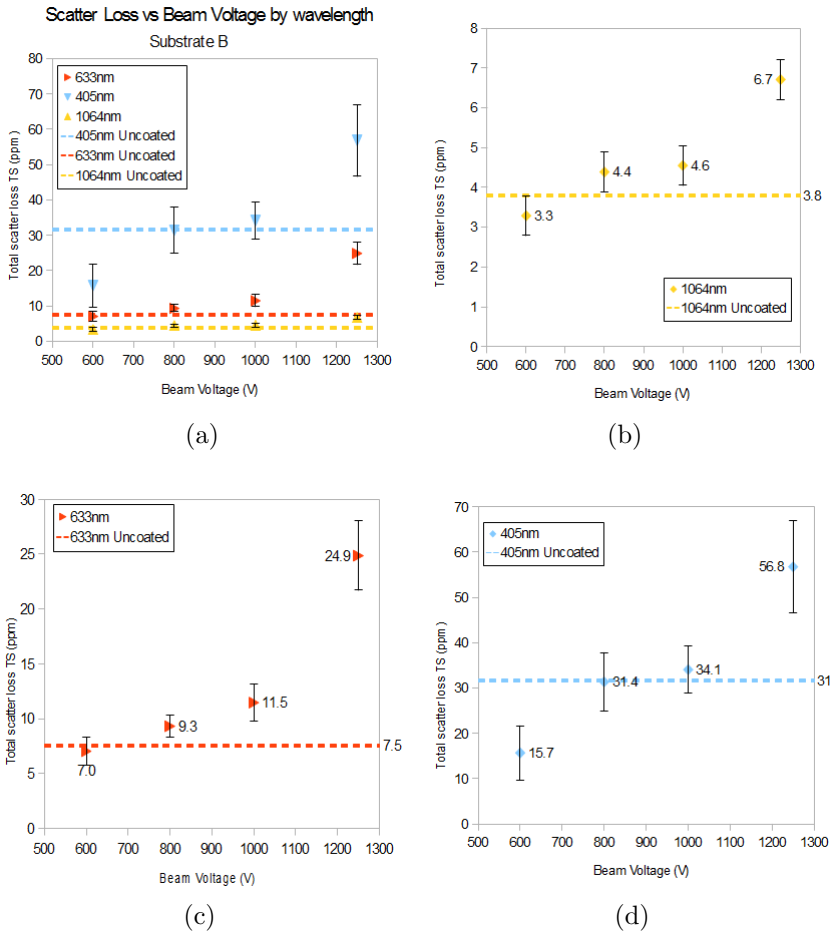

Figure 3.15: TS vs beam voltage for substrate B.

quality and price of the original substrate, the scattering values at 1064nm again are quite acceptable, and don't show significant improvement at lower beam voltage.

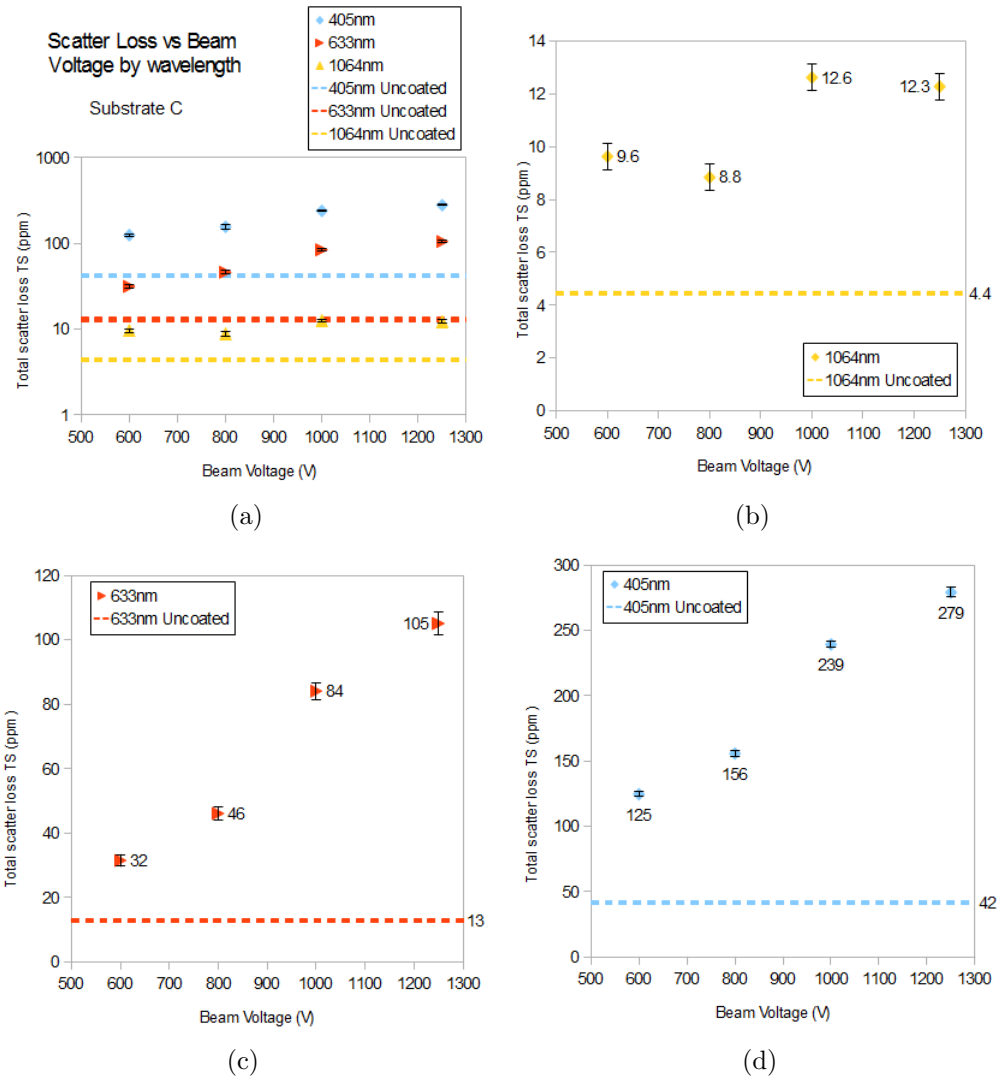

Figure 3.16: TS vs beam voltage for substrate C.

Substrate comparison

A plot of scattering vs wavelength for samples grown on different substrates in the same coating run is shown in figure 3.17. The high quality substrates perform very similarly to one another, and significantly better than the lower quality substrate at 405nm. At 633nm and especially 1064nn all three substrates perform quite similarly.

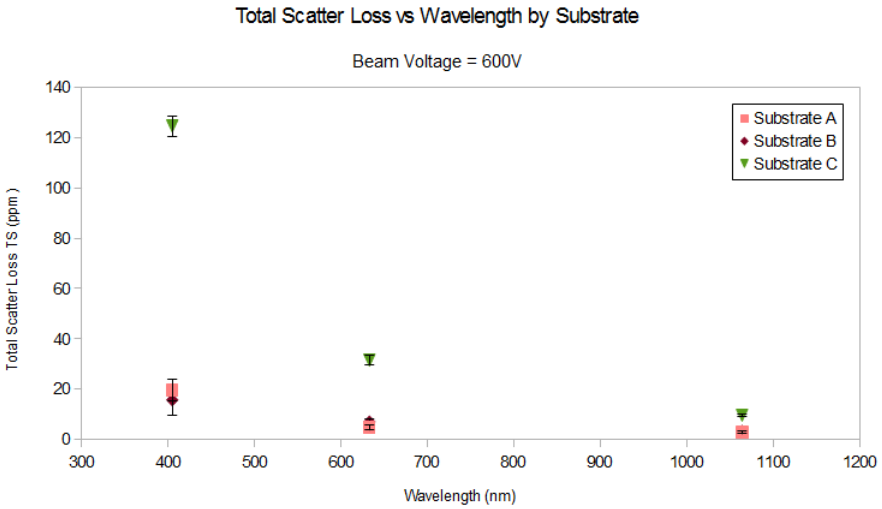

(a)

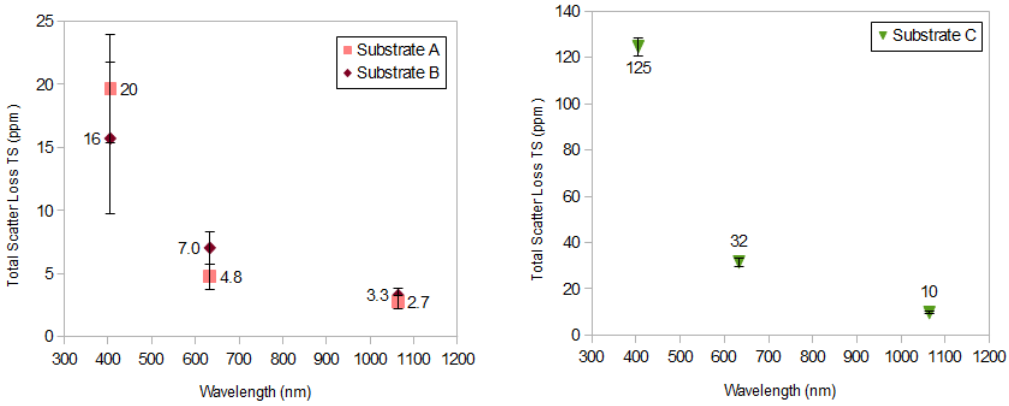

(b) (c)

Figure 3.17: TS vs wavelength by substrate.

3.1.5 Absorption at 1064nm

Absorption at 1064nm was measured with a photothermal commonpath interferometer (PCI). PCI is a pump/probe experiment in which a beam at the wavelength of interest is focused on the coating. The absorption of energy from the pump beam causes a thermal lens in the coating. The probe beam passes through the same spot. The part of the probe beam that is redirected by the thermal lens becomes one arm of the interferometer, and the part that passes through around the thermal lens makes up the other arm of the interferometer. A more thorough description of a PCI and how it works is found in [6].

A plot of absorption vs beam voltage is shown in figure 3.18. Decreasing beam voltage shows slightly increased absorption, except at 1250V, which is close to the 600V value. Though the changes are small, the trend generally opposes the trend for scatter loss at 1064nm in the same samples.

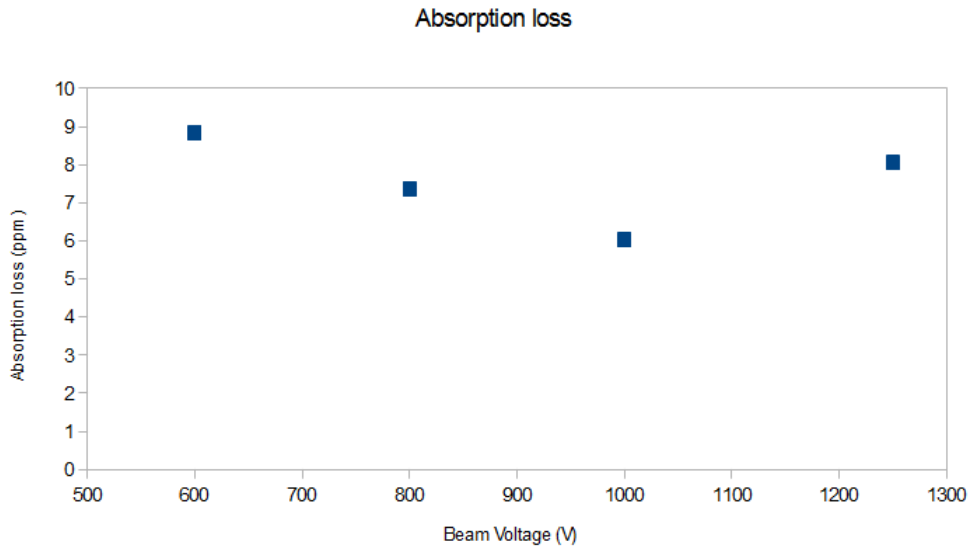

Figure 3.18: Absorption loss at 1064nm as a function of beam voltage.

3.1.6 X-ray diffraction

Grazing incidence x-ray diffraction (GAXRD) was conducted on all samples to determine if there is a change in the degree of crystallinity in the samples. Figure 3.19 shows the results for all four samples overlayed. All four samples show nearly identical peaks. The only peak is at 32°, and has a full width half max of 5°. The crystallite size can be calculated with Scherrer's equation[31]:

$$D = \frac{0.9\lambda}{B\cos\theta} \tag{3.1}$$

Where D is the crystallite size, B is the FWHM of the peak (in radians), and 2θ is the position of the peak. Plugging in the values for the peak position and full width half max gives an approximate crystallite size of 1.7nm which means that the material is nearly completely amorphous. The most important result from GAXRD is that there is no change from one sample to another.

3.1.7 Discussion

The roughness and scattering results seem to be in qualitative agreement that lowering beam voltage from 1250V to 600V creates smoother coatings with less scatter. To compare the techniques numerically, equation 3.2 (a rearrangement of equation 1.40) can be used to calculate a "predicted roughness" (σ_p) value.

$$\sigma_p = \sqrt{\mathrm{TS}}\frac{\lambda}{4\pi} \tag{3.2}$$

By comparing the predicted roughness of scatter at each wavelength, an estimate of which parts of the spatial frequency spectrum are changing between samples can be achieved. Figure 3.20 (a) shows a plot of predicted roughness vs beam voltage calculated from the measured TS at all three wavelengths on substrate B. Figure 3.20 (b) does the same for substrate C.

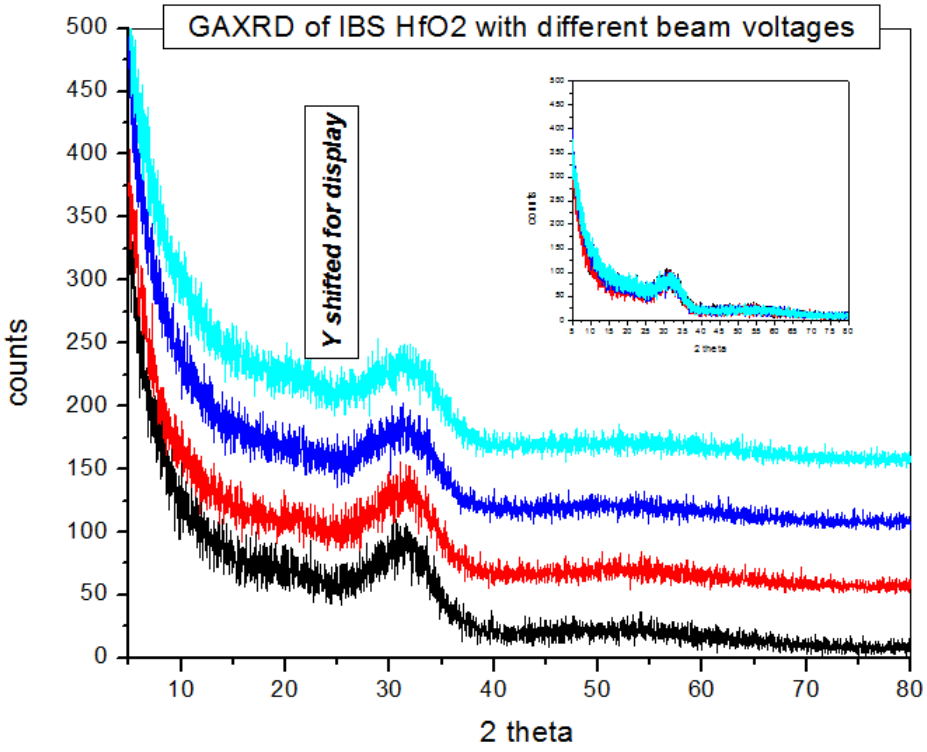

Figure 3.19: XRD Results for samples with different beam voltage.

For substrate B, the predicted roughness increases at about the same rate for all three wavelengths. The slope of the regression on the 1064nm samples is slightly shallower than that of the 405nm and 633nm samples, which is expected given that the increase in roughness appears to be mostly in the high spatial frequency range (pits) which affect lower wavelengths more. However, the difference between the slopes is not huge, and the predicted roughness of the 1064nm set is clearly increasing, likely indicating that there is some increase in lower spatial frequency roughness as well. This assertion is supported by the PSD data which shows an increase at lower spatial frequencies that is significant but less than the increase at higher spatial frequencies.

For substrate C (Figure 3.20 (b)), the difference between the short wavelength scatter and the long wavelength scatter is more evident. The 1064nm trend line is nearly flat. This indicates that the low spatial frequency roughness does not evolve significantly compared to high spatial frequency roughness. This matches the qualita-

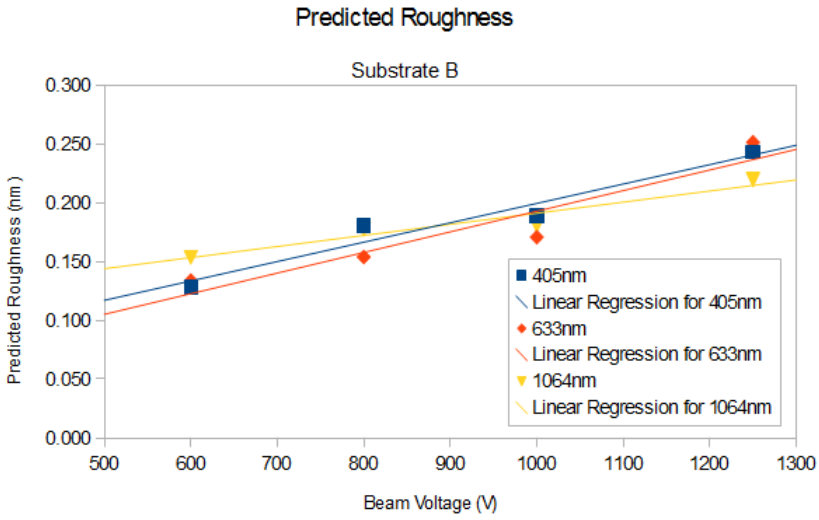

(a)

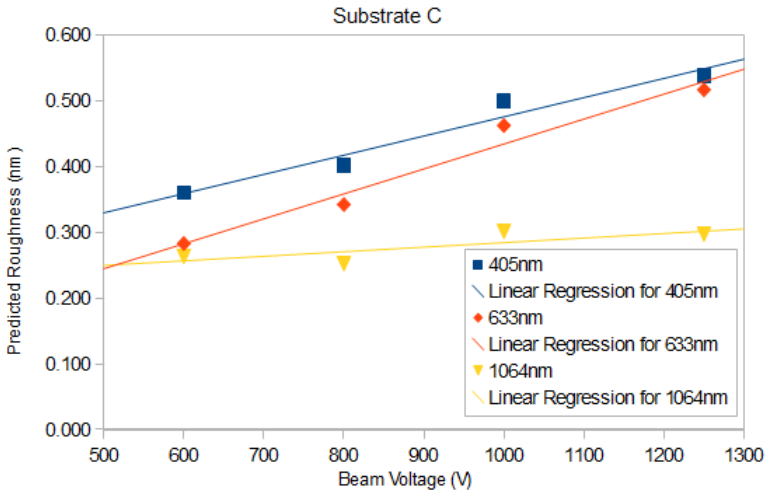

(b)

Figure 3.20: Predicted roughness calculated from measured TS values vs beam voltage for (a)substrate B and (b) substrate C.

tive and quantitative findings in section 3.1.3 which showed that the pit area increased significantly with beam voltage, especially on substrate C, and that most of the increase in the RMS roughness value came from the high spatial frequency end of the PSD. The lack of increase of predicted roughness at 1064nm is in agreement with the PSD, which shows nearly even values at the low end of the power spectral density spectrum.

The significant discrepancies in RMS roughness and scattering values between the high quality substrates (A+B) and the low quality substrates (C) especially at high beam voltage points to a different growth morphology on the different substrates. This is made even more puzzling by the fact that the two high quality substrates used are different in most every way. Substrate A is amorphous fused silica and substrate B is crystalline sapphire. The only similarity between the two is surface quality, yet the results yield nearly no differences in performance. As such, it seems that the growth morphology of the film may depend principally on the surface finish of the substrate it is deposited on.

It is important to note that the absolute values of the predicted roughness are not completely accurate. Equation 3.2 only applies to samples with a single surface. Thin films on a substrate behave differently and accurate models can only be developed if the degree of correlation between the surfaces is known. Also, the correlation length of the interface in question must be much larger than the wavelength of light for the relationship to be completely accurate. It is not clear on these surfaces whether this is true as there are different regimes of correlation to be considered and the regime sampled depends on the instrument used (ie, the correlation length calculated by an AFM is different than the correlation length measured by a WLI for the same sample).

One of the main goals of this project is to produce coatings with the lowest total loss possible at 1064nm. To that end, it is worthwhile to calculate the total loss for

these samples by summing the absorption and scatter losses. Figure 3.21 shows a plot of total loss vs beam voltage.

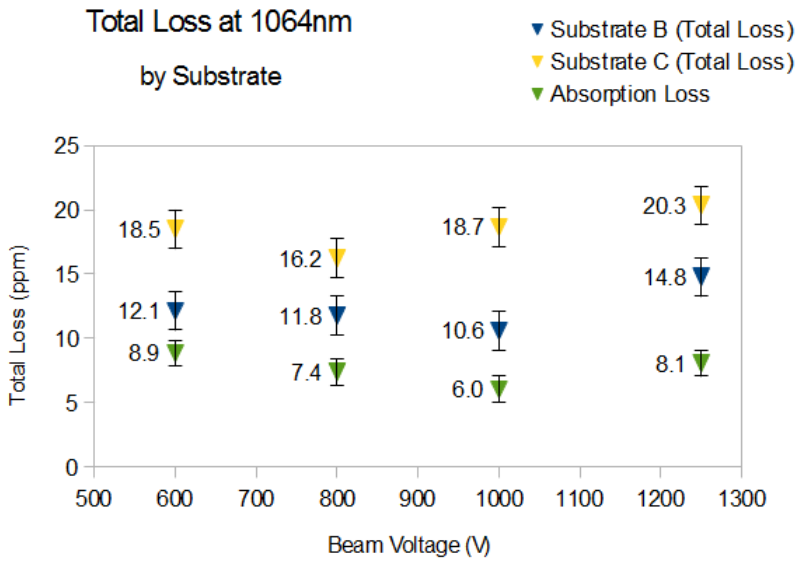

Figure 3.21: Plot of total loss at 1064nm (TS + α_{abs}) vs beam voltage for substrates B and C.

This plot shows that for both substrates, the optimal value is not at either end of the beam voltage spectrum, but at an intermediate value. For substrate B, the best value is 1000V. For Substrate C it is 800V. However, none of these differences are large enough to be significant as the error bars on all the points either nearly or do overlap. Also, more runs should be done to be sure of the repeatability of each of the loss values. That all said, it is clear that beam voltage is not a perfect tool in minimizing scatter at 1064nm as the improvement that was found by lowering the beam voltage by more than half was minimal on substrate B and basically null on substrate C. The absorption loss could be reduced through annealing which would make reduced scatter loss the more important factor in the total loss value.

Though lowering beam voltage does not appear to be effective in significantly reducing scatter loss at 1064nm, it is clearly beneficial in creating smoother coatings that scatter significantly less at shorter wavelengths. This should be considered when

making coatings for applications in the visible. Structurally, there is not any significant change between coatings deposited at high and low beam voltage as the index of refraction and the GAXRD spectrum do not change between samples.

3.2 Set 2: Thickness

Previous work at CSU and in the literature has shown that the surface quality of thin films degenerates with increased film thickness[ref]. Though there is mention of this phenomenon in Gallais et al[23], there has not been a systematic study on HfO_2 surface quality vs thickness. To understand how film thickness may affect HfO_2 films, a set of four thin films of varying thickness on optical substrates are characterized. Only the lower quality substrates (substrate C) are used in this study. All films were grown under identical conditions, with a beam voltage of 600V. Their thickness vary from 100nm to 400nm. Details for the substrate can be found in figure 3.2. The surface quality of these samples are characterized using an AFM and a WLI. Sample thickness and optical constants are measured through spectroscopic ellipsometry. Scatter loss is measured at 405nm, 633nm and 1064nm.

3.2.1 Optical properties

The index of refraction of these samples was measured using spectroscopic ellipsometry as described in section 3.1.2. Figure 3.22 shows a plot of the index of refraction at $\lambda = 1064$nm vs film thickness. This plot shows a decreasing index of refraction with increasing film thickness. This may imply that there is increased porosity or decreased packing density with thickness.

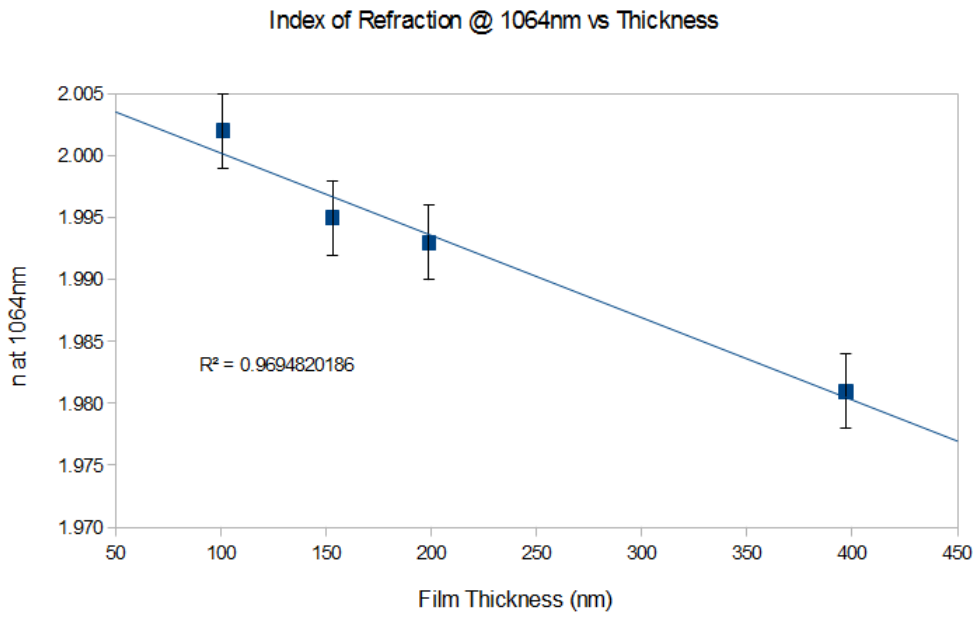

Figure 3.22: Index of refraction at 1064nm as a function of film thickness.

3.2.2 Surface roughness

Three spots on each sample were mapped out in the AFM and in the WLI in the same way as in section 3.1.3.

Surface scans

Figure 3.23 shows an example of AFM scans for each film thickness as well as the associated pit map. As with the samples in the previous section, the form the roughness takes tends to be that of plateaus with deep narrow pits. The first scan shows very little in the way of pits, and some of the polishing marks from the substrate can be seen reproduced in the coating surface. In figures 3.23 (b) and (c) the pits begin to appear and less can be seen of the polishing marks from the substrate. Gouges such that seen in figure (c) are evident in all of the scans of the 200nm thick sample. The 400nm thick coating is more covered with pits, and the pits appear to be slightly bigger and deeper (notice the change in the scale).

WLI scans for each film thickness are shown in figure 3.24. The overall texture

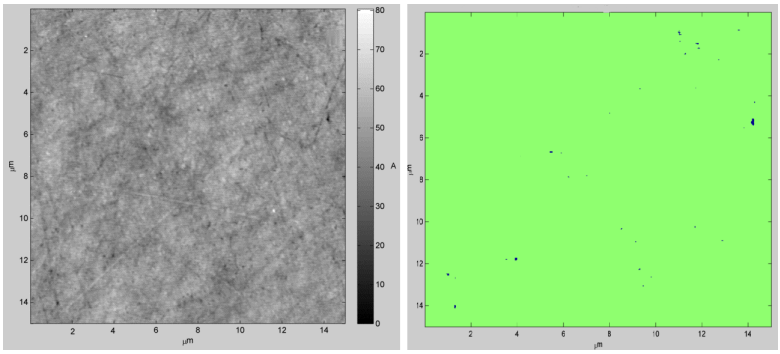

(a) 100nm thick

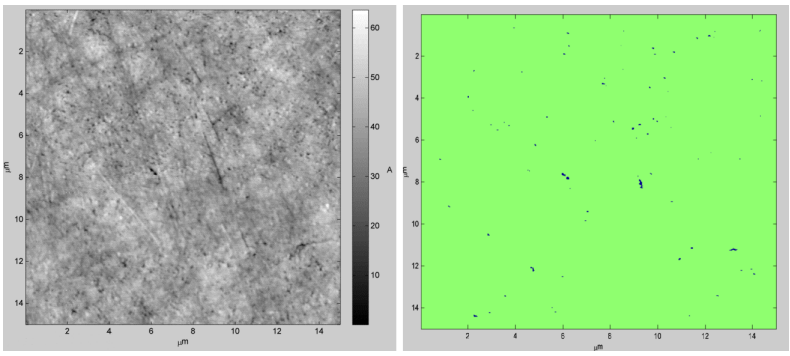

(b) 150nm thick

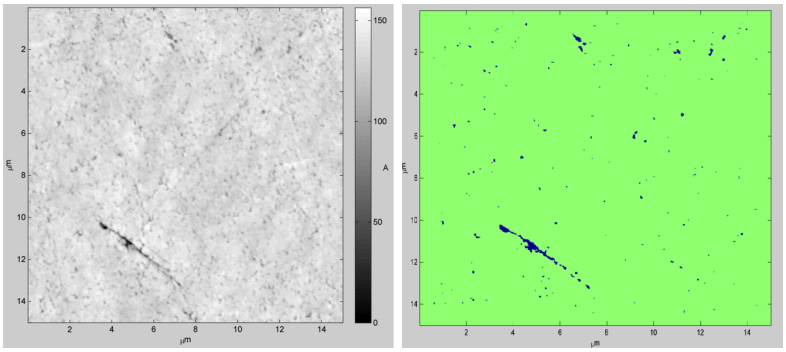

(c) 200nm thick

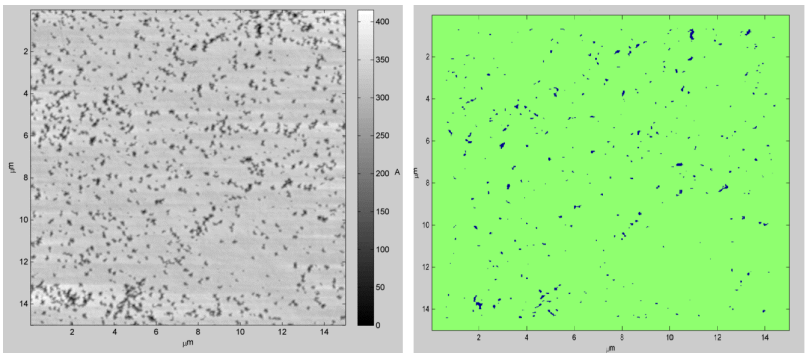

(d) 400nm thick

Figure 3.23: Height map and pit map for 100nm thick coating.

of the surface does not change much for the 100nm, 150nm and 200nm samples, but the peak to valley range does increase slightly. The surface topography changes for the 400nm thick sample. The sample is generally flat with large gouges and valleys that are consistent with what was seen in the AFM in size. Also, the peak to valley measurement is larger in the 400nm sample. This result is significant because the first three samples show very little difference in the range of roughness that should affect scattering at 1064nm. The feature size that has grown more evident in the 400nm sample is around the range of sizes that should have a significant role in scatter loss at 1064nm.

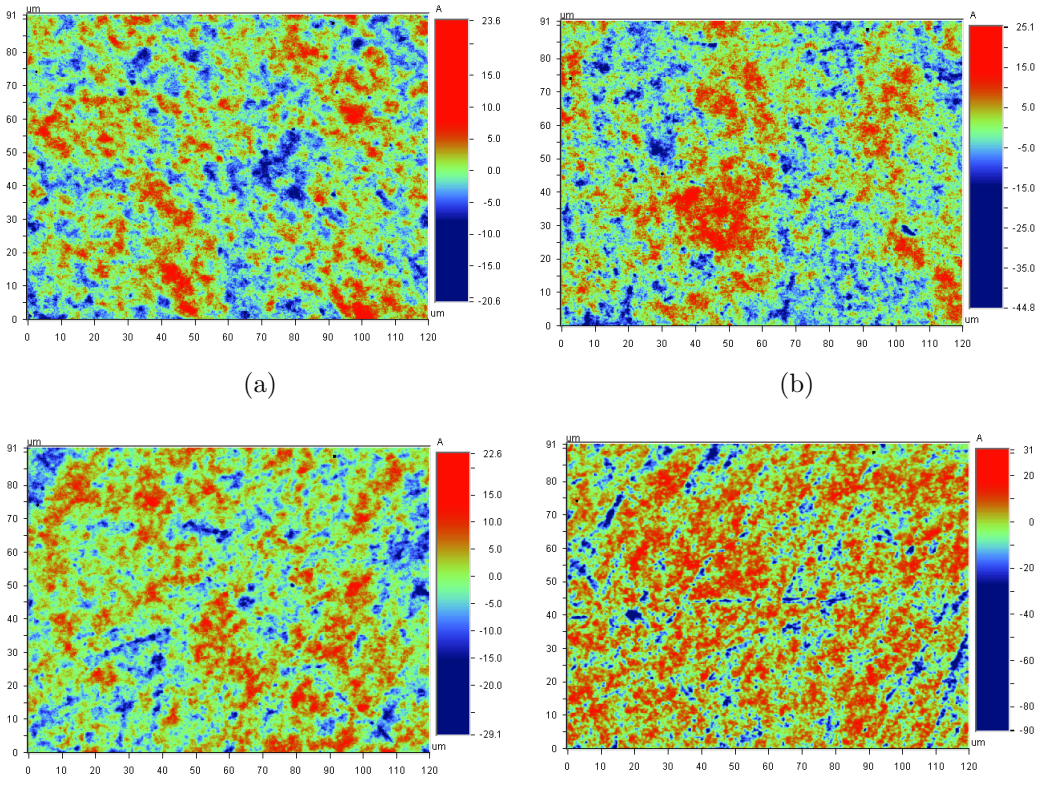

(a) (b)

(c) (d)

Figure 3.24: Example WLI scans of thin films of different thicknesses (a) 100nm thick (b) 400nm thick.

Roughness statistics

From these surface maps, statistics are compiled to benchmark the quality of the surface. Figure 3.25 is a plot of RMS roughness as calculated from AFM scans vs film thickness. For the 100nm film, the roughness is only slightly higher than that of the substrate. Surface roughness increases as the films get thicker.

Pit area is calculated for each sample as in section 3.1.3. Figure 3.26 shows a plot of pit area vs thickness. There is a distinct trend towards increasing pit area for thicker films, though the pit area does not reach as high of a value as seen in the beam voltage study. This is a bit surprising given the extremely high RMS values shown in figure 3.25. One explanation to these high RMS values is the depth of the pits. The pits in sample 4 (1250V, 150nm) are only about 10nm whereas the pits in sample 8 (600V, 400nm thick) are around 30-40nm deep (though as noted earlier, this depth is only an approximation).

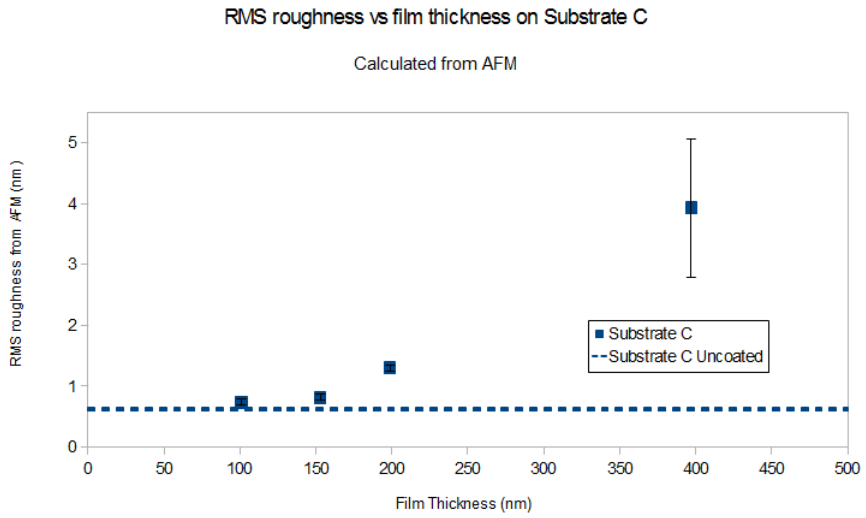

Figure 3.25: Average RMS roughness vs thickness.

Figure 3.27 shows the RMS roughness as calculated from the WLI. The roughness values support the conclusions drawn by examining the scans. The RMS roughness has a general upward trend with beam voltage, but does not change much for the

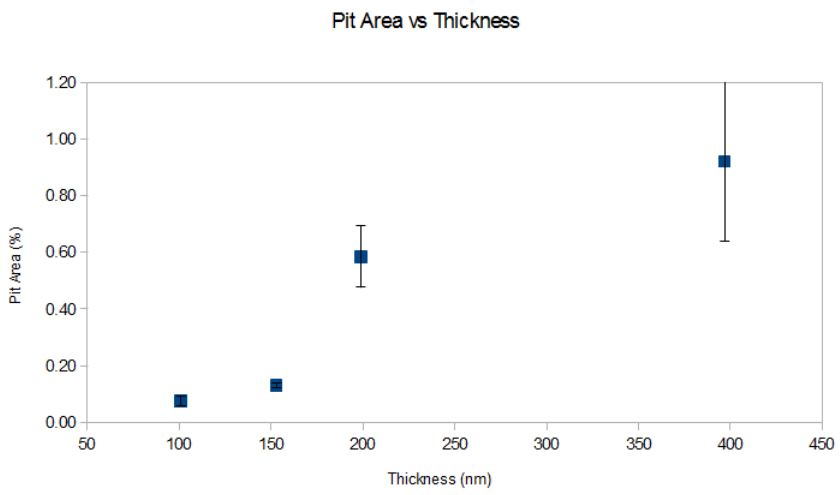

Figure 3.26: Pit area vs film thickness. Pit area increases steeply with thickness.

first three samples, which stay quite close to the substrate value. However, the 400nm sample is significantly higher, indicating there should be much higher long wavelength scatter from this sample.

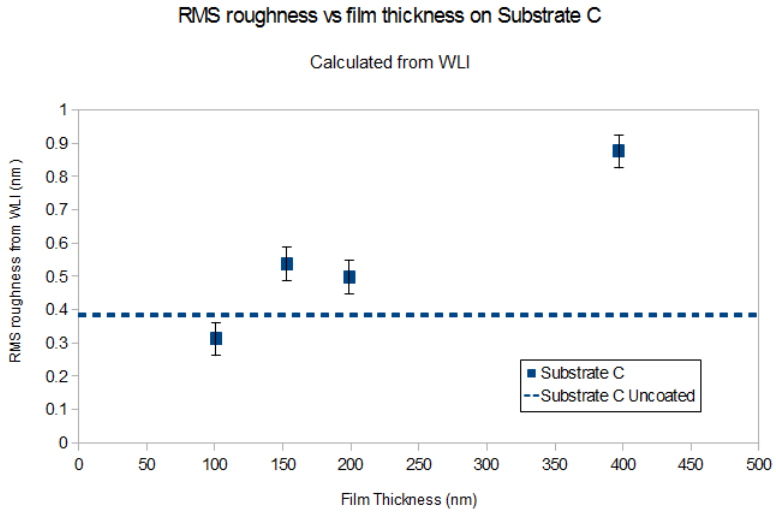

Figure 3.27: RMS roughness vs film thickness calculated from the WLI.

Figure 3.28 shows height histograms calculated for each different thickness sample. There is not a significant change in the 100nm, 150nm and 200nm samples aside from a slight broadening of the histogram and slight increase on the lower tail of the histogram. The disproportionate raising of the lower tail when compared to the

upper tail is an effect of the pits, so the histograms support the conclusion from the pit area calculation that the concentration of pits is increasing with thickness. The histogram for the 400nm sample significantly different than the thinner samples. The lower tail is more pronounced and extends to much lower height values indicating the presence of a larger quantity of deeper pits. The most important change, however is the broadening of the actual Gaussian distribution. The width is nearly double that of the thinner samples, indicating a vast increase in the random roughness which should have a more significant affect on scattering at all three wavelengths.

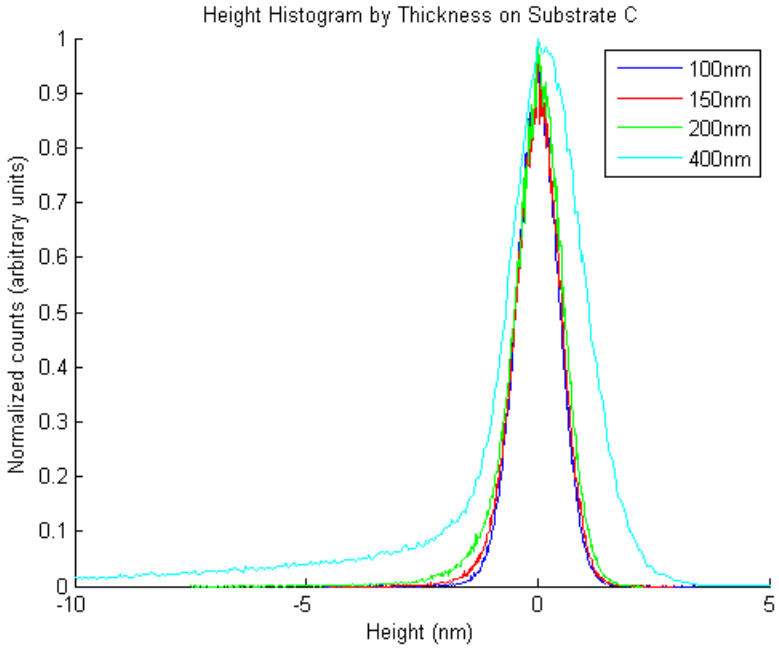

Figure 3.28: Height histogram for different film thicknesses.

To better predict the scatter loss at specific wavelengths, a PSD is computed for each sample. Figure 3.29 shows the overlaid PSDs for each of the samples. As with the histogram, the PSD shows an overall trend towards higher roughness with higher beam voltage. There are small changes between the 100nm, 150nm and 200nm samples, but a large jump up to the 400nm sample. The change from 100nm to 150nm and 150nm to 200nm samples is mostly in the lower spatial frequency regime, indicating that there will be more of a change in scattering at shorter wavelengths

between these samples. However, the increase in the PSD for the 400nm thick sample is across the entire range of frequencies sampled, and is maximum at around 2 μm^{-1}. The scatter loss for this sample should be quite high for all three wavelengths.

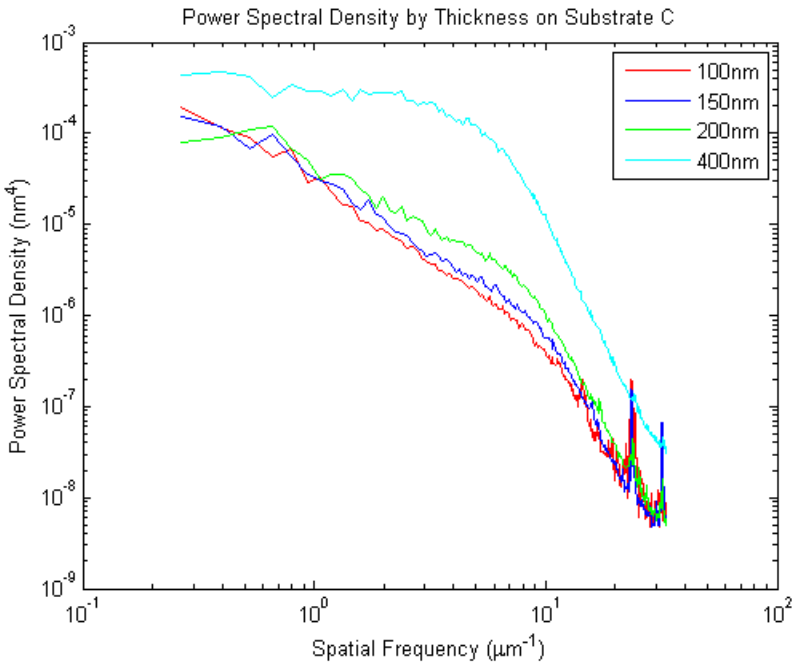

Figure 3.29: Power spectral density (PSD) plots for different film thicknesses.

3.2.3 Scatter loss

Figure 3.30 shows a plot of total scatter loss vs thickness for the three different wavelengths tested. Figure 3.30 (a) shows a comparison of all three on a logarithmic scale. Figure 3.30 (b) - (d) show scattering at each wavelength individually. Scattering increases significantly with thickness at both 405nm and 633nm wavelengths, as is expected based on the pit area values in figure 3.26 and the PSD plots in figure 3.29. The increase is particularly evident for the 200nm and especially the 400nm sample where scattering reaches 0.1% at 633nm and 0.5% at 405nm.

1064nm scattering matches the range of values seen in the beam voltage samples on substrate C for the 100nm and 150nm thick samples. Unlike the beam voltage

samples, the scatter loss at 1064nm increases sharply for the thicker samples, reaching 0.017% for the 400nm sample.

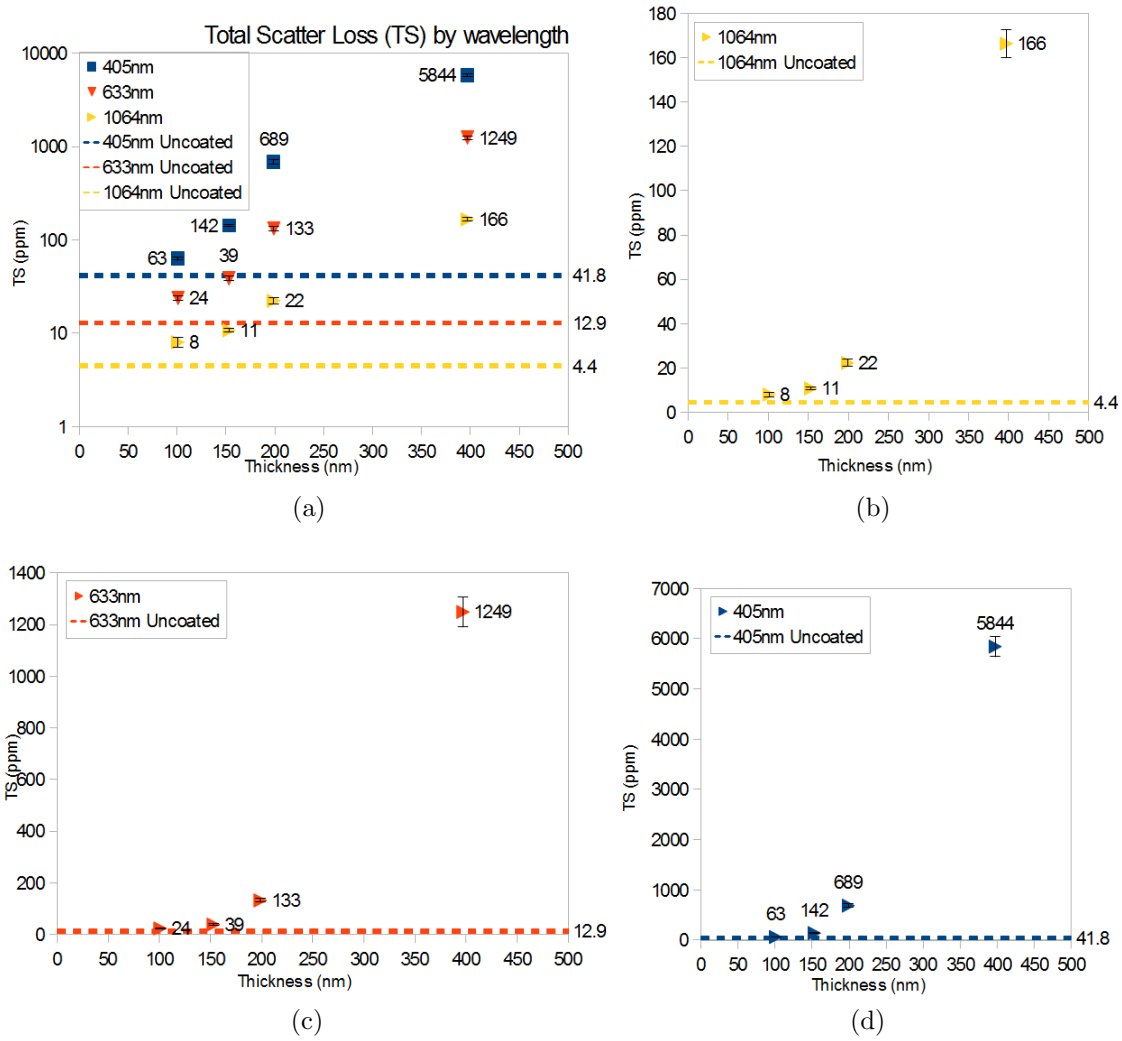

Figure 3.30: TS vs thickness single layers of HfO2 on substrate C

3.2.4 Discussion

There is qualitative agreement between the roughness and scattering results. In each case, as thickness increases, so does the RMS roughness value. The AFM roughness increase seems to follow the same trend as the scattering at 633nm and 405nm. The WLI roughness seems to follow a more gradual upward trend, one that matches the

increase in scattering at 1064nm.

To compare these sets of data quantitatively, a predicted roughness value is calculated from the scattering values at each wavelength. The predicted roughness vs thickness is plotted in figure 3.31. This plot supports the qualitative conclusions given in the previous paragraph. These values are lower because the roughness values are skewed by the deep small pits that are on the low end of the range of feature sizes for scattering at 405nm and 633nm. Also, steep walled and deep pits can significantly skew RMS roughness results without significantly affecting scattering.

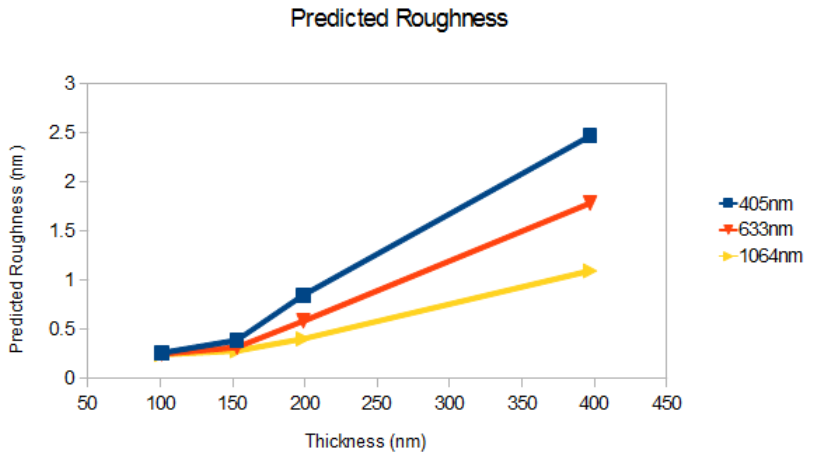

Figure 3.31: Plot of predicted roughness vs thickness for single layers deposited on substrate C.

The predicted roughness values achieved here seem to be in agreement with the PSD plots shown in figure 3.29. The contribution of lower spatial frequencies to the overall roughness stays fairly consistent for films up to about 200nm, which is consistent with the fact that scattering at 1064nm does not increase significantly. for the 400nm thick coating, a significant increase in the PSD at low spatial frequencies translates into a significant increase in scattering at 1064nm. The PSD increases disproportionately in each scan towards the high end of the spatial frequency spectrum (50x increase at $5\mu m^{-1}$ as compared to only 5x increase at $0.2\mu m^{-1}$) which is consistent with the increases in scattering at 633nm and 405nm.

The scatter values, RMS roughness, PSD and histogram analysis all seem to point to what can be seen qualitatively in the scan: the surface topography of the 200nm and 400nm samples is fundamentally different than what is seen on the thinner samples or the high beam voltage samples on substrate C. In addition to pits, the 200nm and especially the 400nm samples have wide valleys and gouges that affect scattering at longer wavelengths. There also appears to be an inflection point in the growth process between 150nm and 200nm where the sample surface begins to deteriorate more generally. More work needs to be done to determine whether this phenomenon is related exclusively to thickness or if something else (such as the increase in temperature from having the ion beam on for such a long time) is affecting the growth morphology. If roughness is simply a function of film thickness, creating smooth multilayer coatings could be problematic.

3.3 Multilayer

The previous sections focus on comprehensive testing of single layer films. This is necessary to systematically understand the individual contributions of different deposition parameters to the optical and structural properties of the finished films, but does not necessarily reflect directly upon a completed thin film stack. Films made for actual optical applications such as anti-reflection or mirrors are many layers thick. Anti-reflection coatings can consist of only four layers, but output couplers and high reflectors may reach ten to twenty or more layers. The results of the film thickness study in section 3.2 indicate that thicker films may have significantly higher scatter loss. Though single layers in a quarter wave stack centered at 1064nm are only 130nm thick, it is not clear whether the trend towards increased roughness with thickness holds true for HfO_2 layers separated by layers of different a material. To see how well these findings translated into actual useful films, an output coupler made up of

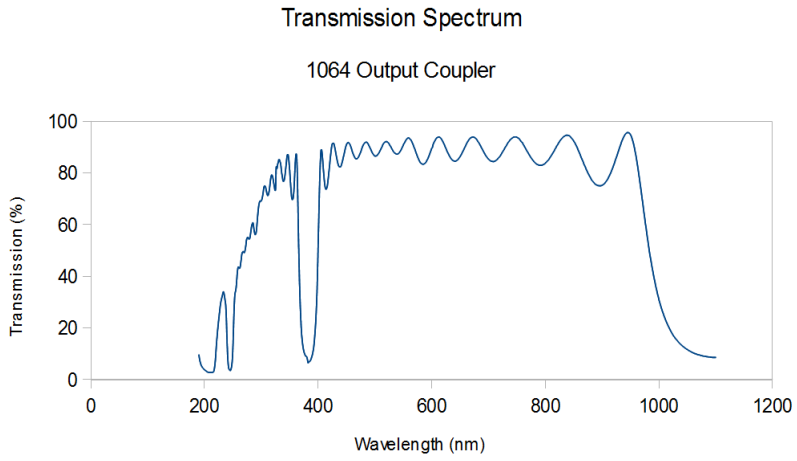

(a)

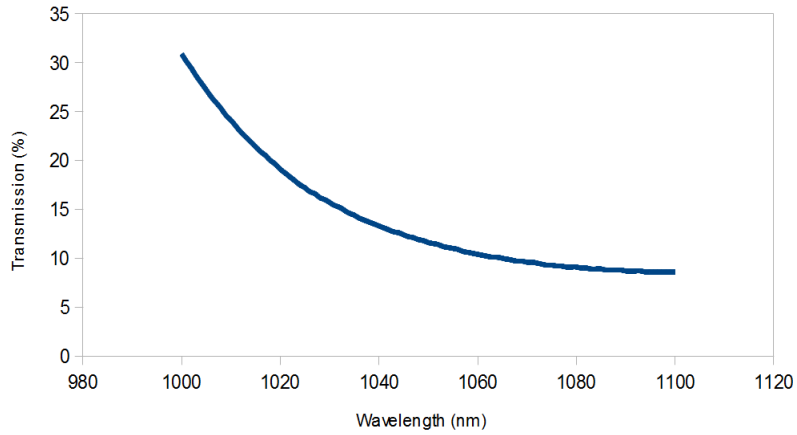

(b)

Figure 3.32: Transmission spectrum for output couplers produced at CSU. The output coupler is designed transmission is 10% at 1064nm.

8 bilayers of HfO_2 and SiO_2 was grown using the ion beam parameters for sample 1 (600V, 400mA). The output coupler is designed to have 10% transmission at 1064nm and is deposited on Substrates A and C. As a comparison, an identical output coupler was produced by a private company in a DIBS system similar to the one at CSU. This output coupler was deposited on substrate A. All of three output couplers were analysed using the spectrophotometer, AFM, WLI as well as scatter loss at 1064nm. The intention of the experiment is to understand how the output couplers designed at CSU compare with commercially available ones. Figure 3.32 shows the transmission

curve for the CSU output couplers.

AFM scans for each sample as well as associated pit maps are shown in figure 3.33. The scans of the output couplers look much more like the scans of the thinner samples, and less like the thick samples. This is true of samples grown on substrate A and substrate C. In each case, there are slightly more pits in the multilayer than in the single layer, but the pits are approximately the same size and depth. The commercial multilayer has pits quite similar to those seen in the CSU multilayer grown on substrate A, but in slightly lower concentration.

RMS roughness is calculated from AFM and WLI scans using equation 1.13. Figure 3.34 shows a table of results for the different output couplers as well as some results for single layer coatings taken from section 3.1. Figure 3.35 compares power spectral densities for the multilayers. The CSU coating on substrate A is very comparable to the commercial sample. The two match it quite closely at each spatial frequency. However, the multilayer on substrate C shows an increase at low spatial frequencies when compared to the samples on super polished substrates. There is very little increase, however, at higher spatial frequencies. This indicates that there is very little affect from the pits and that smaller surface features have been smoothed out by the multilayer. The low spatial frequency roughness of the lower quality substrate is not smoothed out by the coating.

The multilayer films produced at CSU have roughness values that are very comparable to the single layer films on their respective substrates. The multilayer on substrate A suffers a slight increase in roughness compared to the single layer. The same multilayer on substrate C does not show any increase over the single layer on the same substrate. The WLI roughness values behave similarly, except that no increase is seen for the multilayer on substrate A (though both samples are right at the detection limit for the device). Neither the AFM nor the WLI show roughness of the type or magnitude that was seen for the thick sample in section 3.2. This indicates

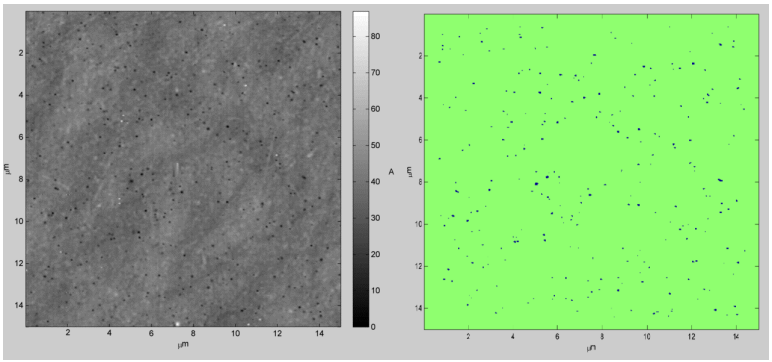

(a)

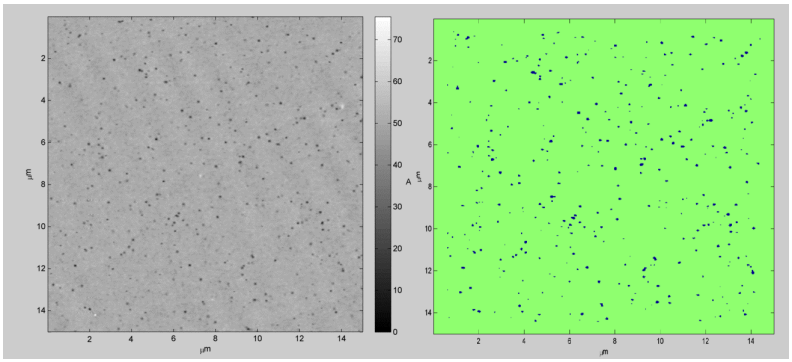

(b)

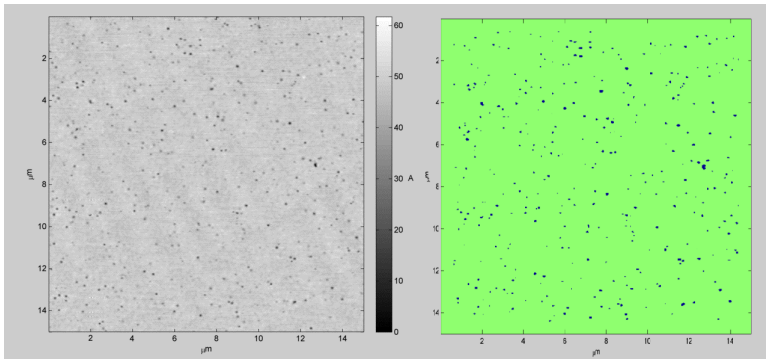

(c)

Figure 3.33: Scans of multilayers. (a) CSU multilayer on substrate C, (b) CSU multilayer on substrate A, (c) Commercial multilayer on substrate A.

	Substrate	AFM Roughness (nm)	WLI Roughness (nm)	Total Scatter at 1064nm (ppm)
CSU Output Coupler	A	0.25 ± 0.05	0.17 ± 0.05	12.3 ± 0.7
	C	0.61 ± 0.05	0.46 ± 0.06	25.8 ± 0.7
Commercial Output Coupler	A	0.26 ± 0.05		9.9 ± 0.7
CSU Single Layer	A	0.17 ± 0.05	0.19 ± 0.05	2.7 ± 0.5
	C	0.59 ± 0.07	0.47 ± 0.05	9.6 ± 0.5

Figure 3.34: Table of results of characterizing of multilayer and singlelayer samples produced at CSU and from a private company.

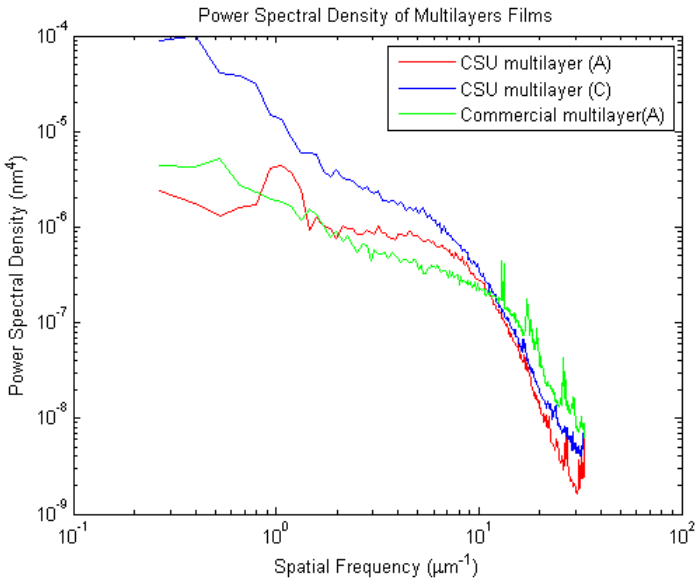

Figure 3.35: PSD comparing CSU and commercial multilayers.

that something is preventing the type of growth that causes the huge roughness seen in sample 8. Possible explanations for this are that the SiO_2 may be smoothing out roughness between HfO_2 layers, or perhaps a short pause between layers is changing the dynamics of the growth process.

The CSU multilayer on both substrates showed a varying increase in scattering at 1064nm. The sample on substrate A showed an increase of about 4x when compared with the single layer on the same substrate while the multilayer on substrate C showed an increase of around 2.5 times over the the single layer. An increase in scatter with little increase in surface roughness suggests that there is increased scattering occurring within the multi-layer stack. Based on the magnitude of the increase, there is likely

scatter coming from uncorrelated layers within the stack. This lends credence to the idea that the HfO_2 layers are increasing the surface roughness which is then smoothed out by the SiO_2 layer, thereby creating uncorrelated pit patterns from one HfO_2 layer to the next.

The CSU multi-layer on substrate A compares very well with the commercial multi-layer in terms of scatter loss at 1064nm. As noted above, both share similar surface topography (smooth with scattered small pits) and have nearly identical roughness.

Chapter 4

Conclusion and future work

The motivation for this work was to determine scatter loss at 1064nm for HfO_2 thin films, and to find ways of reducing it through substrate choice or deposition parameters. The end goal of the project is to create low loss output couplers and mirrors for use in high power lasers at 1064nm, so this work was also motivated by a need to understand how changes in single layer films would translate into completed multilayer films. It was found that scatter loss as well as surface quality are sensitive to beam voltage, film thickness and substrate choice. A systematic study was conducted of HfO_2 single layer thin films at different beam voltages, film thickness, and on different substrates. To understand how the surface topography of the sample translates into scatter loss, exhaustive analysis of surface maps was conducted as well as scatter loss at shorter wavelengths, in addition to 1064nm. Other characterization techniques such as absorption loss measurement through PCI and GAXRD were used to ensure other changes in the samples were not taking place.

Results of scatter loss measurements of thin films at 1064nm showed the best thin films had losses of around 7ppm. This value was somewhat lower than would be predicted by simply taking the AFM RMS roughness. This discrepancy is explained through power spectral density analysis which shows that the roughness spectrum

peaks at higher spatial frequencies which do not as readily affect scattering at 1064nm.

Lower beam voltage created coatings with much smoother surfaces and lower scatter loss at all wavelengths. Increased thickness caused a degradation of the surface quality of the film. There appeared to be some change in the growth morphology above around 150nm where the rate of degradation intensifies significantly. At 400nm the surface quality of the coating deteriorated to the point that it was unacceptable for most optical applications.

Substrate choice had an effect on the scattering properties. Coatings on the lower quality substrate performed only slightly worse for scatter at 1064nm, but were significantly worse than the super-polished substrates at shorter wavelengths. The difference of the substrate choice on short wavelength scatter was exaggerated for higher beam voltages due to far greater pit concentration. This discrepancy suggests that the growth morphology may be different depending on the surface quality of the substrate.

The multilayer coatings made using the deposition conditions optimized for scatter loss showed little increase in roughness over single layers, but did show an increase in scattering, likely caused by scattering at interfaces within the multilayer stack. The final scatter loss values depended significantly on the substrate; the coating on the super polished substrate had half the scatter loss of the coating on the lower quality substrate. The multilayer on the super polished substrate compared very well with the commercially available equivalent on the same substrate. At 12ppm total scatter loss, the CSU multilayer suffered only 2ppm more than the commercial multilayer coating.

The general applicability of using RMS roughness as a benchmark of surface quality and for predicting scatter loss was shown to be limited. Instead, PSD analysis was shown to be a good way to predict scattering at different wavelengths. The low spatial frequency end of the PSD was more consistently in agreement with scatter

loss at 1064nm than the RMS roughness measurements.

Future work should focus on understanding and mitigating the changes in growth morphology with film thickness and substrate choice, as well as exploring other deposition parameters as tools to reduce scattering. Substrate choice could be explored with more resolution by smoothing poor substrates or using more aggressive ion polishing. Other parameters that could be explored to attempt to further reduce the scatter loss are substrate preparation techniques and target type. It would also be interesting to investigate other high index materials used in mid-infrared interference coatings such as Ta_2O_5 and Sc_2O_3.

Bibliography

[1] *Handbook of Thin Film Materials*, chapter 2: Atomic Layer Deposition. Academic Press, 2002.

[2] *A First Course in Atmospheric Radiation*. Sundog Publishing, 2006.

[3] Hitachi spectrophotomer website, 2011. http://www.hitachi-hitec.com/global/science/appli/appli_uv.html.

[4] Horiba-jobinyvone ellipsometer website, 2011. http://www.horiba.com/scientific/products/ellipsometers/.

[5] Mikromasch website, 2011. http://www.spmtips.com/probes/sc.

[6] Markosyan A., Route R., Armandula H, and Fejer M. Photothermal common-path interferometry (pci) for thermal absorption measurements. Technical report, LIGO, 2008.

[7] Jaan Aarik, Hugo Mndar, Marco Kirm, and Lembit Pung. Optical characterization of hfo2 thin films grown by atomic layer deposition. *Thin Solid Films*, 466(1-2):41 – 47, 2004.

[8] Claude Amra, Joseph H. Apfel, and Emile Pelletier. Role of interface correlation in light scattering by a multilayer. *Appl. Opt.*, 31(16):3134–3151, Jun 1992.

[9] George Atanassov, Roland Thielsch, and Dimitar Popov. Optical properties of tio2, y2o3 and ceo2 thin films deposited by electron beam evaporation. *Thin Solid Films*, 223(2):288 – 292, 1993.

[10] David Attwood. *Soft X-Rays and Extreme Ultraviolet Radiation*. Cambridge University Press, 1999.

[11] P.W. Baumeister. *Optical Coating Technology*. SPIE Press, 2004.

[12] Dinesh Patel Ben Langdon, Eric Krous, Carmen S. Menoni, and Michelle Shinn. Electron spin resonance spectroscopy investigation of ion beam sputtered hfo_2 and sio_2 thin films. volume 7132, page 71320M. SPIE, 2008.

[13] H. E. BENNETT and J. O. PORTEUS. Relation between surface roughness and specular reflectance at normal incidence. *J. Opt. Soc. Am.*, 51(2):123–129, Feb 1961.

[14] Jean M. Bennett and Lars Mattsson. *Introduction to Surface Roughness and Scattering*. Optical Society of America, 1989.

[15] Anatoly Bourov, Lloyd C. Litt, and Lena Zavyalova. Impact of flare on cd variation for 248-nm and 193-nm lithography systems. volume 4346, pages 1388–1393. SPIE, 2001.

[16] S. Carusotto, G. Fornaca, and E. Polacco. Multiphoton absorption and coherence. *Phys. Rev.*, 165:1391–1398, Jan 1968.

[17] Arnaud Darmont. Spectral response of silicon image sensors. Technical report, Aphesa, 2009.

[18] H. Davies. The reflection of electromagnetic waves from a rough surface. *Proceedings of the IEE - Part IV: Institution Monographs*, 1954.

[19] H.C. Van de Hulst. *Light Scattering by Small Particles*. Dover Publications, Inc.

[20] Angela Duparré. *Handbook of optical properties, volume I, thin films for optical coatings*, chapter 10. CRC Press, 1995.

[21] Edmund Optics, Inc., 101 East Gloucester Pike, Barrington, NJ 08007-1380 USA. *Understanding Optical Specifications*, 2011.

[22] F. Frost, R. Fechner, D. Flamm, B. Ziberi, W. Frank, and A. Schindler. Ion beam assisted smoothing of optical surfaces. *Applied Physics A: Materials Science and Processing*, 78:651–654, 2004. 10.1007/s00339-003-2274-6.

[23] Laurent Gallais, Jérémie Capoulade, Jean-Yves Natoli, Mireille Commandré, Michel Cathelinaud, Cian Koc, and Michel Lequime. Laser damage resistance of hafnia thin films deposited by electron beam deposition, reactive low voltage ion plating, and dual ion beam sputtering. *Appl. Opt.*, 47(13):C107–C113, May 2008.

[24] David J. Griffiths. *Introduction to electrodynamics*. Prentice Hall, 1999.

[25] Horiba Jobin Yvon, 3880 Park Avenue, Edison, NJ 08820. *Spectroscopic Ellipsometry User Guide*, September 2008.

[26] II House, R., J. Bettis, and A. Guenther. Surface roughness and laser damage threshold. *Quantum Electronics, IEEE Journal of*, 13(5):361 – 363, may 1977.

[27] Harold R. Kaufman and Raymond S. Robinson. *Handbook of Ion beam Processing Technology*. Noyes Publications, 1989.

[28] M. Kempe, A. Z. Genack, W. Rudolph, and P. Dorn. Ballistic and diffuse light detection in confocal and heterodyne imaging systems. *J. Opt. Soc. Am. A*, 14(1):216–223, Jan 1997.

[29] Jolanta E. Klemberg-Sapieha, Jörg Oberste-Berghaus, Ludvik Martinu, Richard Blacker, Ian Stevenson, George Sadkhin, Dale Morton, Scott McEldowney, Robert Klinger, Phil J. Martin, Nadia Court, Svetlana Dligatch, Mark Gross, and Roger P. Netterfield. Mechanical characteristics of optical coatings prepared by various techniques: A comparative study. *Appl. Opt.*, 43(13):2670–2679, May 2004.

[30] W. Kulisch, D. Gilliland, G. Ceccone, H. Rauscher, L. Sirghi, P. Colpo, and F. Rossi. Ion beam deposition of tantalum pentoxide thin film at room temperature. volume 26, pages 991–995. AVS, 2008.

[31] J. I. Langford and A. J. C. Wilson. Scherrer after sixty years: A survey and some new results in the determination of crystallite size. *Journal of Applied Crystallography*, 11(2):102–113, Apr 1978.

[32] Cheng-Chung Lee, Jin-Cherng Hsu, David T. Wei, and Jiun-Horng Lin. Morphology of dual beam ion sputtered films investigated by atomic force microscopy. *Thin Solid Films*, 308-309:74 – 78, 1997.

[33] Quan Li, Yuan-Hsin Yu, C. Singh Bhatia, L. D. Marks, S. C. Lee, and Y. W. Chung. Low-temperature magnetron sputter-deposition, hardness, and electrical resistivity of amorphous and crystalline alumina thin films. 18(5):2333–2338, 2000.

[34] SphereOptics LLC. Integrating sphere design and applications, 2007. http://www.sphereoptics.com/assets/sphere-optic-pdf/sphere-technical-guide.pdf.

[35] Ove Lyngnes, Nick Traggis, Kathy Li Dessau, and Chris Myatt. Coating technologies for high-damage-threshold optics. Technical report, Precision Photonics, 2006.

[36] H Angus Macleod. *Thin Film Optical Filters*. Institute of Physics Publishing, 2001.

[37] N. Matsunami, Y. Yamamura, Y. Itikawa, N. Itoh, Y. Kazumata, S. Miyagawa, K. Morita, R. Shimizu, and H. Tawara. *Energy dependence of the yields of ion-induced sputtering of monatomic solids*. September 1983.

[38] Mark Mero, Luke A. Emmert, and Wolfgang Rudolph. The role of native and photoinduced defects in the multi-pulse subpicosecond damage behavior of oxide films. volume 7132, page 713209. SPIE, 2008.

[39] E. Meyer. Atomic force microscopy. *Progress in Surface Science*, 41(1):3 – 49, 1992.

[40] P.B. Mirkarimi, E.A. Spiller, D.G. Stearns, V. Sperry, and S.L. Baker. An ion-assisted mo-si deposition process for planarizing reticle substrates for extreme

ultraviolet lithography. *Journal of quantum electronics*, 37(12):1514 – 1516, December 2001.

[41] Anthony Musset and Ian Stevenson. Thickness distribution of evaporated films. Technical report, Denton Vacuum, LLC, 2000.

[42] Duy N. Nguyen, Luke Emmert, Mark Mero, Wolfgang G. Rudolph, Dinesh Patel, Eric Krous, and Carmen S. Menoni. The effect of annealing on the subpicosecond breakdown behavior of hafnia films. volume 7132, page 71320N. SPIE, 2008.

[43] Novascan, Novascan Research Building 131 Main St, Ames, IA USA 50010. *Synergy ESPM 3-D Environmental Scanning Probe Microscope Operation Manual*, January 2005.

[44] D. Patel, P. Langston, A. Markosyan, E. M. Krous, B. Langdon, F. Furch, B. Reagan, R. Route, M. M. Fejer, J. J. Rocca, and C. S. Menoni. Sio[sub 2]/hfo[sub 2] multilayers: impact of process parameters and stack geometry on the optical and structural properties. volume 7132, page 71320L. SPIE, 2008.

[45] Frank L. Pendrotti and Leno S. Pedrotti. *Introduction to Optics*. Prentice-Hall, inc., 1993.

[46] P. Petrik, L. P. Bir, M. Fried, T. Lohner, R. Berger, C. Schneider, J. Gyulai, and H. Ryssel. Comparative study of surface roughness measured on polysilicon using spectroscopic ellipsometry and atomic force microscopy. *Thin Solid Films*, 315(1-2):186 – 191, 1998.

[47] D. H. Yoon S. G. Yoon, S. M. Kang. Post-annealing effects on the structural properties and residual stress of ta2o5 thin films deposited by ion beam sputtering. *JOURNAL OF OPTOELECTRONICS AND ADVANCED MATERIALS*, 9(5):1246–1249, May 2007.

[48] Erik S. Thiele and Roger H. French. Light-scattering properties of representative, morphological rutile titania particles studied using a finite-element method. *Journal of the American Ceramic Society*, 81(3):469–479, 1998.

[49] John A. Thornton and Greene Joseph E. *Handbook of Deposition technologies for films and coatings*. Noyes Publications, 1994.

[50] Alexander V. Tikhonravov, Michael K. Trubetskov, Andrei A. Tikhonravov, and Angela Duparre'. Effects of interface roughness on the spectral properties of thin films and multilayers. *Appl. Opt.*, 42(25):5140–5148, Sep 2003.

[51] Marcus Trost, Sven Schröder, Torsten Feigl, and Angela Duparré. Influence of substrate finish and thin film roughness on the optical performance of mo/si multilayers. In *Optical Interference Coatings*, page MD4. Optical Society of America, 2010.

[52] Veeco-Ion Tech, inc., 2330 East Prospect, Fort Collins, Co 80525. *Spector user's manual*, 1999.

[53] David T. Wei, Harold R. Kaufman, and Cheng-Chung Lee. *Thin films for optical systems*. Marcel Dekker, Inc., 1995.

[54] Zhouling Wu, Christopher J. Stolz, Shannon C. Weakley, James D. Hughes, and Qiang Zhao. Damage threshold prediction of hafnia-silica multilayer coatings by nondestructive evaluation of fluence-limiting defects. *Appl. Opt.*, 40(12):1897–1906, Apr 2001.

[55] James C. Wyant. White light interferometry, 2002. http://www.optics.arizona.edu/jcwyant/pdf/meeting_papers/whitelightinterferometry.pdf.

[56] S.G. Yoon, S.M. Kang, W.S. Jung, S.-W. Kim, and D.H. Yoon. Effect of assist ion beam voltage on intrinsic stress and optical properties of ta2o5 thin films deposited by dual ion beam sputtering. *Thin Solid Films*, 516(11):3582 – 3585, 2008. Proceedings of the International Symposium on Dry Process (DPS 2006) Nagoya, Japan, November 29-30, 2006.

[57] S.G. Yoon, H.K. Kim, M.J. Kim, H.M. Lee, and D.H. Yoon. Effect of substrate temperature on surface roughness and optical properties of ta2o5 using ion-beam sputtering. *Thin Solid Films*, 475(1-2):239 – 242, 2005. Asian-European International Conference on Plasma Surface Engineering 2003 Proceedings of the 4th Asian-European International Conference on Plasma Surface Engineering.

[58] C. Zalm, Peer. *Handbook of Ion beam Processing Technology*. Noyes Publications, 1989.